Etude du champ aérodynamique et de la transition laminaire-turbulent sur l'avant-corps d'un véhicule hypersonique

Evgeniy Orlik

UNIVERSITÉ D'ORLÉANS

ÉCOLE DOCTORALE SCIENCES ET TECHNOLOGIES

LABORATOIRE ICARE-CNRS

THÈSE

présentée par :

Evgeniy ORLIK

soutenue le : **17 décembre 2009**

pour obtenir le grade de : **Docteur de l'université d'Orléans**

Discipline/ Spécialité : PHYSIQUE

Etude du champ aérodynamique et de la transition laminaire-turbulent sur l'avant-corps d'un véhicule hypersonique

THÈSE dirigée par :

M. Iskender GÖKALP	Directeur de Recherches, ICARE - CNRS

RAPPORTEURS :

M. Olivier CHAZOT	Professeur Associé, Institut Von Karman
M. Pierre COMTE	Professeur, ENSMA Poitiers

JURY :

M. Olivier CHAZOT	Professeur Associé, Institut Von Karman
M. Pierre COMTE	Professeur, ENSMA Poitiers
M. Ivan FEDIOUN	Maître de Conférences, Université d'Orléans
M. Iskender GÖKALP	Directeur de Recherches, ICARE - CNRS
M. Azeddine KOURTA	Professeur, Université d'Orléans
M. Jean PERRAUD	Ingénieur de Recherches, ONERA

Acknowledgements

This thesis is a result of a collaboration between ICARE (Institute de Combustion, Aérothermique, Réactivité et Environnement) of CNRS Orléans (UPR 3021) and ITAM (Institute of Theoretical and Applied Mechanics of the Russian Academy of Sciences, Novosibirsk). Thanks a lot to the director of my thesis Dr. Iskender Gokalp for the opportunity to perform this work and for his scientific advising.

I appreciate very much the help of Dr. Ivan Fedioun and Dr. Dmitry Davidenko. They assisted me not only in conducting my studies but also in preparing our common publications and conference presentations. Moreover, I acknowledge them for their kindness and sociality during the work and recreation. I thank Dr. Ivan Fedioun for his time spent for proofreading this thesis. One more thanks to Dr. Mark Ferrier, who worked on his thesis at ICARE and developed the stability code, which I also used.

I thank Dr. Marat Goldfeld, my first advisor at ITAM, who managed my master thesis. He taught me the basics of aerodynamic experiments. Thanks to his leading role in the ITAM experimental team and his kind assistance in my work, the transition experiments are successful. I want to say some warm words to the members of ITAM team: Starov Alexey, Timofeev Konstantin, Zakharova Yulia, Lavrov Vladimir and Vikharev Nikolay. It was very interesting and useful to work together with people from TsAGI: Borovoy V., Mosharov V., and Radchenko V., who also were involved in this project and provided experimental measurements on transition.

I am very grateful to Prof. Pierre Comte and Dr. Olivier Chazot, who reviewed this thesis and gave me some important suggestions to improve it. I should also thank Mr. Jean Perraud for his thorough reading and useful comments.

I am very thankful to Mr. François Falempin for his lively interest in the topic of my work and for the proposed ideas.

I thank all my colleagues from ICARE, ITAM and ONERA for fruitful discussions and agreeable conditions which surrounded me.

I must acknowledge the role of my family in my development and education. And I thank my darling wife Ekaterina for her assistance and patience.

Contents

Nomenclature

a	= speed of sound, m/s
C_p, C_v	= heat capacity at constant pressure, at constant volume, J/kg.K
f	= frequency, Hz
k	= thermal conductivity, W/m.K
$\boldsymbol{k}$	= wave vector (real), 1/m
N	= exponent in the e^N method
P	= pressure, Pa
T	= temperature, K
t	= time, s
U, V, W	= mean-flow component along x, y and z, m/s
V_φ	= phase velocity, m/s
$\boldsymbol{V_g}$	= group velocity vector, m/s
W_α	= molecular weight of species α, kg/kmol
X_α	= mole fraction of species α
Y_α	= mass fraction of species α
x, y, z	= streamwise, transverse (normal to the wall) and spanwise coordinates, m
X, Y, Z	= coordinates in the global reference frame attached to the vehicle, m
α, β	= wavenumbers (complex) in the x and z directions , 1/m
θ	= momentum thickness, m
θ_g	= direction of $\boldsymbol{V_g}$
μ	= viscosity, kg/m.s
ρ	= density, kg/m^3
$\boldsymbol{\sigma}$	= amplification vector (real), 1/m
ψ	= direction of $\boldsymbol{k}$
$\overline{\psi}$	= direction of $\boldsymbol{\sigma}$
ω	= (real) pulsation, 1/s
Subscript	
M	= maximum value (envelop method)
u	= unity
w	= value at the wall
∞	= value at infinity, static value
e	= value in the free-stream, outside the BL
Numbers	
M	= Mach number
Re	= Reynolds number

Introduction

On peut faire remonter les premières études intensives sur le vol hypersonique au milieu des années 1950. Les applications étaient alors principalement militaires et liées aux missiles balistiques. Le premier avion hypersonique fut construit dans les années 1960 par la compagnie North America pour le compte de la NASA. Cet appareil, le X-15, utilisé pour recueillir des données expérimentales en vue de préparer les futurs vols hypersoniques, a atteint Mach 6.7 en 1967. Durant les années 1970, l'intérêt pour le vol hypersonique retomba, principalement en raison des limites techniques des systèmes de propulsion : les moteurs aérobies (turboréacteurs et statoréacteurs) ne permettaient pas d'atteindre des vitesses hypersoniques, et les moteurs fusée présentaient l'inconvénient de devoir emporter le comburant. Le développement des superstatoréacteurs (statoréacteur dans lequel la combustion de fait dans écoulement supersonique) a permis de lever cette limitation. La figure 1 montre les performances comparées de différents moteurs aéronautiques en termes d'impulsion spécifique (rapport poussée/consommation de caburant). L'impulsion spécifique des moteurs fusée est de l'ordre de 400 s, indépendamment du nombre de Mach, ce qui est faible comparé à celle d'un superstatoréacteur. La figure 2 montre les limités d'application des scramjets en termes d'altitude. Une d'altitude optimale d'utilisation d'un scramjet en vol hypersonique à Mach 6 est 20-40 km.

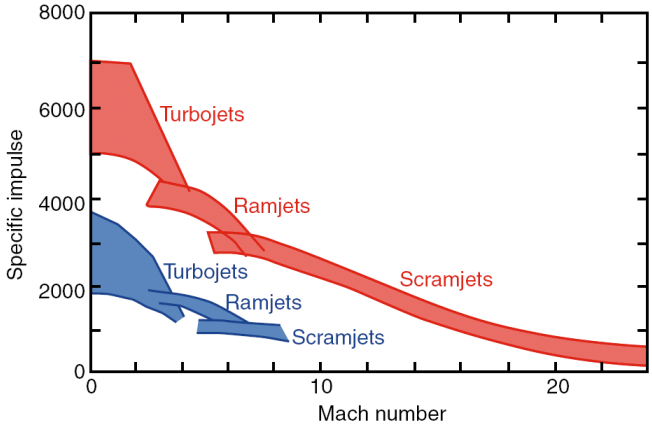

Figure 1: L'impulsion spécifique pour différents moteur (rouge: hydrogène, bleu: hydrocarbure).

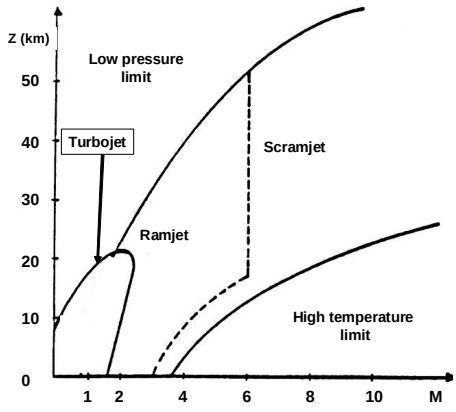

Figure 2: Altitudes pour les ramjet/scramjet.

Un ambitieux projet de lanceur récupérable, permettant un accès à l'espace à coût réduit, a alors vu le jour. Au début des années 1980, le programme américain NASP (National AeroSpace Plane) prévoyait de construire un lanceur récupérable de plus de 30m de long, décollant et attérissant comme un avion. En Europe, des études similaires ont débuté au début des années 1990 avec le programme français PREPHA (Programme de Recherche et d'Etudes sur la Propulsion Hypersonique Aérobie, 1992-1998). Cette étude a été plus ou

moins suspendue à cause de problèmes technologiques insurmontables. Les recherches sur le vol hypersonique se sont néanmoins poursuivies au niveau européen avec le projet franco-allemand JAPHAR (Joint Propulsion for Hypersonic Airbreating application Research) co-dirigé par l'ONERA (France) et le DLR (Allemagne). Ces études menées de 1997 à 2002 avaient pour objectif la conception d'un démonstrateur en vol propulsé par un stato-mixte. Au même moment aux USA, le programme Hyper-X visait à faire voler à Mach 10 un démonstrateur de taille réduite (environ 4 mètres) propulsé par un superstatoréacteur. Cet objectif a été atteint pendant 10s en novembre 2004 par le X-43A. La figure 3 montre une vue d'artiste du X-43A. Aujourd'hui, le X-51A WaveRider américain est prévu pour voler à l'aide d'un superstatoréacteur pendant 5 mn, accélérant de Mach 4.7 à plus de Mach 6, prouvant ainsi que le vol hypersonique soutenu est possible. Le premier vol du X-51 (figure **??**) est prévu au mois de décembre 2009.

Figure 3: X-43.

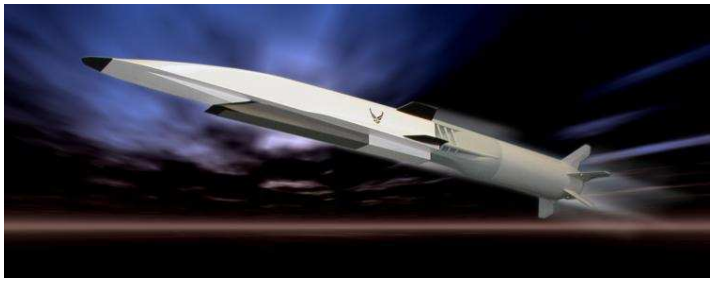

Figure 4: Boeing X-51 A.

A la suite du programme JAPHAR, le programme PROMETHEE (1999-2002) et maintenant le programme LEA (figure 5) sont une coopération MBDA France - ONERA visant à nouveau à construire puis lancer un véhicule expéri- mental hypersonique. Le premier vol du véhicule hypersonique LEA est prévu en 2013. Ce véhicule propulsé par superstatoréacteur doit voler de Mach 4 à Mach 8 à une altitude comprise entre 20 et 30 km, en partenariat avec la Russie. Le bombardier Russe Tu-22 puis le lanceur Volna doivent amener le LEA à la bonne altitude et l'accélérer jusqu'au nombre de Mach voulu. Le bilan aéropropulsif *poussée - traînée* doit ensuite être mesuré en vol par télémétrie 6. On trouvera plus de détails sur les projets de développement des véhicules propulsés par stato ou superstatoréacteurs, ainsi que sur le programme LEA dans les références [2, 3].

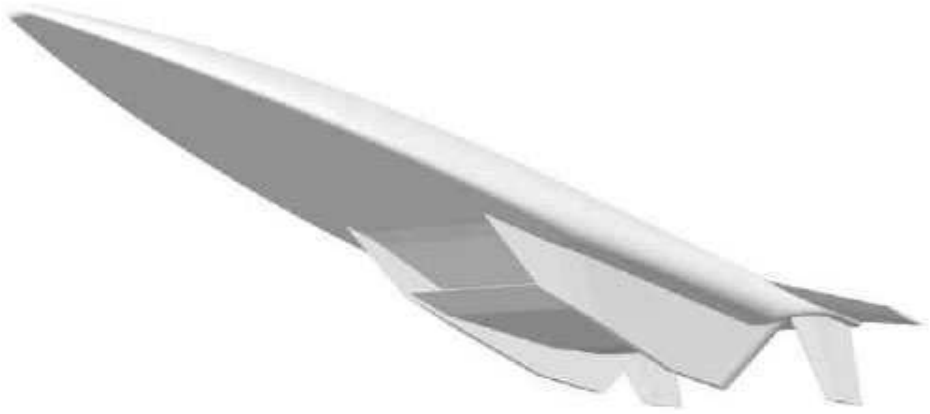

Figure 5: Vue d'artiste du véhicule LEA.

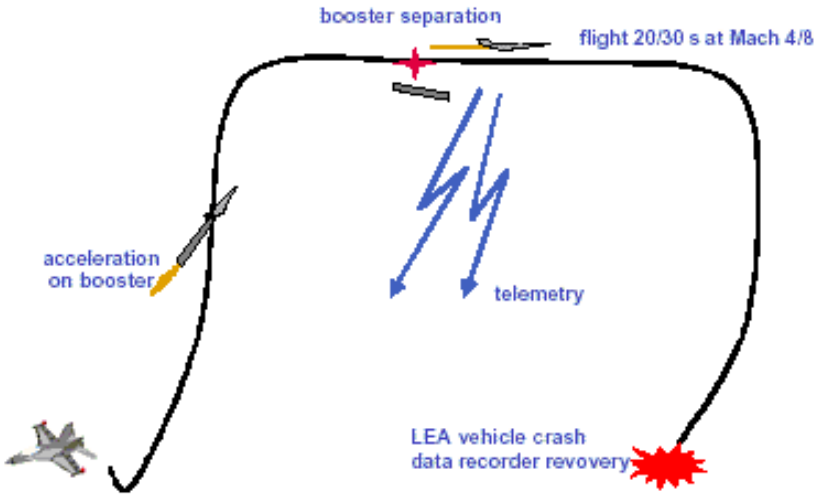

Figure 6: Programme de vol d'essai du LEA.

Un ambitieux programme (LAPCAT) a également pour but d'utiliser les technologies de type superstatoréacteur pour le transport civil (figure 7). On peut imaginer qu'un tel véhicule de transport hypersonique pourrait relier l'Europe et l'Australie en 1 heure. La conception de ce genre d'appareil impose de résoudre de nombreux problèmes, non seulement liés à la propulsion ou à l'aérodynamique, mais aussi liés au choix des matériaux, à l'écologie, à la sécurité etc. Aujourd'hui, tout celà n'est que rêve et un tel véhicule ne verra probablement pas le jour avant 2030. Seule une coopération entre les communautés scientifique et industrielle, avec l'aide des gouvernements, pourra faire de ce rêve notre réalité future.

Figure 7: Transport civil...2030?

L'étude de la transition laminaire-turbulent a une grande importance sur le plan scientifique et est d'un grand intérêt pour le développement pratique de nouveaux concepts de véhicules aéronautiques de par ses effets sur l'échauffement des parois, la contrainte de frottement, le décollement et autres caractéristiques des couches limites. Ceci est particulièrement vrai aux vitesses hypersoniques à cause des très grandes énergies mises en jeu [4, 5, 6]. Le récent regain d'intérêt pour les véhicules hypersoniques aérobies propulsés par superstatoréacteur à conduit à considerer la prévision de la transition laminaire-turbulent du point de vue de l'ingénieur, c'est à dire sur des configurations 3D réalistes à échelle 1. En effet,

pour que l'entrée d'air du moteur soit bien adaptée, il est préférable que la couche limite qui se développe sur l'avant-corps soit turbulente pour mieux résister aux gradients de pression défavorables et ainsi éviter les décollements. Une façon de résoudre le problème est de déclencher la transition à l'aide de rugosités de différentes formes et tailles réparties sur l'avant-corps. Ceci impose de faire de nombreux essais en soufferie hypersonique conventionnelle ou silencieuse pour voir ce qui est le plus efficace [7, 8]. Ceci est extrêmement coûteux. Une autre façon de procéder est de tenter de prévoir la survenue (ou non) de la transition naturelle par l'application de critères empiriques - comme le critère NASP : $\mathrm{Re}_\theta/\mathrm{M}^e = Cste$ ($150 \sim 500$, avec ou sans correction pour les effets d'émoussement [9]) mais ça ne peut être qu'une première ébauche donnant la tendance générale et étant très discutable [10, 11]. Les mécanismes conduisant à la transition sont encore mal compris. La position de la transition laminaire-turbulent dépend de nombreux facteurs dont le nombre de Reynolds, l'état de surface et les conditions atmosphériques comme le niveau de bruit dans l'écoulement. Les essais en vol sont très coûteux et les essais en soufflerie ne reproduisent que partiellement les paramètres de vol. En outre, tous les résultats expérimentaux montrent que la transition survient plus tôt en soufflerie qu'en vol.

Seule une combinaison de l'analyse théorique, de la simulation numérique (CFD) et des essais au sol peut donner des indications sur la nature de la transition, et fournir des éléments pour sa prédiction en vol. La présente étude s'intéresse à la transition laminaire-turbulent sur un avant-corps de véhicule hypersonique. Ce travail comporte à la fois des aspects numériques et expérimentaux. Tous les calculs ont été faits en France, à l'Institut de Combustion, Aérothermique, Réactivité et Environnement (ICARE), UPR 3021 du CNRS, et la partie expérimentale a été réalisée à Novossibirsk à l'ITAM, en coopération avec l'Académie des Sciences de Russie. Ce travail a débuté en octobre 2006. Marc Ferrier et Ivan Fedioun ont développé un code basé sur la théorie de la stabilité linéaire modale (LST) et l'ont appliqué pour prévoir la transition en vol. Marc Ferrier a soutenu sa thèse avec succès en mai 2008 [12]. J'ai réalisé les simulations numériques (CFD) permettant d'analyser la structure de l'écoulement, de fournir avec precision les profils de la solution de base pour les calculs de stabilité, et de concevoir les moyens d'essais expérimentaux. J'ai ensuite participé à toutes les étapes des expériences à l'ITAM à Novossibirsk, comprenant notamment leur conception, le choix des méthodes de détection de la transition, la préparation et le montage de la maquette, l'étalonnage des sondes de mesure etc. Enfin, j'ai également réalisé les calculs de stabilité dans les conditions des essais pour faire la comparaison entre les résultats théoriques et expérimentaux.

Les calculs de l'écoulement autour de l'avant-corps 3D à grande vitesse (de Mach 4 à Mach 8) et les résultats de l'analyse de stabilité dans les conditions de vol sont présentés au chapitre 1. Dans ce chapitre, je parlerai également de la structure de l'écoulement et je ferai un rappel de la théorie de la stabilité linéaire et des divers scenarii de transition à la turbulence.

La simulation numérique peut aussi donner des informations comparatives sur les écoulements laminaires ou turbulents, les épaisseurs de couche limite, les répartitions de température et les flux de chaleur pariétaux. Ces éléments peuvent servir à choisir et optimiser les techniques expérimentales les plus efficaces pour détecter la transition dans des conditions de soufflerie données. Les résultats de ces simulations seront présentés et discutés au chapitre 2.

Les précédents calculs de Marc Ferrier ayant montré qu'aux nombres de Mach les plus élevés, la transition naturelle en vol est très improbable [12], on étudie également la transition induite par rugosités. Le chapitre 3 contient une étude biliographique et passe en revue différents critères empiriques. Ces critères sont ensuite évalués pour des données obtenues par simulation numérique des expériences en soufflerie.

Les chapitres 4 et 5 sont consacrés aux essais au sol sur maquette à échelle 1/3. Les expériences sont réalisées dans deux types de souffleries : une soufflerie continue et une soufflerie à rafale. La soufflerie continue autorise des mesures détaillées dans la couche limite, mais seule une rafale obtenue dans une soufflerie à haute enthalpie permet de reproduire - au moins partiellement - les conditions de vol, à savoir les hautes températures et les transferts thermiques. La transition est détectée dans la soufflerie continue T-313 par mesure de pression Pitot. Des peintures thermo-sensibles (TSP) sont utilisées dans la soufflerie à rafale AT-303. On compare les prédictions de la transition naturelle aux résultats expérimentaux. Les résultats de transition par rugosités dans AT-303 sont discutés au chapitre 5.

La conclusion fait le bilan des résultats obtenus concernant la transition laminaire-turbulent, et donne des recommandations pour la transition naturelle et induite par rugosités dans les conditions des essais en vol.

Introduction

We can trace the first intensive study on the hypersonic flight in the 1950^{th}'s. The applications were mainly military and related to ballistic missiles. The first hypersonic aircraft was built in the 60^{th}'s by the North American Society on behalf of NASA. This machine, the X-15. which was used to collect experimental data for the preparation of future hypersonic flight, reached Mach 6.7 in 1967. During the 70^{th}'s, the interest in hypersonic flight fell, mainly because of limitations imposed by propulsion: air-breathing engines (turbojet, ramjet) do not reach hypersonic speeds, and rocket engines have the disadvantage of requiring the carriage of oxidant. The development of scramjets (supersonic combustion ramjet) has permitted to remove this limitation. Figure 1 gives comparison of efficiency for different engine conceptions. Specific impulse is ratio between thrust and fuel consumption (weight of fuel/sec). Rocket engines give impulse about 400 sec independently from Mach numbers which is less compared scramjet. Figure 2 shows altitude limitations of applicability scramjet. An example at M=6 optimal altitude for using scramjet engine for hypersonic flight is 20-40 km. In the early 80^{th}'s, the NASP american program (National AeroSpace Plane) was to make a launcher over 30 m long with an ambitious design of reusable launch vehicles, allowing access to space at reduced cost. In Europe, such studies have been initiated in the early 90^{th}'s with the french PREPHA program (Programme de Recherche d'Études Propulsion Hypersonique Aérobie). All these studies were eventually abandoned because they ran into prohibitive technological problems. Research efforts on hypersonic flight, however, continued throughout the project JAPHAR (Joint Propulsion for Hypersonic Airbreathing Application Research) co-directed by ONERA (France) and DLR (Germany). These studies have been conducted from 1997 to 2002 as the preliminary study of a dual-mode ramjet hypersonic vehicle. At the same time in the United States, the Hyper-X program aimed to fly at Mach 10 with a small scale demonstrator (about 4 meters) powered by a scramjet. This target was reached in November 2004 by the X-43A. Figure 3 shows an artist view of the X-43A. Now, the american X-51A WaveRider program is planned to fly on scramjet power for 5 min., accelerating from Mach 4.7 to beyond Mach 6 and demonstrating that sustained hypersonic flight is practical. The first flight of the X-51 (figure 4) is expected in December 2009. Next after the JAPHAR, the PROMETHEE program and now the LEA program (figure 5) is a cooperation ONERA-MBDA aimed to develop and launch an experimental hypersonic vehicle. The first flight of the LEA hypersonic vehicle is expected in 2013. The scramjet-powered vehicle is planed to fly from Mach 4 to Mach 8 at altitudes from 20 to 30 km. For flight tests Russian partners will be involved. Russian bomber Tu-22 and after launcher Volna should deliver LEA vehicle to the proper altitude and accelerate to required Mach number. The measurement of the aero-propulsive balance *trust - drag* should be provided in flight (figure 6). More details about the development of ramjet/scramjet-powered vehicles and the LEA program can be found in [2, 3].

An ambitious program (LAPCAT) is also aimed to use scramjet technologies in civil transportation (figure 7). We can imaging that such a hypersonic transport vehicle could travel from Europe to Australia for 4-6 hours. The design of such vehicle implies solving a lot

of problems, not only related to propulsion and aerodynamics, but also materials, ecological problems, safety etc. Nowadays, this is only a dream and such vehicle will probably not be built before 2030. Only a cooperation of scientific community, industries and support of governments can make this dream our real future.

The investigation of laminar-turbulent transition has a great importance regarding fundamental science and also presents great interest in the practical development of new perspective flight vehicles due to its effects on surface heating, skin friction, separation and other boundary-layer properties. This issue is especially significant at hypersonic velocities, due to the high energies and heating involved [4, 5, 6]. The recent regain of interest for hypersonic airbreathing scramjet-powered vehicles has led to consider the laminar-turbulent transition prediction from an engineering point of view, that is on full scale 3D realistic configurations. Indeed, for the air inlet to be well adapted, it is highly desirable for the boundary layer (BL) developing under the forebody to be turbulent in order to avoid flow separation due to strong adverse pressure gradients. One way to fix the question is to trigger transition with distributed roughnesses of various shapes and heights on the forebody. This implies running experiments in a conventional or quiet hypersonic wind tunnel to see what is the most efficient [7, 8]: this is very costly. Another way is to try to predict the onset (or not) of natural transition from empirical criterion - like NASP criterion: $\mathrm{Re}_\theta/\mathrm{M}_e$ =Const ($150 \sim 500$, with or without bluntness correction [9]), but this is only a first step, giving a global trend, and highly questionable [10, 11]. The mechanisms leading to transition are still poorly understood. The position of laminar-turbulent transition depends on many factors, including Reynolds number, surface roughness and atmospheric conditions like free stream noise level. Flight tests are very expensive and tests in wind tunnels reproduce only some flight parameters. Moreover, all experimental results show that transition occurs earlier in wind tunnel conditions compared to flight.

Only combined approaches of theoretical analysis, computational fluid dynamics (CFD), flight and wind tunnel tests can give information about the nature of transition and give assumptions for its prediction in flight. The present study is related to the laminar-turbulent transition on a generic forebody. This work includes both numerical and experimental studies. All computations have been done in France, at CNRS laboratory named ICARE and the experimental part has been conducted in ITAM at Novosibirsk in cooperation with the Siberian Academy of Science. This work started in October 2006. Marc Ferrier and Ivan Fedioun have developed a code based on linear stability theory (LST) and have applied it to predict natural laminar-boundary layer transition in flight conditions. Marc Ferrier successfully defended his thesis in May 2008 [12]. I provided the CFD computations, aimed to analyze the structure of the flow, to obtain accurate mean flow profiles for the linear stability analysis and to design experimental setup. Then I participated to each stage of experiments in ITAM Novosibirsk including design, methods to detect transition, preparation and installation of the experimental model, calibration of gauges, etc. Finally, I also applied the LST code to some experimental conditions for the comparison between experimental results and computations.

Simulations of the flow on the 3D forebody configuration at high velocity (from M =4 up to M =8) and stability analysis for flight test conditions are presented in chapter 1. In this chapter also I will speak about the topology of flow and will give an introduction to stability theory and paths to turbulence.

CFD can also give informations about laminar or turbulent flow fields, thickness of boundary layers, temperature distributions and wall heat fluxes. These data may help to choose and to optimize efficient experimental techniques to detect the transition for given experimental wind tunnel conditions. Results of these computations will be presented and discussed in chapter 2.

Since the previous study by Marc Ferrier has shown that at high Mach number, the natural transition is unlikely to occur in flight [13], roughness-induced transition is also studied. Chapter 3 contains a bibliography and a review of empirical engineering criteria. These criteria are evaluated on data obtained from CFD simulations of the experimental flow.

Chapters 4 and 5 are devoted to ground tests of a 1:3 scale model. Experiments are carried out in two types of wind tunnels: a blow down and an impulse adiabatic wind tunnel. A blow down wind tunnel allows detailed measurements in the boundary layer, but only an impulse regime generated in a high-enthalpy wind tunnel allows to reproduce -at least partially- the flight conditions, namely high temperature and heat exchanges. Transition is detected in the blow down T-313 wind tunnel by Pitot tube measurements. Temperature sensitive paints (TSP) are used in the impulse AT-303 wind tunnel. Computationally predicted and experimentally detected natural transition are compared. Experimental results obtained in the impulse wind tunnel AT-303 with trips are discussed in chapter 5.

The conclusion summarizes the results about laminar-turbulent transition. Recommendations concerning natural and roughness-induced transition in flight conditions are given.

Chapter 1

CFD computations and linear stability analysis

Synopsis

Ce chapitre comprend deux parties : la première décrit les paramètres physiques et numériques des calculs Navier-Stokes permettant d'analyser la structure de l'écoulement autour de l'avant-corps et de fournir les profils de base avec une précision suffisante pour les calculs de stabilité; la deuxième reprend succintement les éléments théoriques des calculs de stabilité détaillés dans la thèse de Marc Ferrier [12] et rappelle l'essentiel des résultats pour les cas "vol".

- Première partie : L'écoulement de base laminaire autour de l'avant-corps est calculé au moyen logiciel commercial Fluent®. L'air, défini selon Burcat & Ruscic [13], est un mélange de 4 composants : $X_{O_2} = 0.2095$, $X_{N_2} = 0.7809$, $X_{Ar} = 0.0093$ et $X_{CO_2} = 0.0003$. Les propriétés thermodynamiques sont calculées selon un modèle proposé par Lemmon & al. [14] pour la plage [80K, 1000K] et selon Burcat pour la plage [1000K, 5000K]. Les coefficients de transport -viscosité et conductibilité thermique- sont calculés par la loi de Wilke dans laquelle les viscosités partielles $\mu_\alpha(T)$ sont obtenues par le modèle CHEMKIN II [17] basé sur la théorie cinétique. Ce modèle thermo-transport, élaboré lors de la thèse de Marc Ferrier [12], est décrit en détail dans [13]. Les conditions statiques en vol sont déduites du modèle d'atmosphère standard US 1976.

  Le maillage de calcul présente une région non-structurée autour du nez du véhicule, et une région structurée permettant l'extraction des profils de base perpendiculairement à la paroi dans la zone d'intérêt (ZI) de l'avant-corps. Plusieurs maillages ont été testés afin de s'assurer de la bonne résolution du choc de nez d'une part, et de la région proche paroi d'autre part. La convergence des calculs est vérifiée sur la valeur des résidus, sur le bilan de masse et sur les réparations de température et de contrainte pariétale sur le plan de symétrie.

  Les principales caractéristiques de l'écoulement de base laminaire sur l'avant-corps sont la présence d'un écoulement pariétal de déversement depuis la ligne de partage vers le plan de symétrie, provoquant 2 tourbillons longitudinaux contra-rotatifs de part et d'autre du plan de symétrie, et la présence d'une couche entropique due à l'émoussement du nez du véhicule, concentrée autour de ce même plan de symétrie. L'écoulement de déversement, ou "crossflow", est dû au fait que, la section droite étant

quasi-rectangulaire, le choc est plus proche des bords latéraux que des surfaces intrados et extrados.

- Deuxième partie : La méthode retenue pour la prévision de la transition est la combinaison de la théorie de la stabilité linéaire modale locale en écoulement compressible à propriétés physiques variables, couplée à la méthode semi-empirique du e^N. Une perturbation de l'écoulement laminaire de base autour de l'avant-corps a la forme d'un mode normal 3D défini par ses nombres d'onde (complexes) longitudinal et transversal, et par sa pulsation (réelle). En chaque point de la paroi, on recherche la direction de propagation telle que l'amplification observée dans la direction de la vitesse de groupe soit maximale. On calcule alors le rapport d'amplification total d'une onde de fréquence f donnée, dont on déduit le facteur N_f. Le facteur N global est défini par l'enveloppe des courbes N_f. On admet qu'en vol, i.e. en environnement calme, la transition intervient dès que $N \sim 9$ à 10 , mais peut survenir dès $N \sim 3$ à 4 en environnement bruyant tel que les souffleries conventionnelles de l'ITAM.

  On distingue plusieurs modes d'instabilité : (i) les instabilités de type 1^{er} ou 2^{nd} mode dans la classification de Mack. Ce sont l'extension aux écoulements compressibles des instabilités de Tollmien-Schlichting d'abord identifiées dans les couches limites à basse vitesse. Le premier mode est dit "oblique" car sa direction de propagation pour une instabilité maximum fait un angle $60° \lesssim \psi_M \lesssim 80°$ avec la direction principale de l'écoulement. Le second mode est qualifié d' "acoustique" et devient prédominant pour $M_e > 5$, ce qui n'est observé que pour le cas de vol $M_\infty = 8$. Ce mode est droit, caractérisé par $\psi_M \approx 0$. (ii) les instabilités de type "crossflow", associées au caractère inflexionnel de la composante transversale du profil de vitesse, telles que $80° \lesssim \psi_M \lesssim 90°$. Certaines instabilités CF sont dues à l'amplification d'ondes stationnaires ($f = 0$ kHz), localisées près de la ligne de partage au bord d'attaque de l'avant-corps. (iii) les instabilités de la couche entropique, étudiées théoriquement et numériquement, mais trop faibles pour déclencher la transition en vol ($N \approx 4$) [12, 13].

  L'analyse de stabilité montre un effet stabilisant de l'angle d'incidence, la zone d'intérêt se trouvant "au vent". A M_∞=6, les facteurs N maximum atteignent environ 9 à 2° d'incidence, et chutent à moins de 8 à 6°. A incidence 4° constante, on constate qu'à M_∞=4, l'instabilité dominante est de type 1^{er} mode oblique car le choc principal est assez éloigné des parois. A M_∞=6 et 8, l'instabilité dominante est de type "crosfflow" près du nez et se transforme progressivement et continûment en 1^{er} mode oblique vers l'aval. Les facteurs N observés atteignent 8 à 9 sur une région assez étendue à M_∞=6, indiquant une probable transition naturelle en vol. En revanche à M_∞=8, ils ne dépassent pas 5: la transition en vol est très improbable.

1.1 Part I: CFD

1.1.1 Description of the investigated model

The forebody that has been studied is about 1.3m long (figure 1.1). The nose radius in symmetry plane is 5mm. Upper and lower faces are plane, with an angle +4.8° and -4° respectively. The end section is 0.5m × 0.2m. The scale of the forebody model investigated in ground tests is chosen to be 1:3 because of the limited size of wind tunnels. More detailed description of the experimental model, wind tunnels and experimental conditions are presented in sections 4 and 5.

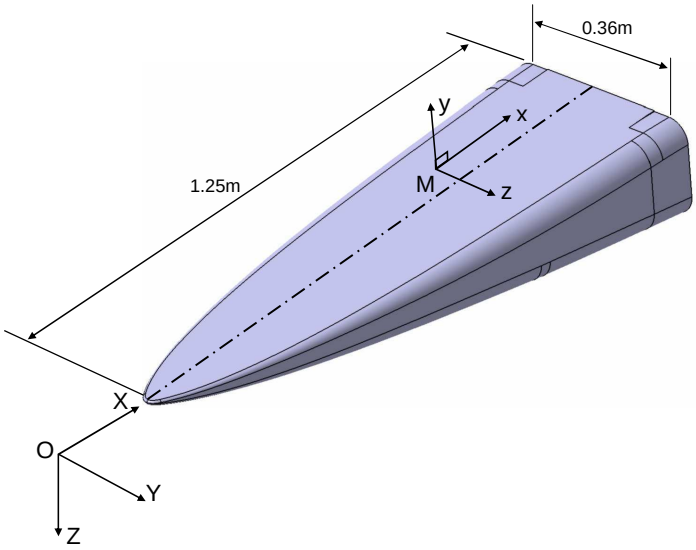

Figure 1.1: CAD view of the forebody.

1.1.2 Thermodynamic and transport models

Static conditions in flight (taken from the 1976 US Standard Atmosphere), conditions on the wall are gathered in table 1.1. In all calculations presented hereafter, air is a mixture

Table 1.1: Flight conditions.

M_∞	Alt. (km)	P_∞ (Pa)	T_∞ (K)	M^e	T_w (K)
4	20	5475	216.6	$3.4 \sim 3.6$	$800 \sim 900$
6	25	2512	221.6	$4.2 \sim 5.0$	$1500 \sim 1650$
8	30	1172	225.5	$5.2 \sim 6.1$	$2500 \sim 2700$

of N_2, O_2, Argon and CO_2, as defined in Alexander Burcat's thermodynamics database [14]. It differs slightly from the US Standard Atmosphere as reported in table 1.2. Using Burcat's composition, the molar mass of air is $W_{air} = 28.96518\,\mathrm{kg/kmol}$.

Isobaric heat capacities of single components are given as coefficients of 4^{th} order polynomial fits for two ranges of temperature : 80 K-1000 K and 1000 K-6000 K. Since at high altitude, static temperatures are in the low-range limit, only the high temperature range is retained from Burcat. At low temperatures, data from Lemmon *et al.* [15], accurate from 80 K to 2000 K are used instead, for N_2 and O_2 (Lemmon *et al.* do not provide any value for CO_2). The two curves are matched numerically at 1000 K. Then, heat capacity of air is computed from single components properties as a mass-weighted average for each temperature range. The resulting global fit $C_{p,air}(T)$ is given in table 1.3, and is shown on figure 1.2.

$$C_{p,air}(T) = \sum_\alpha Y_\alpha C_{p,\alpha}(T) = C_{p0} + C_{p1}T + C_{p2}T^2 + C_{p3}T^3 + C_{p4}T^4 \tag{1.1}$$

Table 1.2: Air composition (mole fractions).

Component	A. Burcat [14]	US Std. Atm.	W (kg/kmol)
N_2	0.780 840	0.780 840	28.013 48
O_2	0.209 476	0.209 476	31.998 80
Ar	0.009 365	0.009 340	39.948 00
CO_2	0.000 319	0.000 314	44.009 80
	1.000 000	0.999 970	

Table 1.3: Polynomial coefficients for isobaric heat capacity of air (J/kg.K)

T(K)	C_{p0}	C_{p1}	C_{p2}	C_{p3}	C_{p4}
80-1 000	1005.451375	-0.039995848	$8.21409\ 10^{-6}$	$4.98177\ 10^{-7}$	$-3.32144\ 10^{-10}$
1 000-6 000	878.5374285	0.369200531	-0.000127397	$2.05949\ 10^{-8}$	$-1.23408\ 10^{-12}$

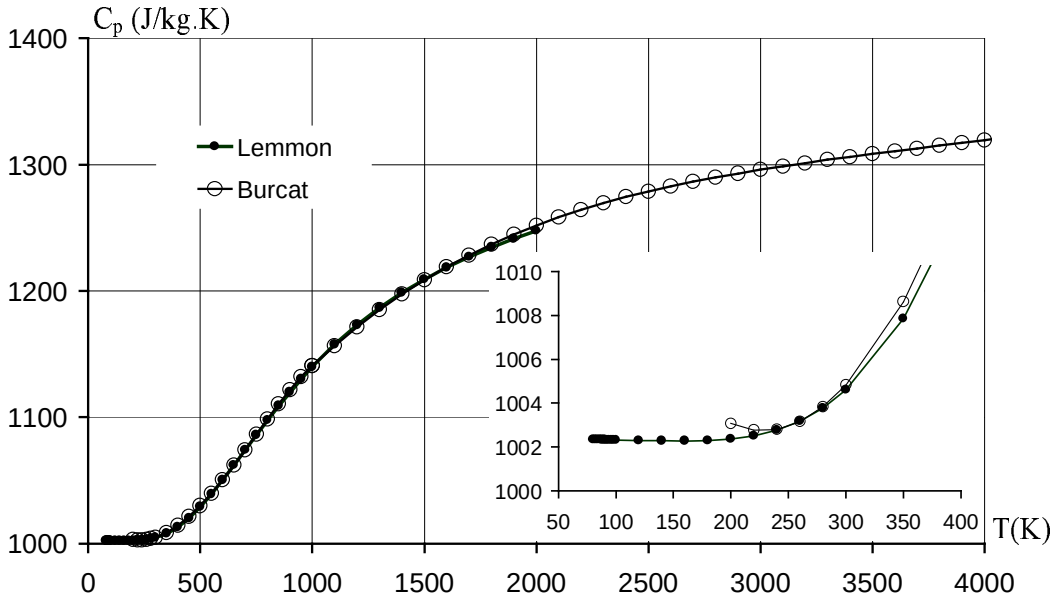

Figure 1.2: Heat capacity of air.

The viscosity $\mu(T)$ of air is calculated with Wilke's mixing formula [16]

$$\mu = \sum_{\alpha=1}^{N_{sp}} \frac{X_\alpha \mu_\alpha}{\sum_{\beta=1}^{N_{sp}} X_\beta \phi_{\alpha\beta}} \quad ; \quad \phi_{\alpha\beta} = \frac{\left(1 + \sqrt{\frac{\mu_\alpha}{\mu_\beta}} \left(\frac{W_\beta}{W_\alpha}\right)^{1/4}\right)^2}{\sqrt{8\left(1 + \frac{W_\alpha}{W_\beta}\right)}} \tag{1.2}$$

in which single component values $\mu_\alpha(T)$ are obtained from the CHEMKIN II [17] transport model based on the kinetic theory. The same method is applied for the thermal conductivity $k(T)$ of air, changing $\mu_\alpha(T)$ to $k_\alpha(T)$. Polynomial fits are applied to (1.2), of the 5^{th} and 3^{rd} orders for μ and k respectively (see table 1.4), accurate in the range 100K-5000K.

The thermodynamic and transport model have been validated [18] on the classic $M_e = 10$ adiabatic flat-plate of Malik and Anderson [19].

Polynomial fit for viscosity $\mu(T)$ (kg/m.s) and thermal conductivity of air are:

$$\mu_{air}(T) = \mu_0 + \mu_1 T + \mu_2 T^2 + \mu_3 T^3 + \mu_4 T^4 + \mu_5 T^5 \quad (1.3)$$

$$k_{air}(T) = k_0 + k_1 T + k_2 T^2 + k_3 T^3 \quad (1.4)$$

Table 1.4: Polynomial coefficients for viscosity $\mu(T)$ (kg/m.s) and thermal conductivity of air $k(T)$ (W/m.K)

μ_0	μ_1	μ_2	μ_3	μ_4	μ_5
2.9141 10^{-6}	5.8921 10^{-8}	-2.6383 10^{-11}	9.3607 10^{-15}	-1.6670 10^{-18}	1.1392 10^{-22}
k_0	k_1	k_2	k_3		
5.0968 10^{-3}	7.2304 10^{-5}	-8.9331 10^{-9}	7.0777 10^{-13}		

1.1.3 Calculation setup and grid requirements

Figure 1.3 shows the computational mesh of the forebody lying "on the back" or "upside-down" to make the area of interest visible. For meshing conveniences, a vertical cutting plane separates the nose region from the body region, 0.04m downstream from the nose tip. In the nose region, the mesh is hexahedral and unstructured (figure 1.4), and in the body region of interest for the LST calculations in black in figure 1.3, the mesh is fully structured.

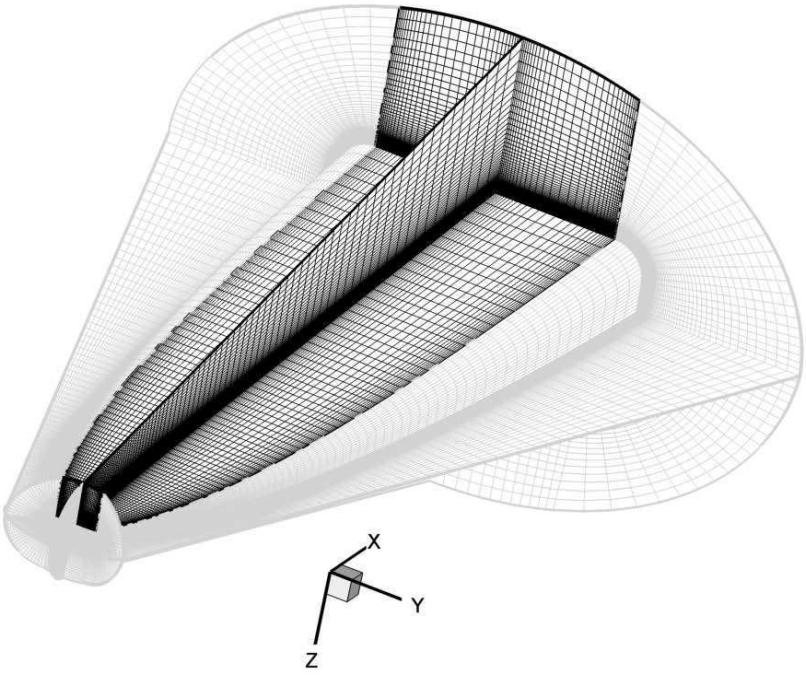

Figure 1.3: Overview of the computational mesh, showing the zone of interest (ZI) in black.

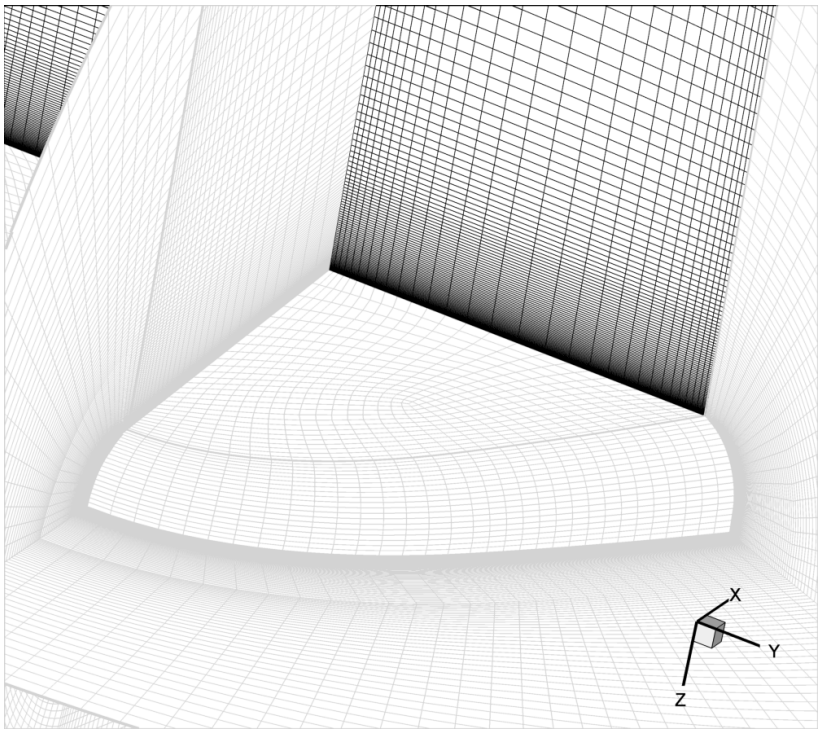

Figure 1.4: Detail of the unstructured mesh of the nose region. Mesh #4.

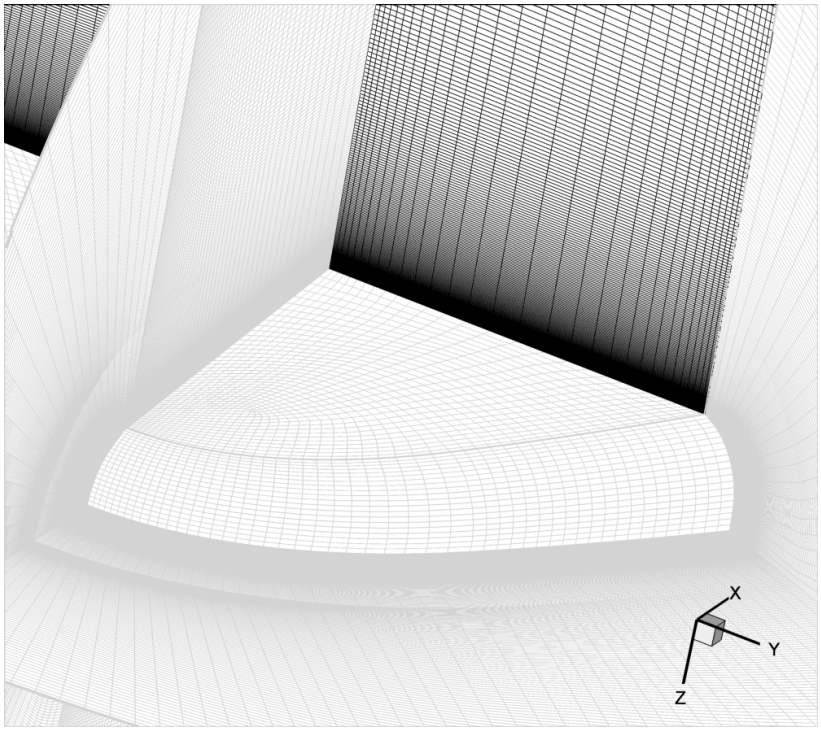

Figure 1.5: Detail of the unstructured mesh of the nose region. Mesh #6.

The grid convergence of the mean flow has been investigated by building different meshes, whose parameters are gathered in table 1.5.

Table 1.5: Numbers of cells for different meshes.

	mesh #1	mesh #2	mesh #3	mesh #4	mesh #5	mesh #6	mesh #7
ZI : X	56	90	90	90	95	90	90
ZI : Y	32	32	40	60	72	60	60
ZI : Z	71	101	101	101	141	201	201
ZI : total	127232	290880	363600	545400	964440	1085400	1085400
Total	$9.0\ 10^5$	$1.7\ 10^6$	$2.0\ 10^6$	$2.0\ 10^6$	$3.3\ 10^6$	$4.5\ 10^6$	$5.1\ 10^6$

- Meshes #1 to #4, #6 and #7 are designed for $M_\infty = 6$ and 8.
- Meshes #6 and #7 contain the same number of points in spanwise and streamwise directions as Mesh #4 in ZI but the number of points normal to the wall is increased from 101 to 201. The mesh in the nose region has also been refined. Figure 1.5 shows details of mesh #6 in the nose region.
- Mesh #7 is built with the aim of a better resolution of the boundary layer compared to other meshes. For that 100 points were in the first 3.5 mm layer with height of the first cell 0.015 mm. The number of points on side walls was also increased from 20 to 30.
- Mesh #5 is designed for $M_\infty = 4$. In this latter case, the size of the computational domain has been increased to avoid numerical reflection of the shock wave on the external boundary.

Examples of streamwise and spanwise velocity profiles obtained for different meshes, at $X = 0.5\,\text{m}$ $Y = 0\,\text{m}$ (plane of symmetry) and at $X = 0.5\,\text{m}$ and $Y = 0.05\,\text{m}$ are shown in figures 1.6, 1.7 and 1.8. Big differences between profiles are observed in the symmetry plane. The particular profile in the symmetry plane is obtained by averaging of the neighbor profiles on the right and left sides of the symmetry plane. It is found that near the plane of symmetry, longitudinal vortical structures exist and need high mesh resolution in the transversal direction to be properly described. The flow topology will be presented and discussed in subsection 1.1.5.

For each mesh, the height of the first cell is less than 0.05 mm all along the body, which is enough to capture both the shock, as it can be seen in figure 1.9, and the boundary layer. Nevertheless as visible on figures 1.10 and 1.11 contours in the nose region even for mesh#7 remain rough despite the increasing number of points. A discussion and an additional analysis of the flow in the nose region are given in section 1.1.4.

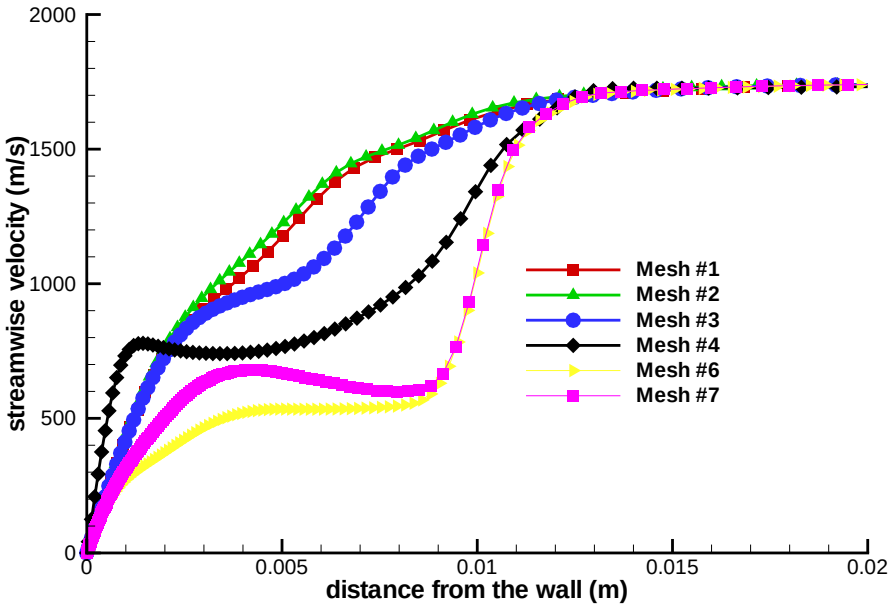

Figure 1.6: Streamwise velocity for different meshes in the symmetry plane. $M_\infty = 6$, AoA=4°, $X = 0.5$m, $Y = 0$m

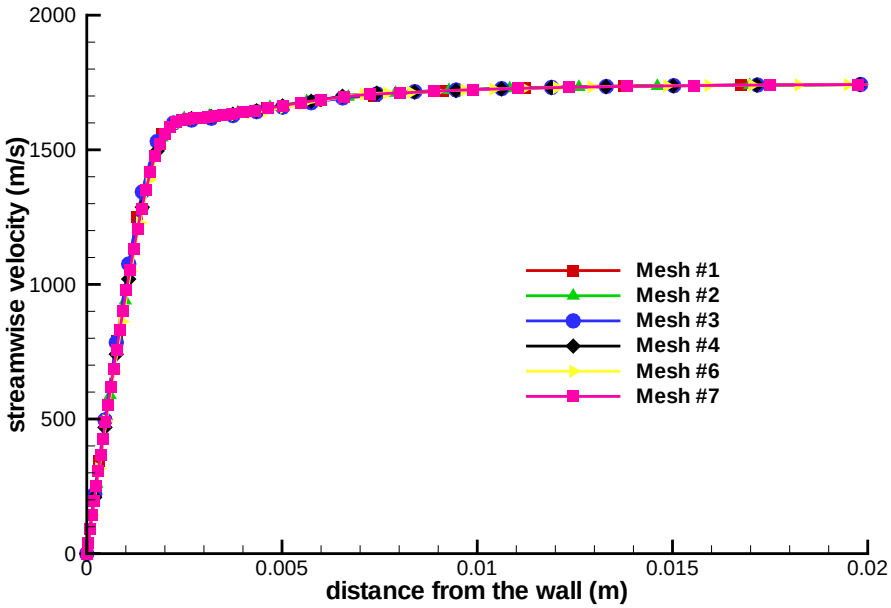

Figure 1.7: Streamwise velocity profiles for different meshes. $M_\infty = 6$, AoA=4°, X=0.5 m, Y=0.05 m

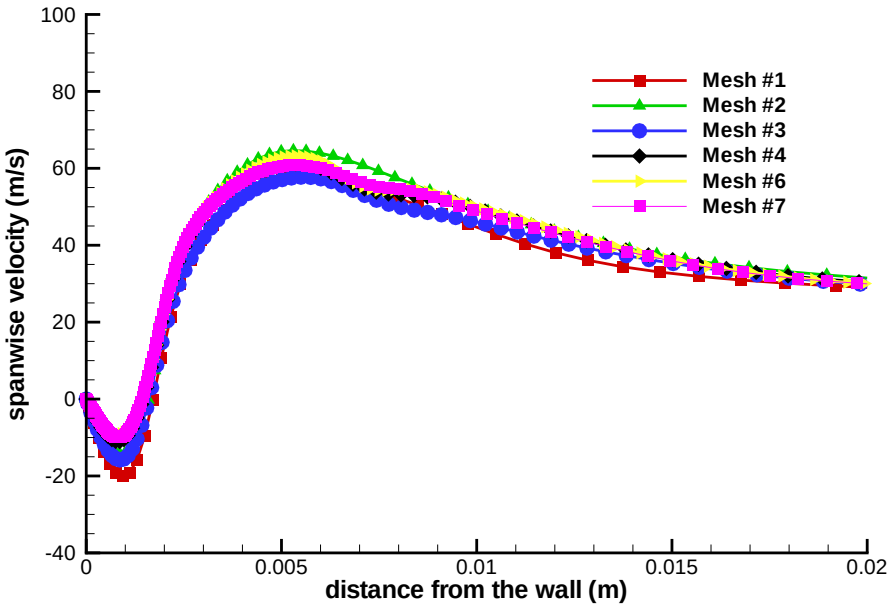

Figure 1.8: Spanwise velocity profiles for different meshes. $M_\infty = 6$, AoA=4°, X=0.5 m, Y=0.05 m

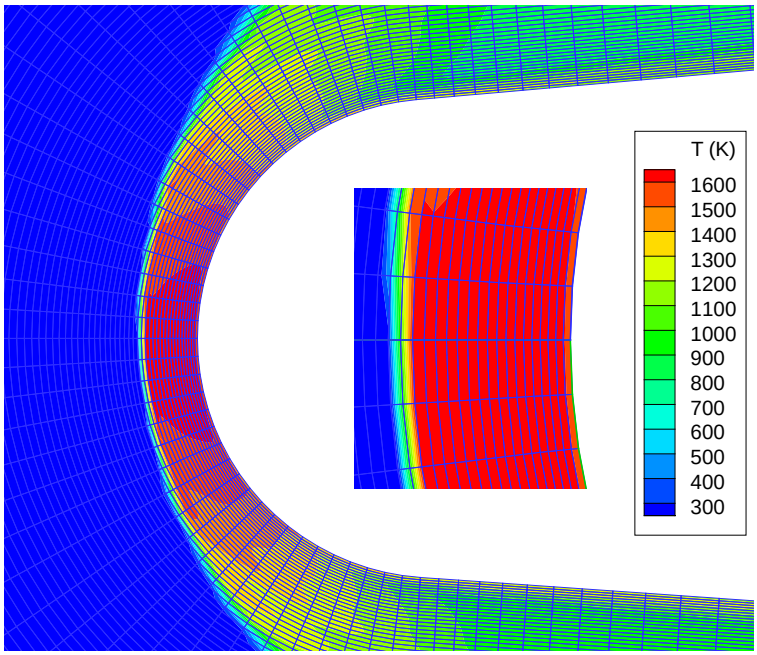

Figure 1.9: Resolution of the shock in the plane of symmetry, $M_\infty = 6$, mesh #4.

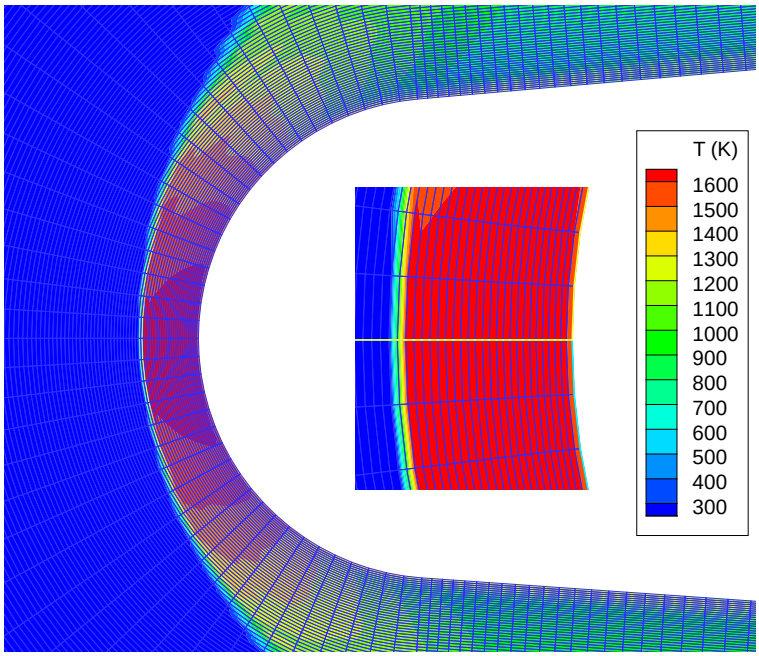

Figure 1.10: Resolution of the shock in the plane of symmetry, $M_\infty = 6$, mesh #6.

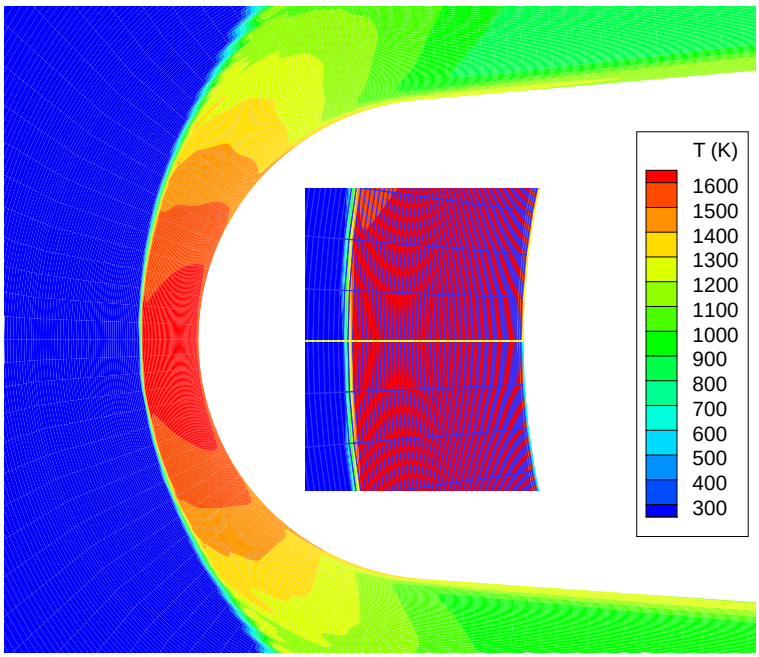

Figure 1.11: Resolution of the shock in the plane of symmetry, $M_\infty = 6$, mesh #7.

Calculations have been performed using the 2^{nd} order upwind implicit density-based solver available in FLUENT® 6.3.26, with Roe's flux. The CFL number is increased progressively from 0.1 to 1.5, since the calculation starting from initial conditions diverges if CFL > 0.1. The wall is considered as either adiabatic, or radiating with emissivity $\varepsilon = 0.8$ in thermal equilibrium with the flow, which is the most representative of flight conditions. Far-field non-reflecting characteristic-based boundary conditions are imposed. This boundary condition is not very accurate in the exit section, between the wall and the sonic line in the BL, but it affects only the last two rows of cells. Convergence is obtained after 15000 iterations, taking about 50 h of CPU time on 4 Intel bi-Xeon 3.2 GHz (8 processors local cluster of ICARE) for mesh #4. Computations on mesh #7 (5 million cells) take more than 90% of RAM (2 GB×8) of our local cluster, that shows the limitation on the maximum number of cells of a mesh that can be computed. Convergence criteria are based on numerical residuals, on mass balance and on wall temperature and skin friction in the plane of symmetry of the vehicle. The time evolutions of numerical residuals and mass balance are shown in figures 1.12 and 1.13. Numerical residuals are not good indicators of convergence since boundary conditions are not very accurate in the exit section. Mass balance criteria reaches value less than 10^{-6}. Variation of temperature field in the symmetry plane after 18000 and 38000 iterations is shown in figure 1.14 for mesh #6. The flow field changes everywhere less than 0.01% except in local place where the shock moves a little and where the variation increases up to 0.1%. Figure 1.15 shows an example of the convergence history of the temperature distribution in the plane of symmetry for a radiating wall for mesh #4. The influence of boundary conditions in the exit sections is also observed. The red curve is the converged solution in the case of an adiabatic wall. The solution converges first upstream, then downstream which is typical of supersonic flows and independent from meshes. Moreover, one can see that a radiating wall is about 500 K colder than an adiabatic wall at Mach 6 in flight.

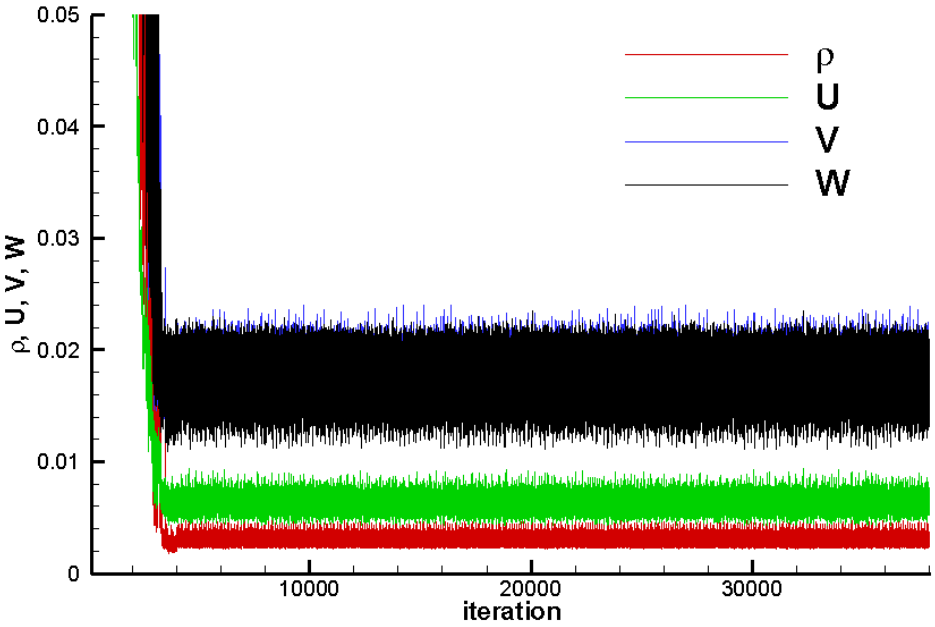

Figure 1.12: The time evolution of numerical residuals.

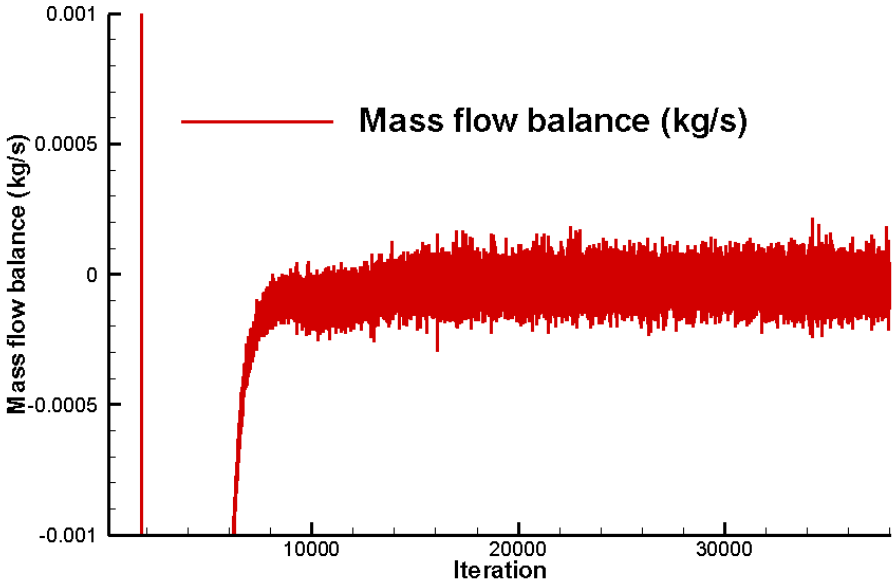

Figure 1.13: Time evolution of mass balance through inlet and outlet. (Mass flow through inlet is 37.7 kg/s).

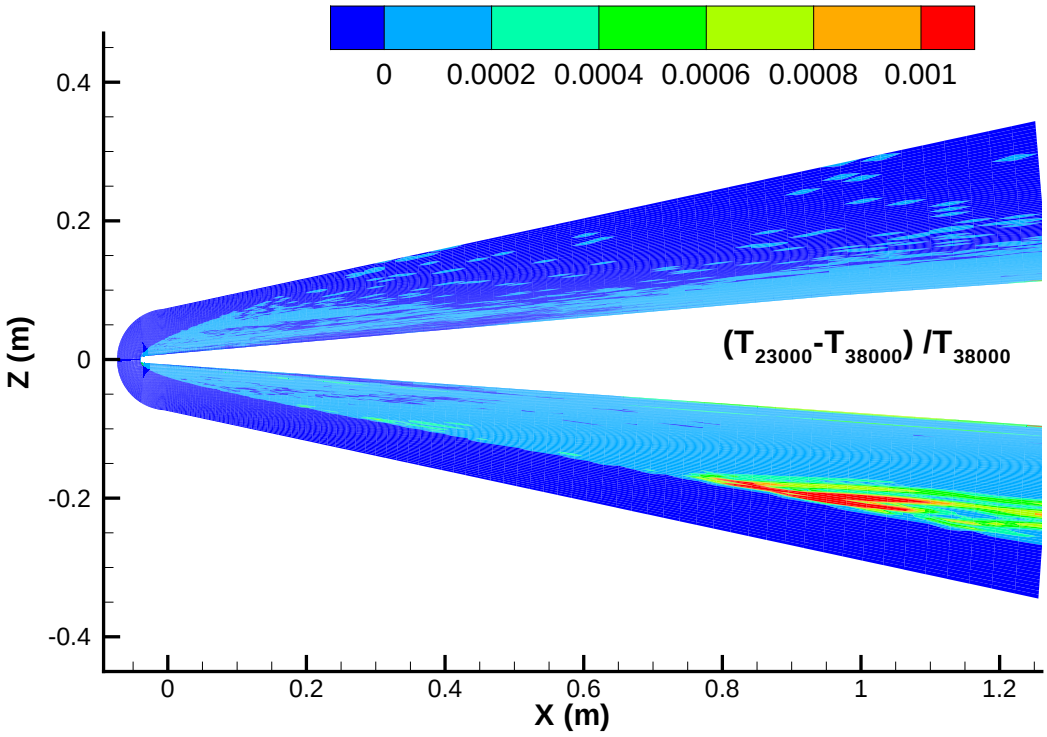

Figure 1.14: Variation of temperature field between 23000 and 38000 iterations.

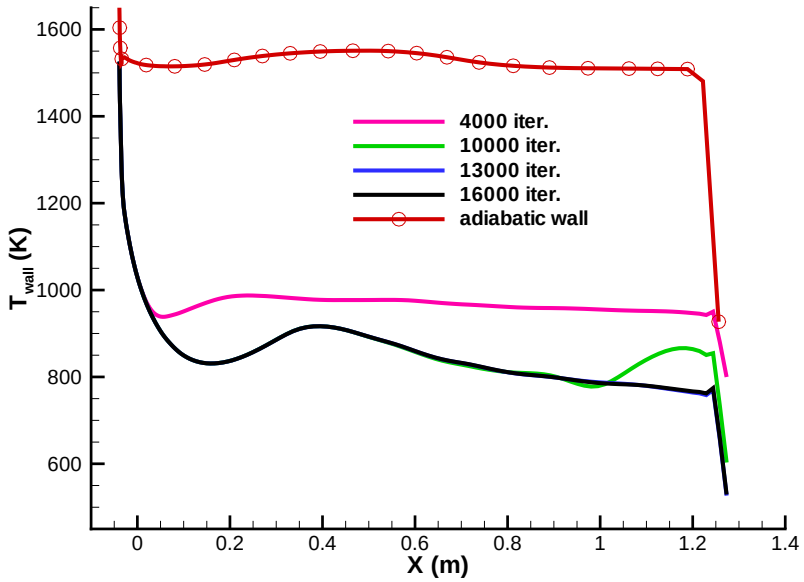

Figure 1.15: Wall temperature distribution in the symmetry plane.

A main technical problem with FLUENT® is the complexity of extracting profiles from unstructured data (although the mesh is built structured in the zone of interest). It has been necessary to write a specific UDF (User Defined Function) in order to extract data from cell centers to obtain accurate profiles. UDF code is listed in appendix. Once data are extracted, they must be ordered and formatted for post-processing (TECPLOT®) and for the LST code. A FORTRAN code has been written for that purpose: the algorithm considers mesh lines that are orthogonal to the wall. Hence, a simple change of coordinate from the global reference frame to a wall fitted coordinate system (a 4 degree Y-rotation) allows an easy sort of data by constant coordinates. A routine with complex algorithm that allows extracting data from the entire structured domain has also been written. This procedure was used to draw stream lines on the body (an example see in figure 1.30). It takes about 2-3 hours of CPU time of PC to classify profiles and to build structured data in the whole domain (except the unstructured nose region). Examples of extracted data are presented on figure 1.16.

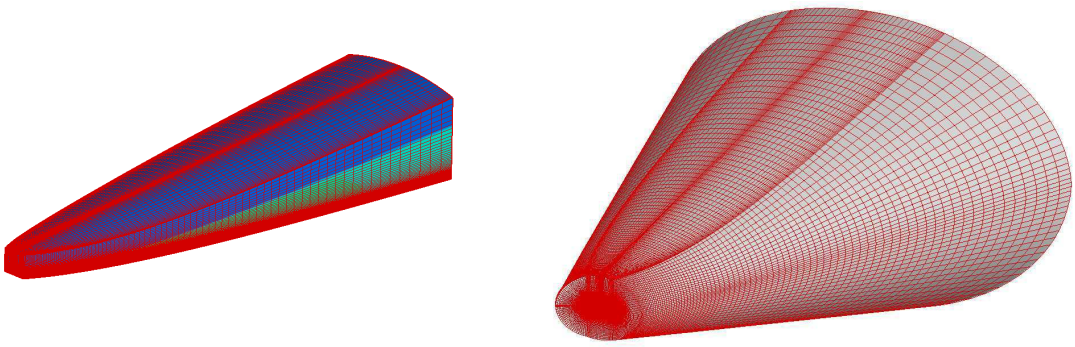

Figure 1.16: Extracted data from FLUENT® in to TECPLOT®

1.1.4 The problem of the shock resolution

Before analyzing the mean flow in section 1.1.5, we discuss the problem of the shock resolution in the nose region. As it was noted previously, data in the symmetry plane in figures 1.10 and 1.11 are obtained by averaging of the neighbor layers. To be sure that those non-uniformities of the flow in these figures do not result from the numerical procedure of averaging of the neighbor layers, we need to analyze the flow field in each layer built on the cell center separately. Data in the cell centers of the structured part of the mesh can be obtained with the same procedure used for data in ZI and previously described. Result of such classification in the nose region is shown in figure 1.18. This mesh is staggered to the cell centers of mesh of figure 1.4. Mesh above flat surfaces of the nose is unstructured as shown in figure 1.4 and obtaining data in the cell centers in this region is a complicated task. Figure 1.19 presents the temperature field in the first row of the cells adjacent to the symmetry plane for mesh #4. The shock wave follows the mesh lines and when the shock changes from one mesh line to another, the flow is locally disturbed. Some selected profiles in figure 1.20 show the value of the disturbances and the distance from the shock to the wall. Increasing the mesh resolution both normal to the wall from 101 to 201 and in the radial direction from 20 points to 30 points reduces the zone of non-uniformity, as visible in figure 1.21 and figure 1.22. Removing or at least minimizing oscillations in the flow would require increasing the mesh resolution in all directions. However, we could not refine the mesh both for the shock and the boundary layer because mesh #7 is already our limit in computations. But if we follow the development of these disturbances downstream, we can see their dissipation. Figures 1.23 and 1.24 show the flow evolution downstream following side walls. Contours of temperature field become smooth before the cutting plane downstream of which the LST is applied. Two surfaces which cross ZI are also presented in figures 1.25 and 1.27. Some non-uniformity in the flow remains in the lateral parts of the body. It indicates a local lack of grid resolution. A comparison of longitudinal and transversal velocity profiles in the ZI, obtained with different meshes, is shown in figures 1.7 and 1.8. Visually, the effect of the numerical oscillations in the nose region due to the poor resolution of the shock seems negligible. However, the LST is very sensitive to the quality of mean flow profiles which should be smooth up to second derivatives. A posteriori analysis of the LST results for different meshes (section 1.2.4) will allow to conclude about Fluent ability to produce acceptable profiles for LST applications.

We should also mention the carbuncle phenomenon [20, 21] which is a numerical instability that affects the computation of bow shock waves around blunt bodies in supersonic flows when the grid is almost aligned with the shock 1.17. Although this phenomenon seems quite different from the present wriggles, it may have a common origin, but this need further analysis for a definitive conclusion.

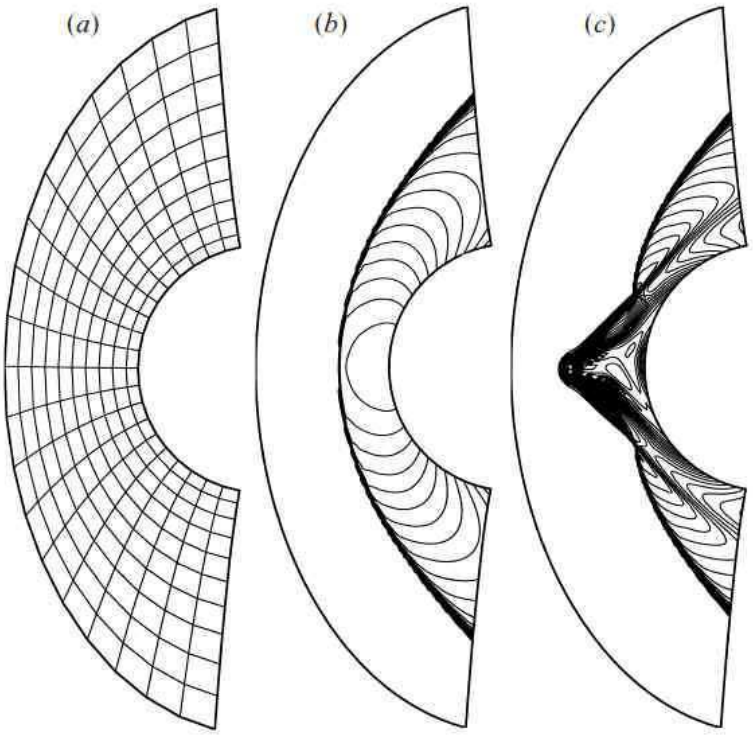

Figure 1.17: An illustration of the carbuncle phenomenon, taken from [21].

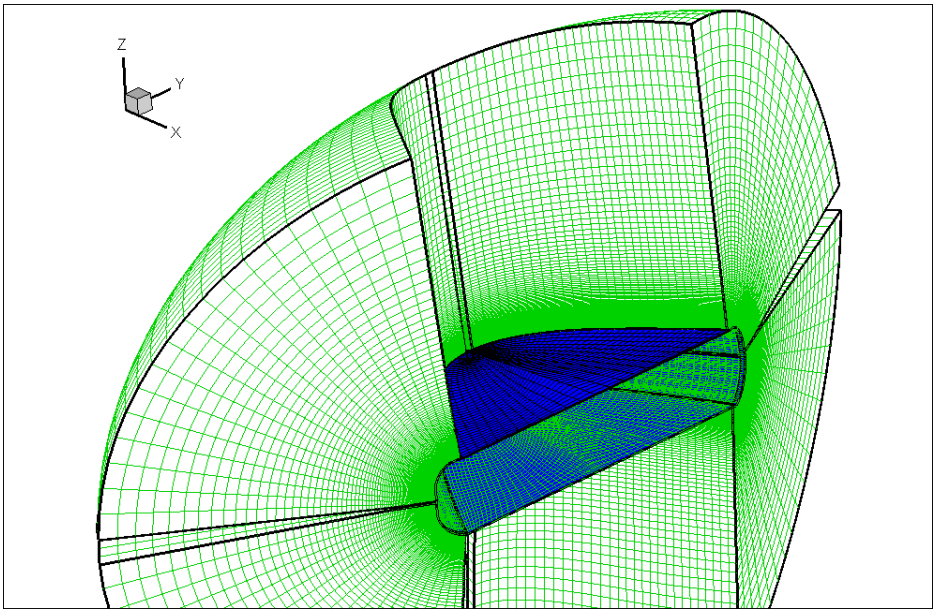

Figure 1.18: Structured part of mesh in the nose region.

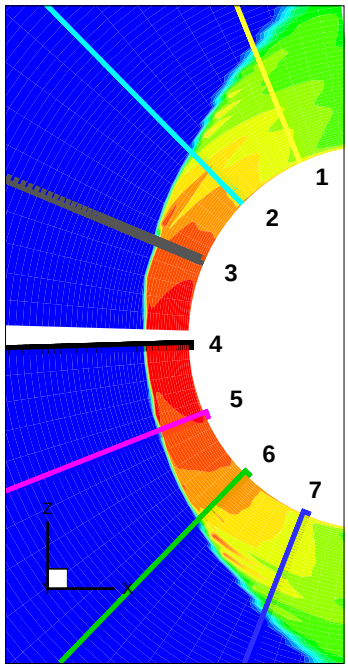

Figure 1.19: Temperature field in the first row of cells adjacent to the symmetry plane. Mesh #4.

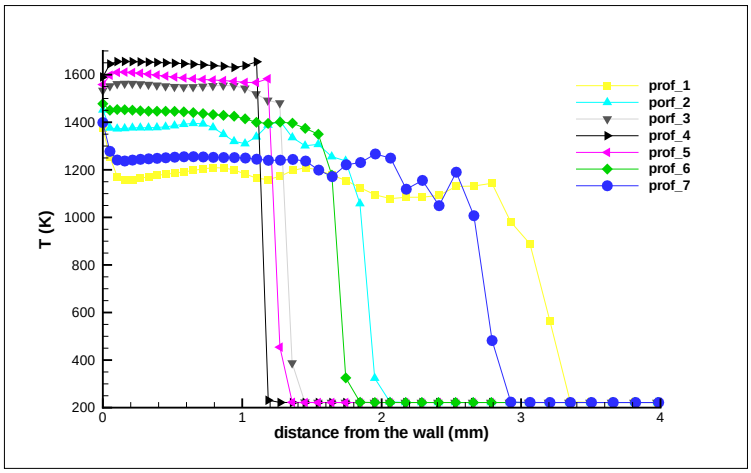

Figure 1.20: Temperature profiles along the lines indicated by corresponding colors in figure 1.19.

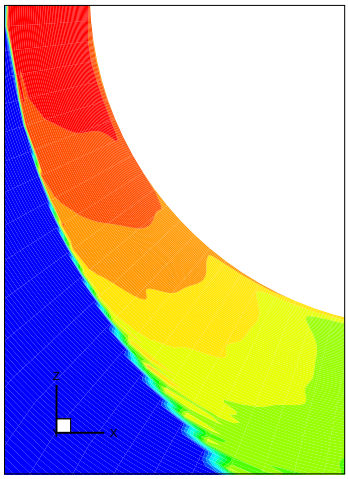

Figure 1.21: The same as figure 1.19. Mesh #7.

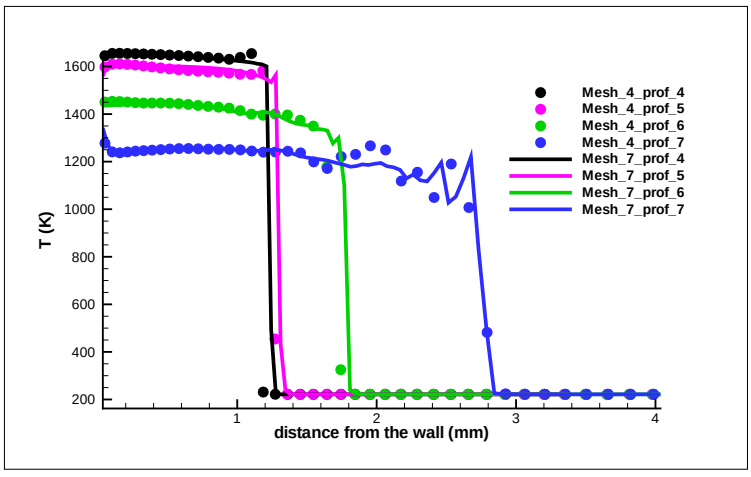

Figure 1.22: Same as figure 1.19. Mesh #7.

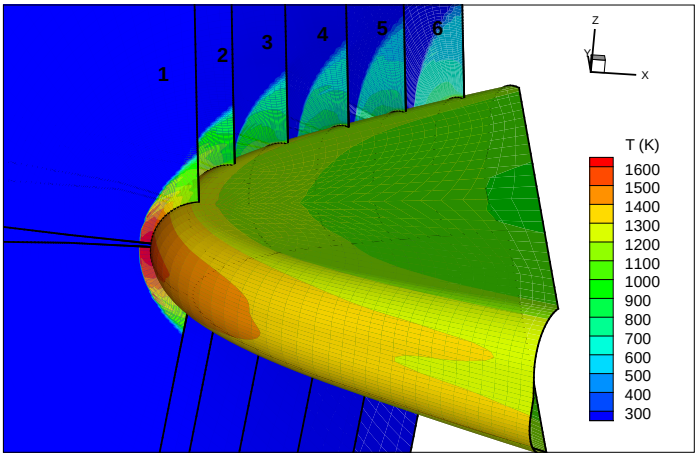

Figure 1.23: Position of chosen planes.

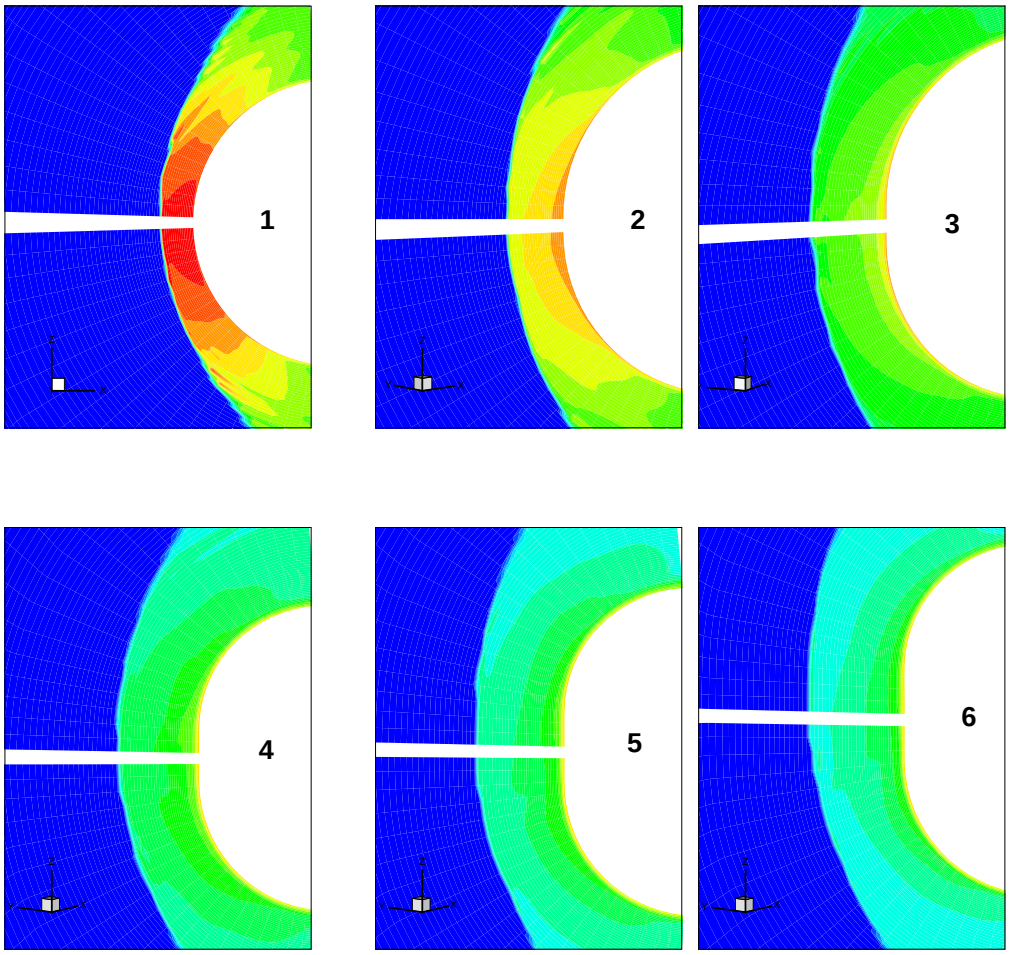

Figure 1.24: Illustration of the dissipation of shock-induced oscillations.

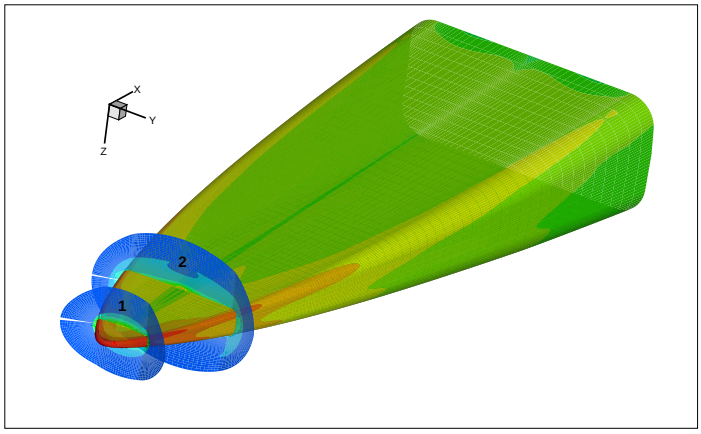

Figure 1.25: Position of surfaces crossing ZI.

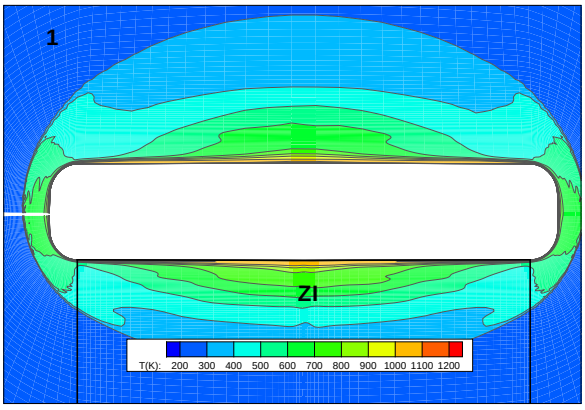

Figure 1.26: Temperature field from figure 1.25, plane 1.

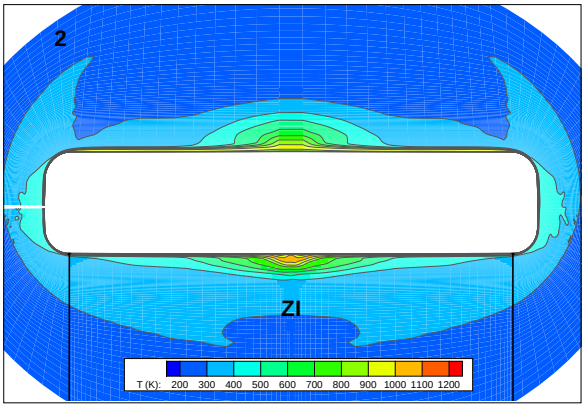

Figure 1.27: Temperature field from figure 1.25, plane 2.

1.1.5 Mean flow analysis and main results

All the results presented hereafter have been obtained with mesh #4 for $M_\infty = 6$ and 8, and with mesh #5 for $M_\infty = 4$. During flight, different angles of attack (0° to 8°) and slip angles (0° to 6°) are considered, but the nominal angle of attack (AoA) is 4° and the slip angle is 0° (design conditions).

Topology of the flow

The flow topology is first illustrated at $M_\infty = 6$, AoA of 4° and a radiating wall. The contour of Mach number is displayed on figure 1.28 and 1.29.

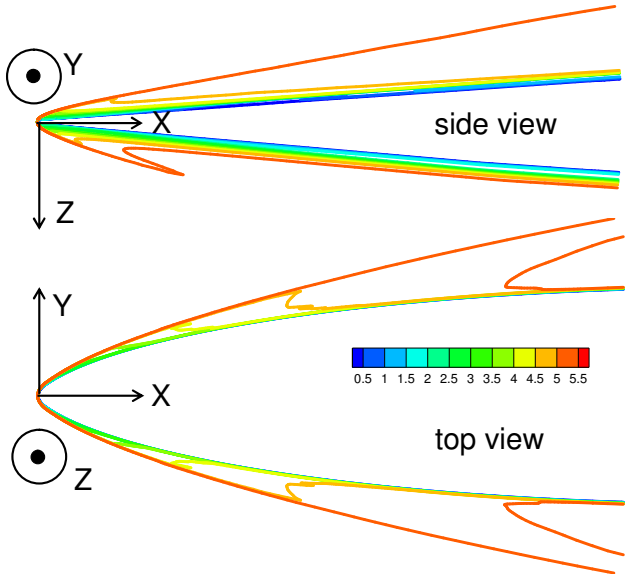

Figure 1.28: Contour of Mach number, $M_\infty = 6$, AoA=4°. Mesh #4.

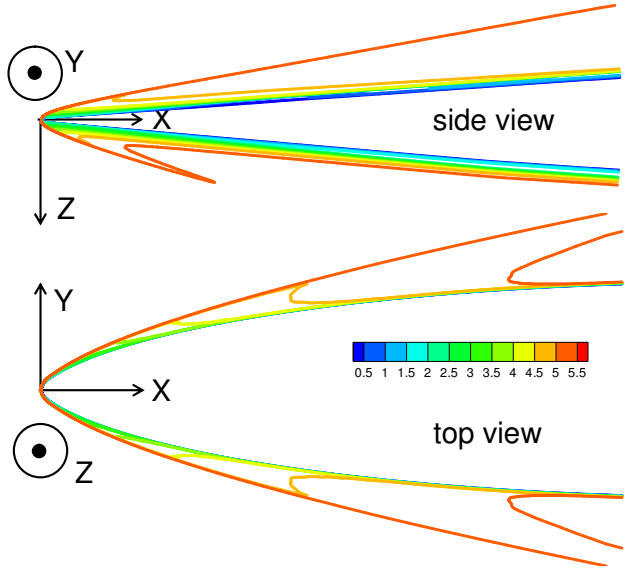

Figure 1.29: Contour of Mach number, $M_\infty = 6$, AoA=4°. Mesh #7.

The distance from the shock to the nose is about 2 mm. This implies very high thermal loads on the tip of the vehicle (see figure 1.9). Moreover, since the shock wave is closer to the lateral than to the upper or lower faces, a pressure gradient drives the near-wall flow from the edge toward the centerline of the vehicle. Isolines of contour of Mach number on top view for mesh #4 are not very smooth compared side view. The reason can be the following: the values on this plane are obtained by averaging of the neighbor rows of cells. In the symmetry plane, profiles are orthogonal to the wall while mesh lines are broken lines on the side walls. Nevertheless, isolines are smooth in the computation with mesh #7. Figure 1.30 shows the streamlines computed from the 1^{st} row of cells above the wall. They converge toward the plane of symmetry, and the near-wall flow rolls-up into a pair of counter-rotating longitudinal vortices on both sides of the symmetry plane. This phenomenon is the same as observed by Kimmel *et al.*[22, 23] on an elliptic cone. These vortices are apparent on figure 1.31, and figure 1.32 shows two additional smaller ones very near the wall on the centerline. The mesh is fine enough to capture properly these vortical structures. The bluntness of the nose induces a bow shock and then an entropy layer (EL) which is mostly visible as a loss in total pressure (figure 1.33). The EL combines with the longitudinal vortices near the plane of symmetry to produce velocity profiles of complicated shapes. Figures 1.34 and 1.35 show the streamwise and spanwise velocity profiles respectively, at $X = 0.6\,\mathrm{m}$. The influence of the vortices is clearly visible at the two first locations ($Y = 0.01\,\mathrm{m}$, $Y = 0.013\,\mathrm{m}$): close to the vertical plane of symmetry, low momentum flow coming from the near-wall region is pulled up (see figure 1.31, mushroom-like shape) and induces the non-monotonicity of the velocity profiles. From $Y = 0.017\,\mathrm{m}$ to $Y = 0.05\,\mathrm{m}$, profiles exhibit a structure characteristic of a mixed boundary-entropy layer. At $Y = 0.07\,\mathrm{m}$, the EL almost disappears and a standard boundary layer profile is recovered. Both crossflow and EL create inflexion points in the longitudinal and transversal profiles and this is very important for stability issues.

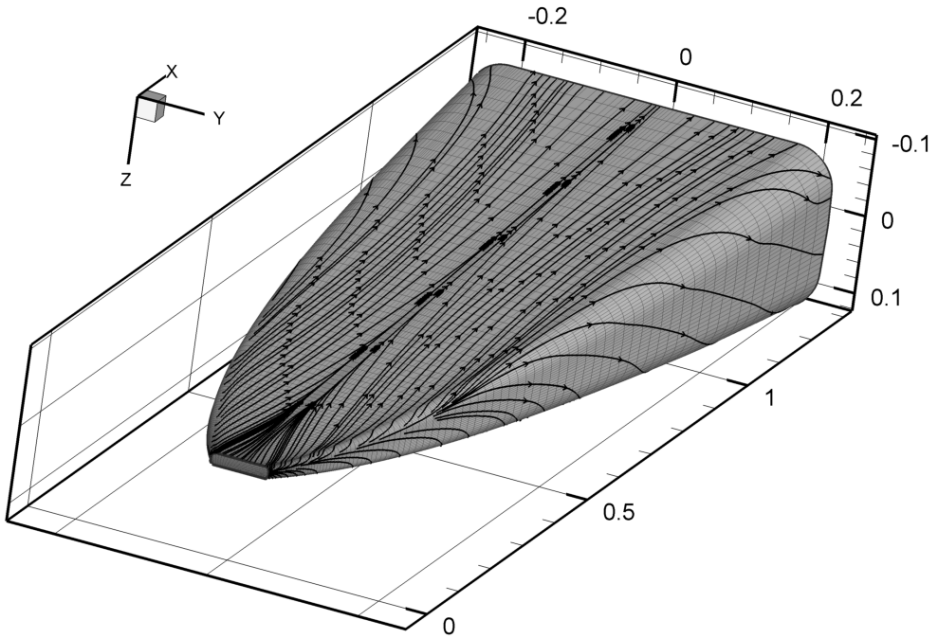

Figure 1.30: Streamlines under the forebody at $M_\infty = 6$, AoA=4°. Axis units are meters.

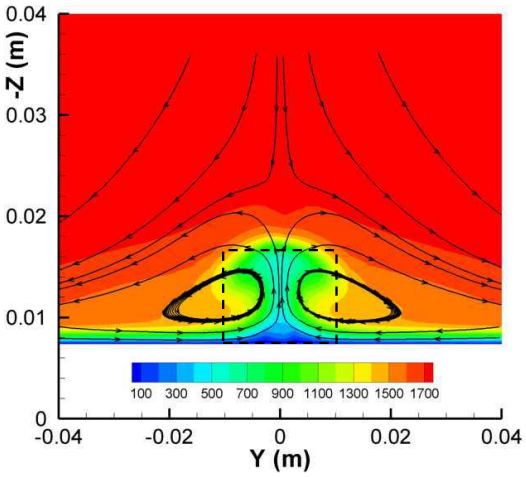

Figure 1.31: Streamwise velocity contours (m/s) and velocity vectors in the cross-section at $X = 0.5\,\mathrm{m}$. Streamlines illustrate the longitudinal vortices.

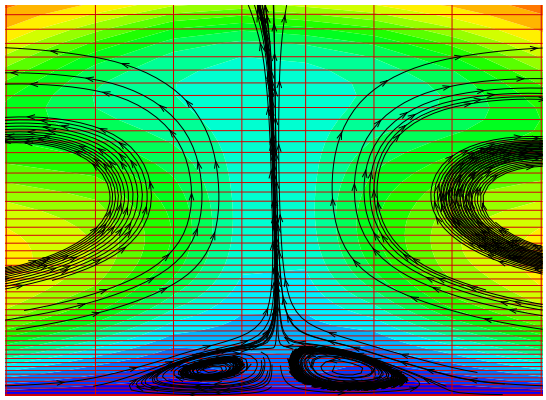

Figure 1.32: Zoom of dashed box from figure 1.31 to illustrate two additional smaller vortices.

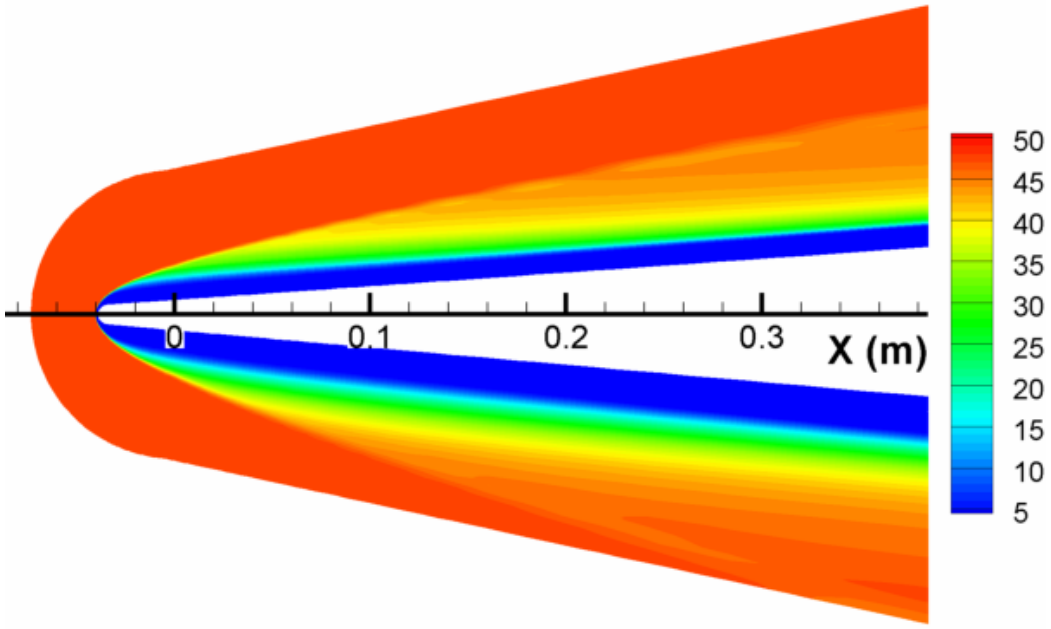

Figure 1.33: Contour of total pressure (bars), side view.

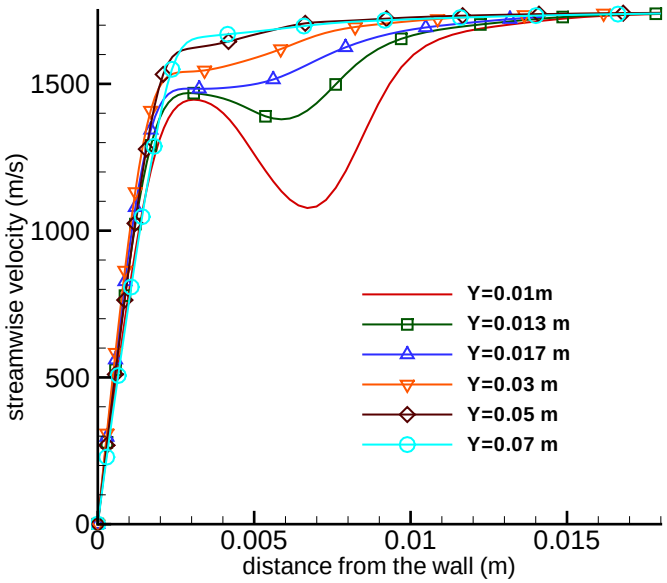

Figure 1.34: Streamwise velocity profiles in the $X = 0.6\,\mathrm{m}$ cross-section.

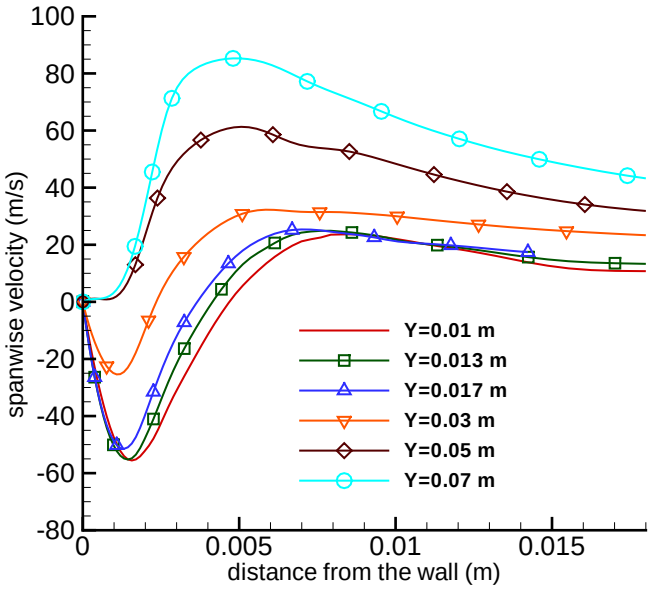

Figure 1.35: Same as figure 1.34: spanwise velocity component.

Effects of Mach number and angle of attack on the flow around the forebody

At $M_\infty = 8$, the topology of the flow is nearly the same as at $M_\infty = 6$. Figure 1.36 shows near-wall streamlines (top and side views) for $M_\infty = 8$, and angle of attack 0° and

4°. Streamwise velocity contours and spanwise velocity vectors in the $X = 0.8$m vertical plane, are displayed on figures 1.37. Increasing the angle of attack increases the spillage of the flow, as it can be clearly seen on the figures.

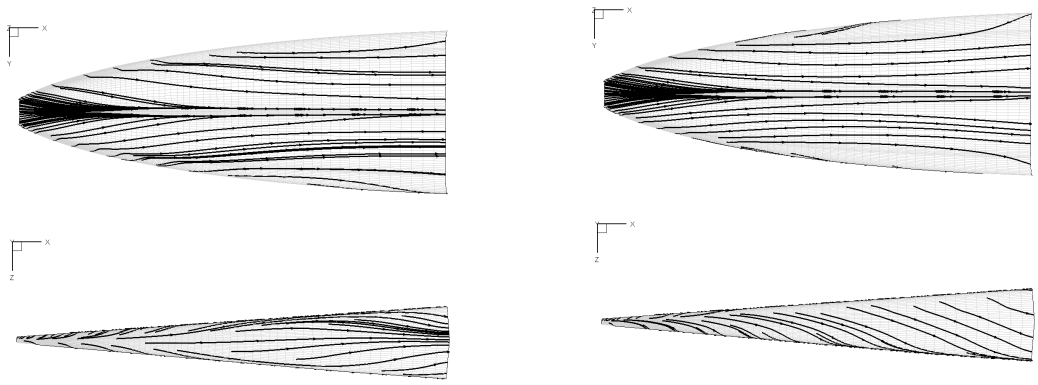

(a) AoA=0°

(b) AoA=4°

Figure 1.36: Streamlines $M_\infty = 8$, top and side view.

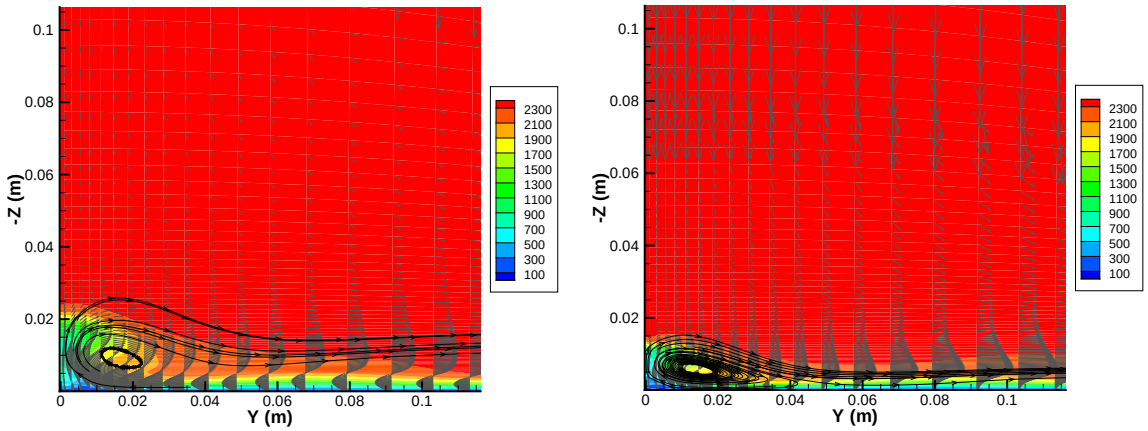

(a) AoA=0°

(b) AoA=4°

Figure 1.37: Streamwise velocity contours (m/s) and velocity vectors in the cross-section at $X = 0.8$ m. Streamlines illustrate the longitudinal vortices at $M_\infty = 8$.

At $M_\infty = 4$, the topology of the flow is slightly different. All streamlines coming from the side of the body converge to an attachment line near the leading edge (figure 1.38). Nevertheless, longitudinal counter-rotating vortices are still observed, and hence are common to all Mach numbers (4 up to 8) and all angle of attack (see figures 1.31, 1.37 and 1.39 for $M_\infty = 4$).

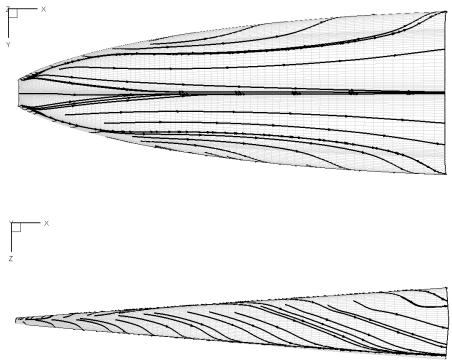

Figure 1.38: Same as figure 1.36: $M_\infty = 4$, AoA=4°.

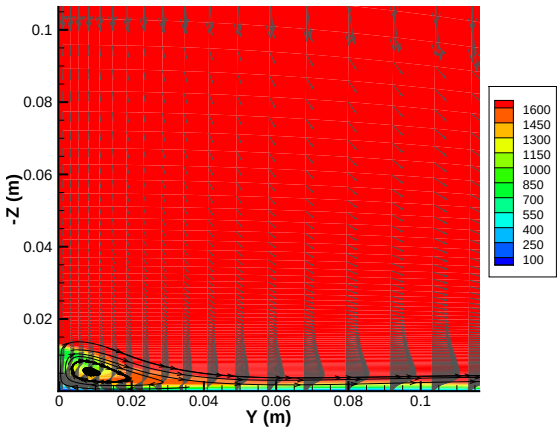

Figure 1.39: Same as figure 1.37: $M_\infty = 4$, AoA=4°.

1.1.6 Boundary layer thickness

A qualitative information about boundary layer thickness is needed to prepare experiments or to compute different empirical transition criteria (used in chapter 2 and 3). But the definition of the edge of the boundary layer is not obvious and is subject to discussion [24]. The method applied here is based on the total enthalpy profile because it is not influenced by the entropy layer due to the curvature of the shock. Starting from the wall, the edge of the BL is found along a normal when the total enthalpy variation is less than 0.01% between two successive mesh points. This method differs slightly from the one proposed by Kimmel *et al.*[22]. Figure 1.40 shows an example of velocity, temperature profiles and variation of total enthalpy for two neighbor locations numbered 1 and 2. Comparison between streamwise velocity contour and boundary layer thickness (black curve) is given in figure 1.41. Figures 1.42, 1.43 and 1.44 show results of the boundary layer thickness at $M_\infty = 6$ and AoA=4° obtained with meshes #4 to #7. Some differences are observed because the method depends on the resolution of profiles. Contour map of boundary layer thickness is less smooth for mesh #4 than for meshes #6 and #7. Results can be improved by a simple linear interpolation (see figure 1.43).

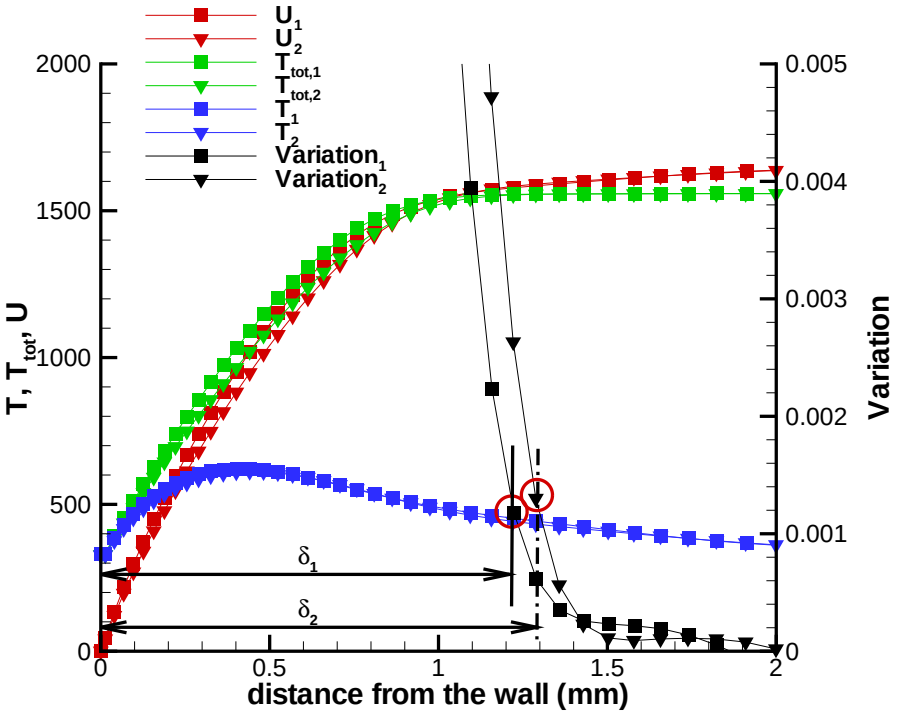

Figure 1.40: U, T, T_{tot} profiles and variation of H_{tot}. Mesh #4.

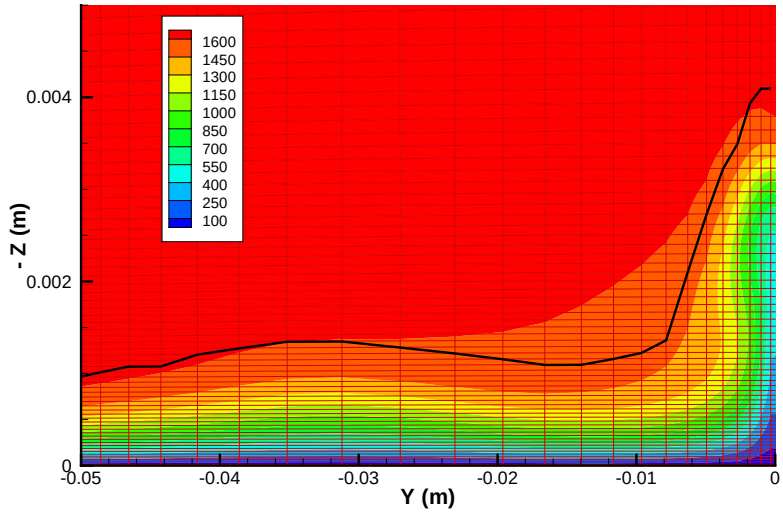

Figure 1.41: Contour map of streamwise velocity (m/s) and boundary layer thickness black curve. Mesh #4.

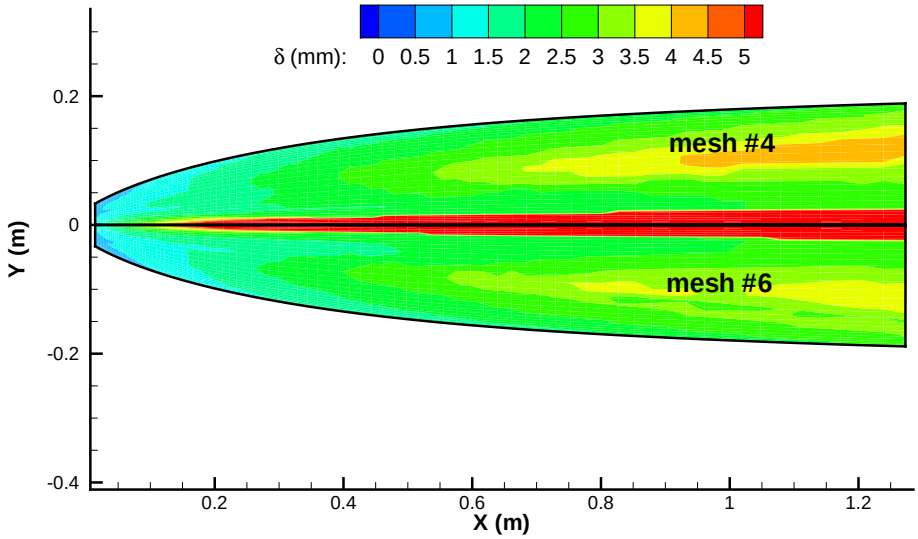

Figure 1.42: BL thickness at $M_\infty = 4$ and $M_\infty = 6$, AoA=4°. Meshes #4 and #6.

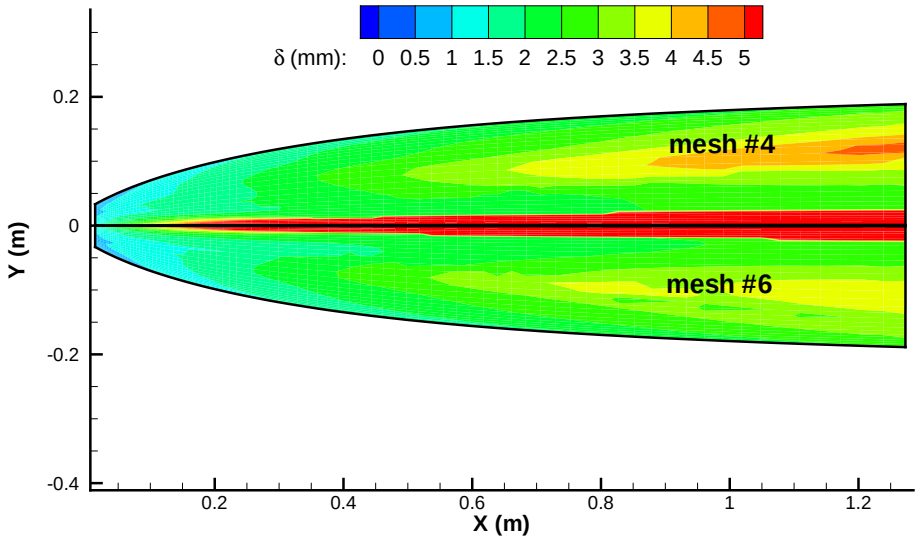

Figure 1.43: Same as figure 1.42: linear interpolation.

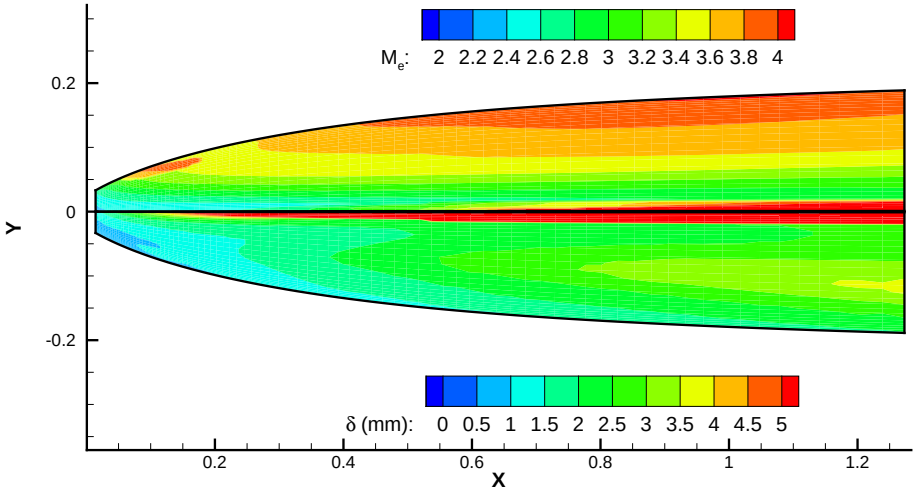

Figure 1.44: BL thickness and edge M number at $M_\infty = 6$, AoA=4°. Mesh #7.

1.2 Part II: LST

Understanding mechanisms involved in the transition process is still a challenging task in supersonic and hypersonic flows, after more than half a century of intensive research. Since the funding paper by Lees and Lin [25], and further developments by Mack [26, 27], Malik [28] and others, numerous experimental and numerical parametric studies on transition in hypersonic flows have been done for flat plates or cones. The effects of Mach and Reynolds numbers, leading edge bluntness, angle of attack (AoA), have been investigated. A recent review has been done by Schneider [5] (see also [29]).

1.2.1 Introduction to LST

At the moment, the only method of industrial application, taking into account theoretically (although incompletely) the destabilizing mechanisms, is the linear stability theory [30]. Local or non-local (PSE) theories may be applied. They both rely on the e^N method and are of comparable efficiency in predicting the point of transition: their difference for a given N may be of the same order of magnitude than the uncertainty on the value of N itself at the transition location. The real interest of non-local theories is to open the way for non linear theories that allow a deeper understanding of the transition processes. However, $N \approx 10$ is a currently accepted value for the transition to occur in flight conditions. In wind tunnels, this value may be decreased dramatically [31].

The LST applies to mean-flow profiles, and is very sensitive to their accurate description. In case of flat plates or sharp cones at zero AoA, self-similar mean-flow profiles are at disposal through the Levy-Lees and Mangler transformations. In case of a real-shape forebody, no such quasi-analytical solutions exist and one has to use a CFD code to calculate the 3D mean-flow. Since strong shock-waves are present in hypersonic flight conditions, robust solvers are needed. Until quite recently, wall-bounded flows were obtained by Euler/BL weak or strong coupling, but 3D effects and flow separation were difficult to handle. Navier-Stokes solutions have already been obtained for stability calculations in case of a small-scale (L $\approx$ 0.25m),

axi-symmetric model at ONERA (France) [32], allowing for very well resolved BL profiles (1^{st} cell = 5 μm). In this sense the present study for a full scale forebody, computing the mean flow with CFD, is original.

1.2.2 Path to transition

It is interesting to get an overview of transition mechanisms before starting to explain the LST. Reshotko *et al.*[33] proposes several paths to turbulence for wall-bounded flow, according to the level of external disturbances. Indeed, transition is the answer to the "complex oscillator [11]" that is the flow to environmental disturbances. In any case, disturbances have first to enter the boundary layer through receptivity mechanisms, which can be investigated through direct numerical simulation [34].

Receptivity describes perturbations enter the boundary layer and their initial amplitude. Once entered into the boundary layer disturbances will be amplified or damped depending on the system stability.

Figure 1.45 presents paths to transition under which the perturbations are amplified by the boundary layer instability and will actually create unstable waves. Only paths A, B and C are relevant to external flows. Paths D and E correspond to levels of disturbances found only in internal flows (turbomachinery, for example). Figure 1.46 offers an interpretation of paths A, B and C. On this graph, E represents the energy of a disturbance and x_c the abscissa at which the disturbance starts to grow in path A. E_t corresponds to limit where transition occurs.

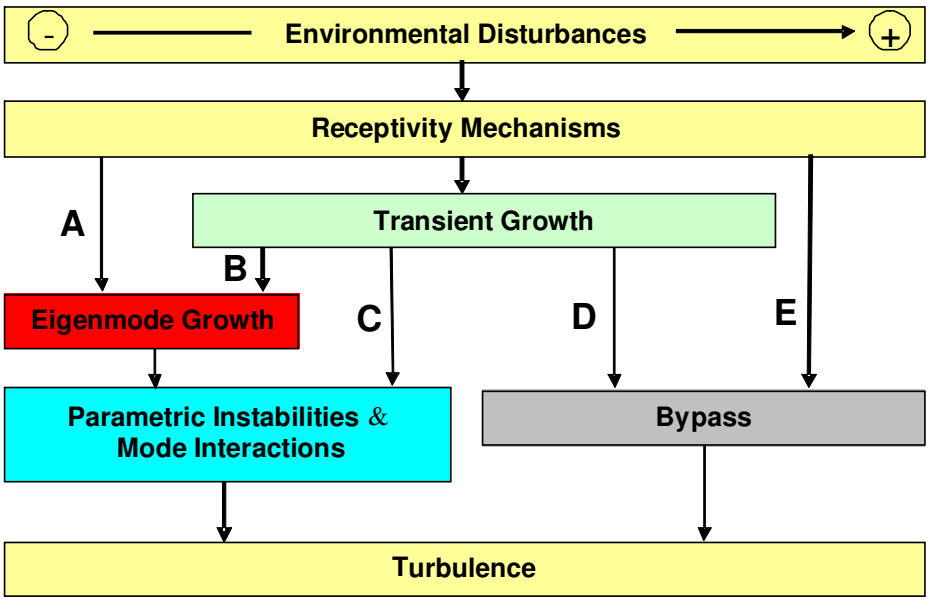

Figure 1.45: Paths to transitions [33].

Path A. Historically, this is the first transition mechanism which was discovered. This is the traditional path for low disturbance environments. The disturbances excite the modes of the boundary layer. If some of these modes are unstable, then they can rise to waves that will grow spatially, during their displacement in the flow. The equations describing the evolution of instabilities are the unsteady Navier-Stokes equations. The nonlinear terms can be neglected, because perturbations have small amplitude compared to the mean flow. Thus for the study of these instabilities linearized Navier-Stokes unsteady equations are

constituted (sometimes called linear growth although the growth is exponential, or the term modal growth by reference to the eigenmodes of the linearized problem). In this context, the study focuses on stability of each mode separately, and it is considered that the boundary layer is unstable if one of these modes is unstable. When the instabilities have reached a certain amplitude, the nonlinear terms are no more negligible: the different modes can interact and eventually lead to turbulence.

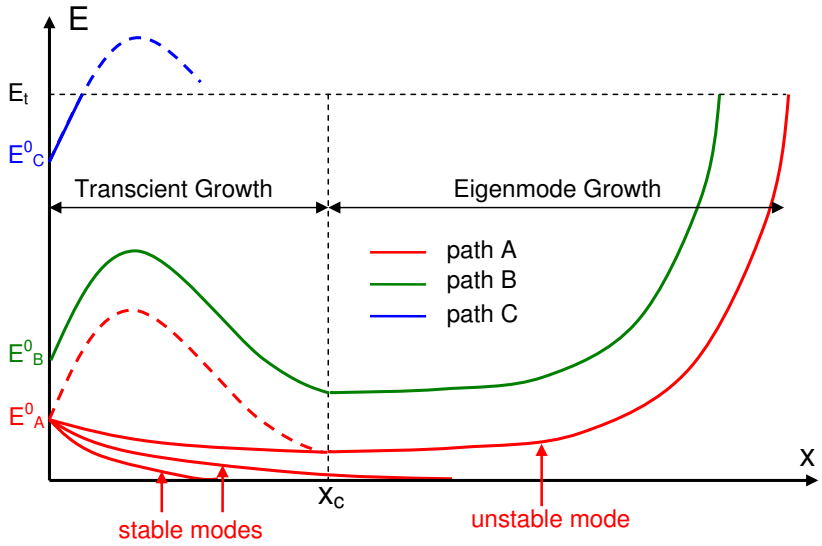

Figure 1.46: Illustration, which helps from energy consideration to explain different path to transition.

Path B and C. Transient growth is the algebraic initial amplification of perturbations due to the non-normality of the linearized Navier-Stokes operator. At high level of disturbances, the mechanism of transient growth can be expected to play a role in the transition. It may either be followed by an exponential decay and then by a modal amplification (path B), or directly trigger transition (path C). Roughness-induced transition is relevant to path C.

In this study path A is considered for natural transition, for which LST applies. Transition probably follows path B in conventional wind tunnel.

1.2.3 Stability theory and the e^N method

In hypersonic flows, normal modes are classified as Mack's first and second (or higher) modes, Cross-Flow (CF) instability, and entropy layer instability. In fact, it has been shown by Fedorov, Tumin and co-workers [35, 36, 37] that second mode instability is due to synchronization of the first and second mode, which consequently may be considered as a single mode : "...their frequency and phase speed coincide at some points" (ref.[35] p.361). Anyway, we will keep here the terminology 'first' and 'second' modes, which is well-ingrained and understood in the field. The first mode is a 3D mode whose direction of propagation is oblique with respect of the mean flow direction, whereas the second mode which appears around Mach 2 and becomes predominant at about Mach 5, is a 2D mode. Cross-flow modes are associated with the inflexional transverse (here spanwise) velocity component W (see figures 1.47 and 1.35). They are almost perpendicular to the mean flow direction, and may possibly have a zero phase speed (stationary waves, f =0 Hz). Nevertheless, their group velocity do not vanish, hence they are convectively unstable.

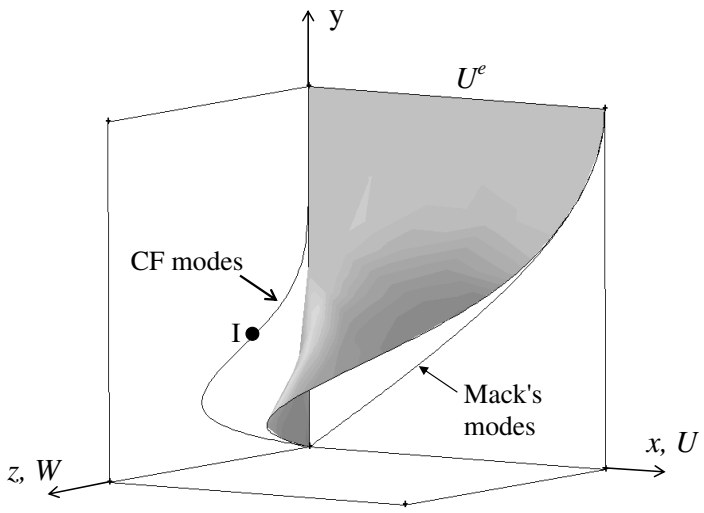

Figure 1.47: Sketch of a 3D mean flow and associated unstable modes.

First, a coordinate system attached to the wall (and not to the streamlines at the outer edge of the BL) is defined. Since the wall is plane, this coordinate system is the same for the whole surface : x is lying along the wall in the $\{X, Z\}$ plane, y is the distance to the wall and $z = -Y$ is the transverse direction. Corresponding units vectors are $\boldsymbol{x}$, $\boldsymbol{y}$ and $\boldsymbol{z}$ (figure 1.1).

In the 3D compressible Navier-Stokes equations, the mean-flow variables $\{\rho, U, V, W, P, T\}$ are perturbed by normal modes of the form

$$q'(x, y, z, t) = \hat{q}(y) exp[i(\alpha x + \beta z - \omega t)] \tag{1.5}$$

The parameters α, β and ω can either be real or complex, according to the nature of instabilities. Here, instabilities are convective, so the spatial approach is adopted : wavenumbers $\alpha = \alpha_r + i\alpha_i$ and $\beta = \beta_r + i\beta_i$ are complex, and the pulsation $\omega = 2\pi f$ is real. Hence, perturbations become:

$$q'(x, y, z, t) = \hat{q}(y) exp(-\alpha_i x - \beta_i z) exp[i(\alpha_r x + \beta_r z - \omega t)] \tag{1.6}$$

Fluid properties $\{C_p, C_v, \mu, k\}$ are also perturbed as, for example

$$C'_p = (dC_p/dT)T'$$

The stability solver developed at ICARE uses the fully variable thermodynamic and transport models previously described in subsection 1.1.2.

A 3D perturbation of given frequency f is characterized by the wave vector $\boldsymbol{k} = \alpha_r \, \boldsymbol{x} + \beta_r \, \boldsymbol{z}$ and propagates in the direction

$$\psi = \tan^{-1}\left(\frac{\beta_r}{\alpha_r}\right) \tag{1.7}$$

with the phase velocity

$$V_\varphi = \frac{\omega}{|\boldsymbol{k}|} = \frac{\omega}{\sqrt{\alpha_r^2 + \beta_r^2}} \tag{1.8}$$

Its amplitude

$$A(x, z) = |\hat{q}(y)| \, exp(-\alpha_i x - \beta_i z) \tag{1.9}$$

is growing (or decreasing) with the rates

$$\frac{1}{A}\frac{\partial A}{\partial x} = -\alpha_i \quad \text{in the } x \text{ direction} \tag{1.10}$$

$$\frac{1}{A}\frac{\partial A}{\partial z} = -\beta_i \quad \text{in the } z \text{ direction} \tag{1.11}$$

which define an amplification vector $\boldsymbol{\sigma} = -\alpha_i \boldsymbol{x} - \beta_i \boldsymbol{z}$. Perturbed equations are linearized (quadratic perturbation terms are neglected) and the mean flow is assumed parallel: $V = 0$. This is the local LST framework. The resulting set of differential equations for the amplitude of perturbations (normal mode equations for the eigenfunctions of the fluctuations) is given by Mack [27]. These equations are integrated from the outer edge of the BL - where mean-flow gradients are negligible- down to the wall, using a 4^{th} order Runge-Kutta scheme and a Gram-Schmidt orthonormalization procedure. From known vanishing boundary conditions in the freestream, the eigenvalues $\{\alpha, \beta, \omega\}$ of the problem are to be found using a shooting/Newton-Raphson procedure in order to satisfy the wall boundary condition $\hat{v}(y = 0) = 0$. The other wall boundary conditions are imposed : $\hat{u}(0) = \hat{w}(0) = \hat{T}(0) = 0$, and the pressure fluctuation may be chosen arbitrarily : $\hat{p}(0) = 1$. At convergence, the eigenvalues are related through the (numerically obtained) dispersion relation :

$$\mathcal{D}(\alpha, \beta, \omega) = 0 \tag{1.12}$$

It is assumed in the calculations that unstable waves are amplified in the direction of the group velocity. This gives the closure relation for the dispersion relation in the spatial theory [31]:

$$\bar{\psi} = \tan^{-1}\left(\frac{\beta_i}{\alpha_i}\right) = \theta_g \tag{1.13}$$

In the e^N method, amplification rates of every unstable frequencies are integrated along a path to be defined on the surface of interest (here the forebody of the vehicle). In compressible or 3D flows, one possibility is to seeks at each location, for a given frequency, the angle ψ_M for which the wave is mostly amplified : this is the so-called envelope method. Therefore, from equation (1.9), N factors are given by:

$$N(s, f) = \ln(A/A_0) = \max_{\psi} \int_{s_0}^{s} \sqrt{\alpha_i^2 + \beta_i^2}\, d\xi \tag{1.14}$$

where s_0 is the point on the path, where the wave, of amplitude A_0 at this location, becomes unstable. The transition location is then determined using the upper bound curve of all unstables frequencies. To be coherent with the choice of the local amplification direction 1.13, the integration path must be tangent to the group velocity in the computation of N factors. The code based on linear stability theory was developed and the linear stability analysis at flight conditions to the present forebody has been applied by Marc Ferrier.

1.2.4 Stability analysis results for flight conditions

Before presenting the stability results for flight conditions, we address the question of the grid resolution and its influence on the stability results (see section 1.1.4). The stability analysis has been performed for flight conditions at $M_\infty = 6$ and AoA=4° for mesh #4, #6 and #7. Figures 1.49, 1.48 and 1.50 show stability properties computed along a sample mesh line. The number of grid points across the boundary layer vary along this line from about 50 to 70 for mesh #4, 70 to 120 for mesh #6 and 130 to 150 for mesh #7. We can observe very small differences in the stability results for the different meshes, and conclude that mesh #4 can be used in all hereafter stability calculations for flight and experimental conditions.

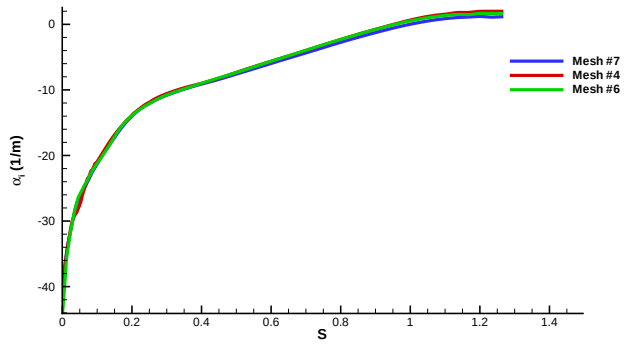

Figure 1.48: Stability results along mesh line 49. Amplification rate for frequency f=15 kHz.

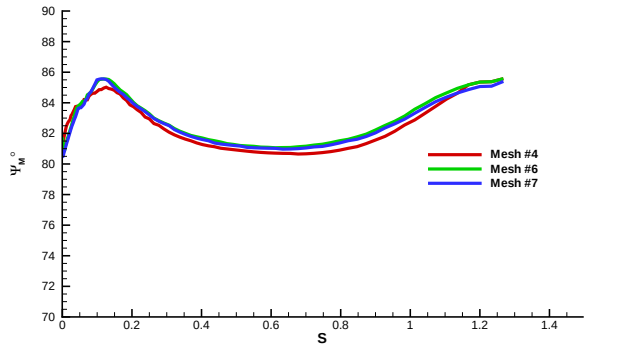

Figure 1.49: Same as figure 1.48: angle of propagation of most unstable waves.

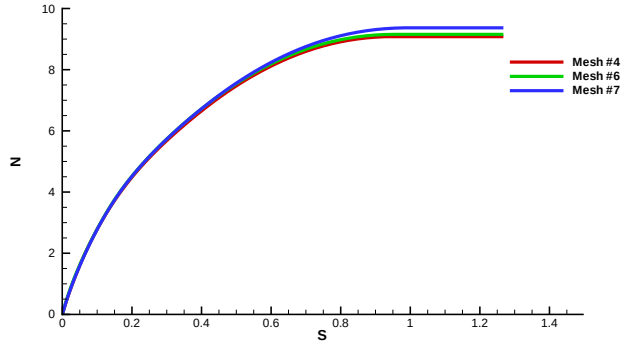

Figure 1.50: Same as figure 1.48: N factor.

Effect of the angle of attack at $M_\infty = 6$

The area of interest lies in the windward side of the forebody. Increasing the angle of attack makes the boundary layer thinner and more stable. This is visible on figures 1.51, 1.53 and 1.55 in which the unstable region ($\alpha_i < 0$) is reduced as the angle of attack is increased. White areas on figures are stable regions. Together with α_i, Ψ_M (the propagation angle of the most unstable waves) is given on the lower part of the figures. Ψ_M angles are always greater than 80°, which is typical of crossflow instability.

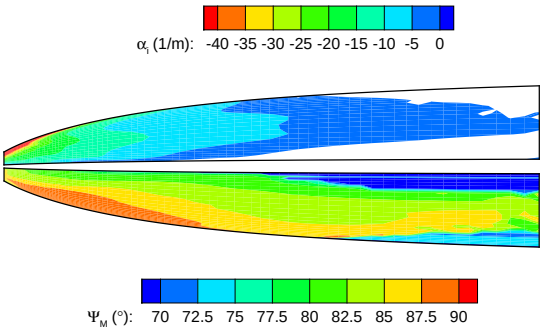

Figure 1.51: Stability properties at $M_\infty = 6$, AoA=2°.

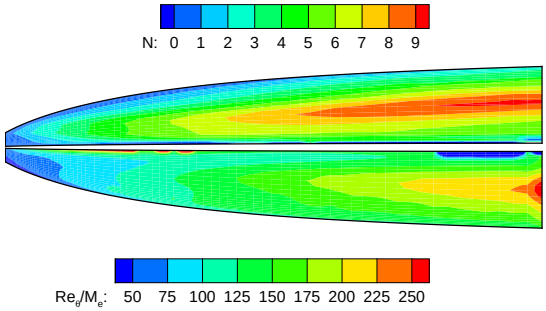

Figure 1.52: N factors compared to Re_θ/M_e at $M_\infty = 6$, AoA=2°.

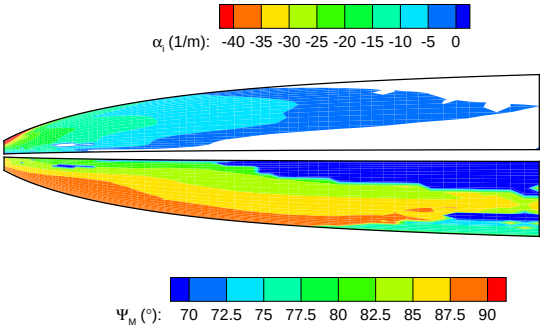

Figure 1.53: Same as figure 1.51: AoA=4°.

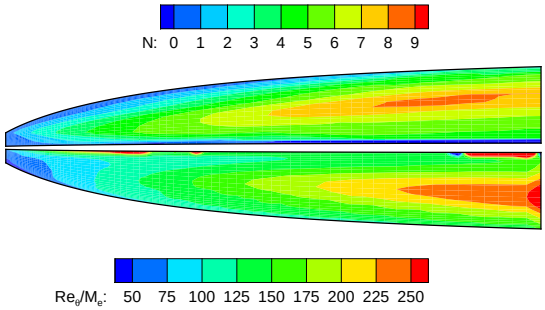

Figure 1.54: Same as figure 1.52: AoA=4°.

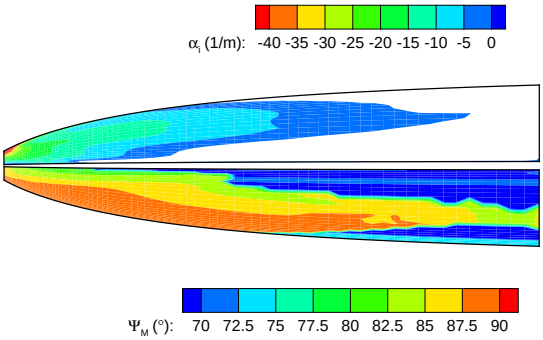

Figure 1.55: Same as figure 1.51: AoA=6°.

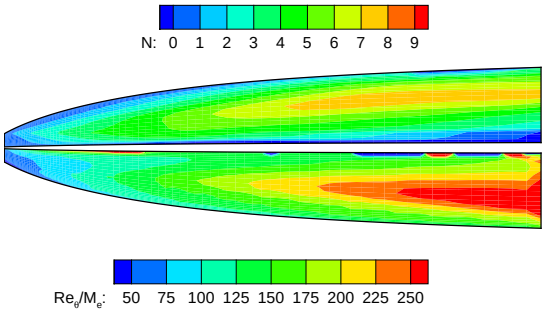

Figure 1.56: Same as figure 1.52: AoA=6°.

The resulting N-factors are consequently higher at small angle of attack. They reach

maximum values of 9.1 at AoA=2°, 8.4 at AoA=4° and 7.9 at AoA=6° (figures 1.52, 1.54, 1.56), all being hardly high enough for a definite conclusion about a natural transition in flight. NASP criterion Re_θ/M^e is plotted on the other side of the forebody. Some contradictions are observed between NASP criterion and N-factors. This is discussed in Marc Ferrier thesis [12].

Effect of the Mach number at AoA=4°

At $M_\infty = 4$, the structure of the flow is slightly different than at $M_\infty = 6$ or $M_\infty = 8$ (see subsection 1.1.5 effect of Mach number) and it has been found that instability is mainly due to oblique 1^{st} modes (figure 1.57). Crossflow instability is also found very near the nose leading edge, but is of minor importance here. At $M_\infty = 4$, amplification rates α_i are relatively high and give N-factors (figure 1.58) of the same order of magnitude as the M =6 case. On the other hand, at $M_\infty = 8$, the whole forebody is dominated by crossflow instability (figure 1.59). The maximum value is 4.8, too low for a transition in flight (figure 1.60). A Mack's 2^{nd} mode has also been found, too weak again for a natural transition. To be able to provoke transition in flight, roughness-induced transition have been studied and chapters 3 and 5 are devoted to these investigations.

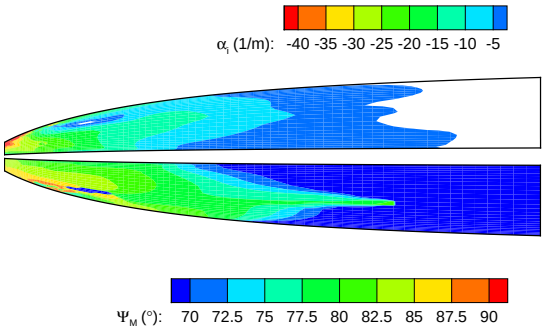

Figure 1.57: Stability properties at $M_\infty = 4$, AoA=4°.

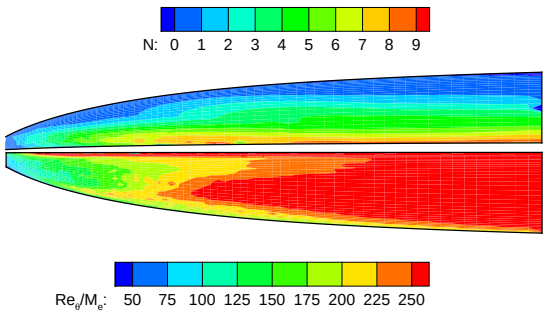

Figure 1.58: N factors compared to Re_θ/M_e at $M_\infty = 4$, AoA=4°

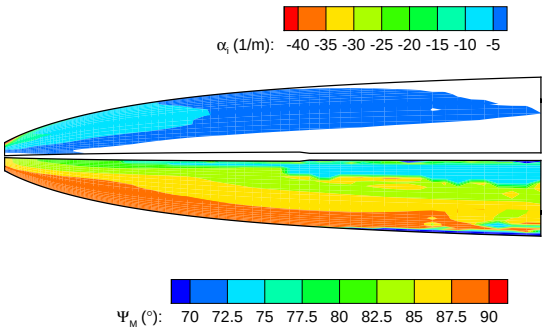

Figure 1.59: Stability properties at $M_\infty = 8$, AoA=4°.

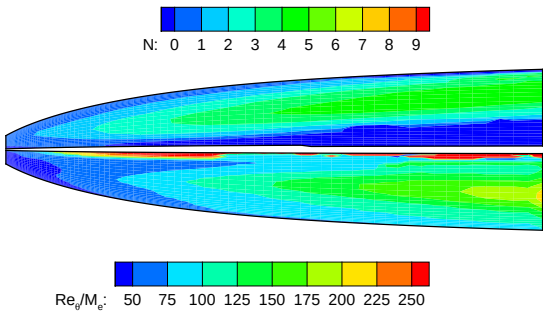

Figure 1.60: N factors compared to Re_θ/M_e at $M_\infty = 8$, AoA=4°

These results (figure 1.51 to 1.60) have been taken from Marc Ferrier's thesis [12].

Chapter 2

Test facilities and experimental methods for the detection of transition

Synopsis

Ce chapitre passe en revue différentes méthodes expérimentales de détection de la transition en régime hypersonique, et donne une rapide description comparée des souffleries hypersoniques de l'ITAM et des paramètres de l'écoulements dans chacune d'elles.

On peut distinguer : (i) les méthodes de mesure des fluctuations turbulentes de vitesse par anémométrie à fil chaud, permettant une analyse spectrale détaillée de la zone de transition puis de la turbulence développée (ii) les méthodes de mesure des fluctuations de pression pariétale ou de flux de chaleur, permettant seulement de détecter la zone de transition ; les sondes instationnaires utilisées sont assez coûteuses et difficile à mettre en oeuvre (iii) les méthodes de mesure de contrainte pariétale ; l'emploi des jauges de contraintes pariétales est délicat dans les souffleries à rafale (iv) les méthodes de mesure du flux de chaleur, déduites de la mesure de température pariétale par thermocouples ou par procédés optiques associés à l'usage de peintures thermosensibles (TSP) ; ces méthodes sont bien adaptées aux souffleries à rafale (iv) les méthodes de mesure de pression Pitot, particulièrement bien adaptées aux souffleries en régime continu.

L'avantage de la soufflerie à rafale AT-303 est de reproduire des conditions d'arrêt proches du cas vol, mais au détriment d'une durée de rafale très courte ($<$ 100ms). Inversement, la soufflerie continue T-313 permet des tirs de plus 5mn, mais la température et la pression statique sont très basses.

Les simulations numériques des écoulements sur l'avant-corps à échelle 1/3 dans ces souffleries, en régime turbulent et en régime laminaire, permettent d'obtenir les ordres de grandeur des différences de température pariétale, de pression Pitot, d'épaisseur de couche limite etc. auxquelles s'attendre dans chaque cas. Les calculs en régime turbulent sont réalisés avec le modèle k-ω-SST disponible dans Fluent®. Afin d'éviter certaines aberrations comme la production excessive d'énergie cinétique turbulente au passage du choc, le modèle est désactivé dans la région du nez.

Les calculs en régime turbulent ne sont pas absolument fiables, mais on en déduit au moins qualitativement que la variation de flux de chaleur pariétal est le meilleur indicateur de la transition dans AT-303, et que la variation de pression Pitot est plus significative dans T-313. Ce seront donc les techniques expérimentales retenues par la suite. This chapter con-

tains a review of experimental methods for the detection of transition and their comparison, and a description of hypersonic wind tunnels. Numerical simulations of wind tunnel tests and computations needed to design experimental setup are provided.

2.1 Basic experimental methods to detect the position of transition

Turbulence is a chaotic motion of the flow around mean values, and hence the appearance of fluctuations in the flow is the first indicator that the flow has become turbulent. As a consequence of turbulence, global or average characteristics of the flow are dramatically changed. Hence, the detection of the position of the laminar-turbulent transition is mainly based on the measurements of two kinds of changes in the BL:

- pulsating characteristics of the flow due to turbulent fluctuations;
- global wall characteristics like temperature, heat fluxes, skin friction.
- Pitot probe measurements at constant altitude

(i) *Detailed turbulence analysis*
The fundamental study of turbulence, like how perturbations enter the BL (problem of receptivity), how they are amplified (mechanisms responsible for turbulence) and what are the characteristics of further developed turbulence (anisotropy, time and length scales ...), requires unsteady measurements and spectral analysis of the data. For that, high speed and high resolution measurement systems are needed. A classical technique to measure pulsations is the hot-wire anemometry. Hot-wire anemometers allow to do spectral measurements of the flow up to 1 MHz. Resolution of hot-wire anemometry is high enough, since the frequency of the 2nd acoustic mode - the highest frequency mode expected in hypersonic flow - is usually of order of a few hundreds of kHz.

(ii) *Just finding the transition location*
If we are only interested in detecting the position of transition, a spectral analysis of the flow is not mandatory. Usually, in hypersonic flows, a resolution of 20 kHz is enough to provide qualitative indications of transition. Pressure pulsations or heat flux pulsations gauges can be used for that. Figure 2.1 is taken from [38] and illustrates how laminar-turbulent transition has been detected by heat-transfer gauges. It shows a top view of the flow coming from top to bottom. Each frame reports the time sequence of the gauge at the corresponding location. The flow is first laminar upstream and level of fluctuations in the signal is low. Downstream, the flow becomes turbulent and the observed level of fluctuations grows. Examples of applications of these techniques can be discovered in the following articles [38, 39, 40, 41, 42]. However, pulsation gauges are more expensive than other gauges and more complicated in operation than conventional steady gauges.

(iii) *Methods based on skin-friction*
Laminar-turbulent transition leads in a significant increase of the local skin friction and heat flux. Skin friction measurements are difficult and expensive tasks, usually needing strain gauges. Such gauges are complicated, not so compact, and are of limited

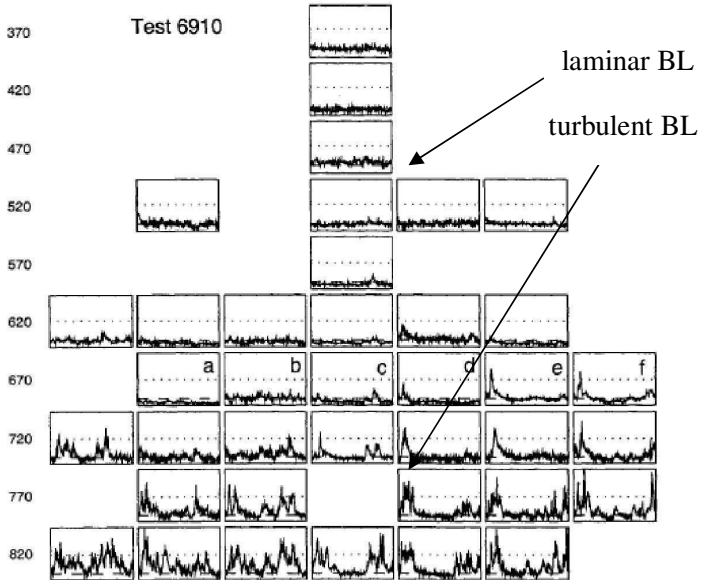

Figure 2.1: Signal from thin-film heat-transfer gauges [38]

range of application. Example of measurements using strain gauges can be found in [43]. Especially, it is difficult to detect the transition through skin friction in facilities with short operation time.

(iv) *Methods based on heat flux*

Heat flux measurements are not so complicated and a lot of different techniques exist for that. In experimental studies of heat transfer, both local (distributed measurement) and global (surface measurement) methods are used to measure heat fluxes. However, most are based on the temperature measurement, and some post-processing is needed to recover fluxes, reducing *de facto* the accuracy of the method. Anyway, temperature gauges are cheap and compact.

Discrete sensors of different kinds are used for local measurements. Thermocouples are widespread temperature gauges, however not so accurate. For example, calorimetric gauges give errors of about 10-20%. But, since heat flux is increased two or more times at the transition location, the accuracy of calorimetric gauges is enough to detect it [**?**]. Furthermore, in contrast to optical methods, discrete sensors can be applied in areas inaccessible to observation and optical detection. But the preparation of models for global methods is much simpler and cheaper than instrumentation for local measurements. Moreover, global methods are much more informative.

Various coatings which are sensitive to changes in surface temperature (melting materials, liquid crystals and fluorescent paints) are used for global measurements. The infrared radiation of the model also depends on the temperature of its surface and is defined by the Stefan-Boltzmann law. Examples of application of an IR camera to detect laminar-turbulent transition can be found in [39, 44]. The emissivity factor of a material like steel is small, and hence a metallic model has to be coated with some special paints in order to get valuable results. All of these techniques have relative advantages and drawbacks. It is significant to say that painting the wall increases its roughness and may modify heat exchanges due to a change in the surface thermal con-

ductibility. Also, during run tests, painting can be altered or destroyed by mechanical or thermal ablation. Some characteristics of optical techniques are compared in table 2.1.

Table 2.1: Comparison of characteristics of optical techniques.

	IR camera	fluorescent paints (TsAGI paints)	liquid-crystal or melting coatings
λ,nm	8000-9000	exit. 280-400 / fluor. 600-650	400-760
Temperature range(°C)	-20 $\sim$ 2000	10 $\sim$ 60	-30 $\sim$ 120
Sensitivity(%/°C)	$\sim$ 10	$\sim$ 3	$\sim$ 10
Spatial resolution (pixels)	by matrix 500x500	by camera (4098x4098)	by camera
Coating thickness (μm)		<10	>10
Limitation time	no, 50Hz by camera	relaxation time 2$\sim$5ms	relaxation time $\sim$ 0.3s
Additional equipments	special windows for IR		

Massive experimental data on heat transfer are accumulated using global measurements with melting indicators (see [45]). However, the possibility of melting indicators, as well as liquid-crystal coatings in impulse wind tunnels are strictly limited to the inertia of these coatings (large coating thickness - usually about 50 microns, absorption of heat needed for phase change in melting indicators). In addition, melting indicators have to be used with an imaging rate of several thousands frames per second, which complicates the experiment and processing of the data. In impulse wind tunnels, methods based on the fluorescent converters of temperature (TSP) are the most suitable [46]. TSP usually contain phosphor because the quantum emission of phosphor strongly depends on temperature. Compared to melting indicators for which a large number of frames is needed depending on the heat flux resolution, luminescent coating has the advantage that information can be obtained by a single (wind-on) image, which simplifies greatly the methodology. The intensity of coating luminescence depends not only on the temperature but also on several other factors: the intensity of the exciting light and its changes during time, the accommodation factor of the surface (hence, the shape and position of the model), the coating thickness and its phosphor concentration, etc. Some errors may be removed by the use of the reference image taken just before the experiment under the same conditions as wind-on image. Nevertheless, using the reference frame is not enough to obtain satisfactory accuracy. Successful results have been achieved through the use of binary (two color) TSP [46]. Binary TSP contains two phosphors: the active and the reference. The active luminophore is sensitive to temperature, and the reference luminophore does not practically react to changes in temperature: the luminescent intensity is only proportional to the excitation. Both phosphors are excited by a monochromatic radiation, but emit at different wavelengths. Two separated images have then to be recorded. If the intensity of the active and reference luminophores are recorded simultaneously, then the measurement result is not influenced by changes in the intensity of the exciting radiation, due for instance to an instability of the light source or to some deformation or movement of the model during the experiment. Using binary coating at NASA-Langley has allowed heat flux measurement in blow-down wind tunnels with accuracy close to that of discrete sensors [47]. This method is widely used in studies of aerodynamic heating of hypersonic aircrafts [48]. It is decided to collaborate with TsAGI scientists and to apply their luminescent paints in tests in ITAM.

(v) *Pitot tube measurements: blow down condition*

In conditions of a blow down wind tunnel, heat flux measurements do not apply (heat flux equal zero). It is possible to find the laminar-turbulent transition from wall temperature measurements or using a Pitot tube [49, 50]. A Pitot tube is a gauge which measures the flow velocity and is a classical device used to detect transition on 2D configurations. Measurements with a Pitot tube give the value of the stagnation pressure in incompressible flows. In a supersonic flow, the Pitot tube gives the stagnation pressure behind the normal shock attached to it and has to be corrected to provide the flow total pressure. The basic principle of determination of the transition with a Pitot tube is based on the change in shape of BL velocity profiles: a turbulent boundary layer is more "filled" than a laminar boundary layer. At a given fixed altitude, the maximum in Pitot pressure distribution is located in the transitional zone (see figure 2.2). Application of Pitot tube measurements in a hot shot wind tunnel is not reasonable because it is necessary to have enough time to move the gauge and scan the whole model length in order to find the position of transition.

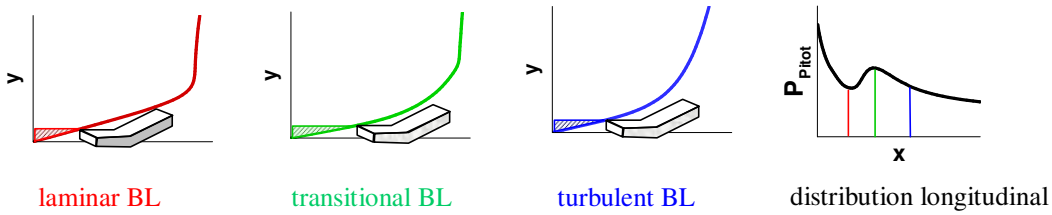

Figure 2.2: Principle of finding the laminar-turbulent transition using Pitot tube.

2.2 Description of wind tunnels and experimental conditions

Experiments have been done in wind tunnels of two types - the blow down T-313 and the impulse wind tunnel AT-303 with cooperation of ITAM of Siberian Academy of Science. Schemes of wind tunnels and parameters are described later in beginning of chapters 4 and 5. Some conditions in these wind tunnels are given in table 2.2. These wind tunnels require that the scale of the model should be 1:3.

Table 2.2: the blow down T-313 and the impulse AT-303 wind tunnels.

Wind tunnel	Size of operation section (m^2)	M_∞	P_{tot} (bar)	T_{tot} (K)	Regime time (sec)
T-313	0.6 x 0.6	2-7	2-10	up to 700	up to 600
AT-303	nozzle ∅ 0.4	6-20	up to 3000	up to 3000	up to 0.12

The main advantage of AT-303 is that it can reproduce experimental conditions close to flight conditions because of high stagnation temperature and pressure. But this is at the expense of a very short operation time, less than 100 ms. On the contrary, the blow down wind tunnel T-313 can operate for several minutes, but static temperature is very low. Unfortunately, these wind tunnels are conventional ones with high level of noise, which will have to be characterized by analyzing the free-stream fluctuations. Before the tests, simulations of the flow around the forebody with laminar and turbulent models have been carried out in test conditions. Parameters which we chose in computations gathered in table 2.3. The

obtained information is useful to choose and optimize the experimental techniques which are described above. Turbulent flow simulations have shown the k-ω SST model [51] to be

Table 2.3: Simulation of wind tunnels conditions: the blow down T-313, the impulse AT-303

Mach	P_{st} (Pa)	T_{st} (K)	P_{tot} (Bar)	T_{tot}, K	Re (1/m)
4	6484	67.3	9.8	282	47.0×10^6
6	490	48.0	7.7	400	9.2×10^6
6	3776	139.9	64.0	1094	13.6×10^6
8	1703	97.8	182.0	1268	13.8×10^6

more physically sound than other models available in FLUENT®, in simulating hypersonic boundary layers on a 3D body. However it was found that some unphysical production of turbulence occurred behind the shock due to strong gradients and big bluntness. To circumvent this problem, a laminar model is applied in the nose region and the turbulence model is used downstream. The transitional k-ω SST model implemented in FLUENT® also has been tested. Results obtained with this model are not very reliable. Anyway, using laminar and turbulent models to simulate the flow can help understanding how parameters can change during the transition and can improve experimental investigation techniques that would have failed otherwise.

Figure 2.3 shows an example of the skin friction in the case of a laminar or a turbulent boundary layers at $M_\infty = 6$ and AoA=4° in impulse wind tunnel AT-303. One can see that the skin friction is a good indicator (2- 3 times higher in a turbulent boundary layer), but as it is said before, its measurement is very difficult, and from a practical point of view, it is more interesting to compare heat fluxes and wall temperature distributions in laminar and turbulent boundary layers. During the very short duration of tests in the adiabatic wind tunnel (t<100 ms), the wall temperature has no enough time to change significantly. Therefore, the wall temperature in the calculations is fixed and imposed equal to 300 K. Figure 2.4 shows the level of heat fluxes in the laminar and turbulent boundary layers at $M_\infty = 6$. The level of heat flux in the turbulent boundary layer is two or three times higher than in the laminar case. Therefore utilizing thermocouples or optical techniques is preferable for the detection of laminar-turbulent transition.

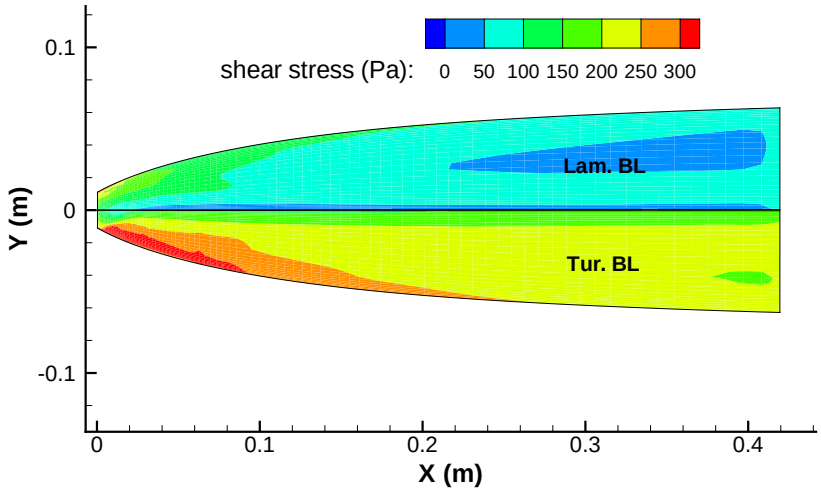

Figure 2.3: Wall shear-stress, $M_\infty = 6$, AoA=4°, impulse AT-303 WT.

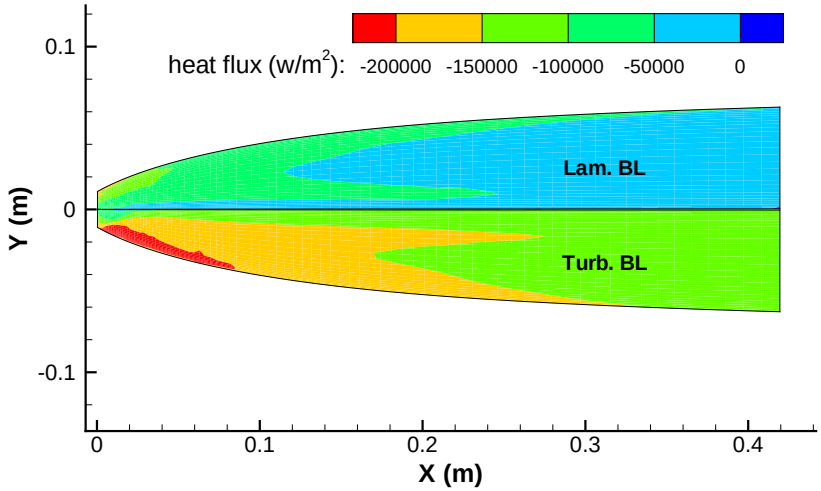

Figure 2.4: Heat flux, $M_\infty = 6$, AoA=4°, impulse AT-303 WT.

Wall temperature in the blow down wind tunnel conditions are presented on figure 2.5 (the wall is considered as adiabatic in FLUENT®). The wall temperature difference between a laminar and a turbulent flow is limited to a few degrees, because of the low stagnation temperature (400 K). As a consequence, it seems difficult to detect transition with temperature sensitive paints or thermocouple arrows. Using Pitot tubes would be more reliable.

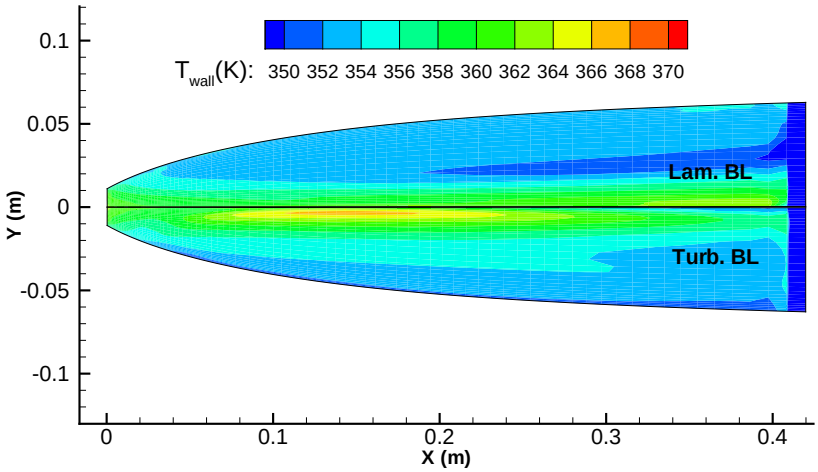

Figure 2.5: Wall temperature, $M_\infty = 6$, AoA=4°, blow down T-313 WT.

The main problem in using Pitot tubes to detect transition is that the gauge sensitivity is linked to its diameter, which should be small compared to the BL thickness. It is found from different experimental studies that the size of the tube should be less than half the boundary layer thickness [49, 50]. The definition of the edge of the boundary layer is not obvious and is subject to discussion[24]. The method applied here is based on the total enthalpy profile because it is not influenced by the entropy layer due to the curvature of the shock. Starting from the wall, the edge of the BL is found along a normal when the total enthalpy variation is less than 0.01% between two succesive mesh points. This method differs slightly from the one proposed by Kimmel *et al.*[22]. Figure 2.6 shows the boundary layer thickness at $M_\infty = 4$ and $M_\infty = 6$ and AoA=4° in the blow down wind tunnel conditions. On can see that the boundary layer thickness increases globally in the downstream direction, but in a non-uniform way in the transverse direction. This illustrates the difficulty in choosing properly the Pitot gauges.

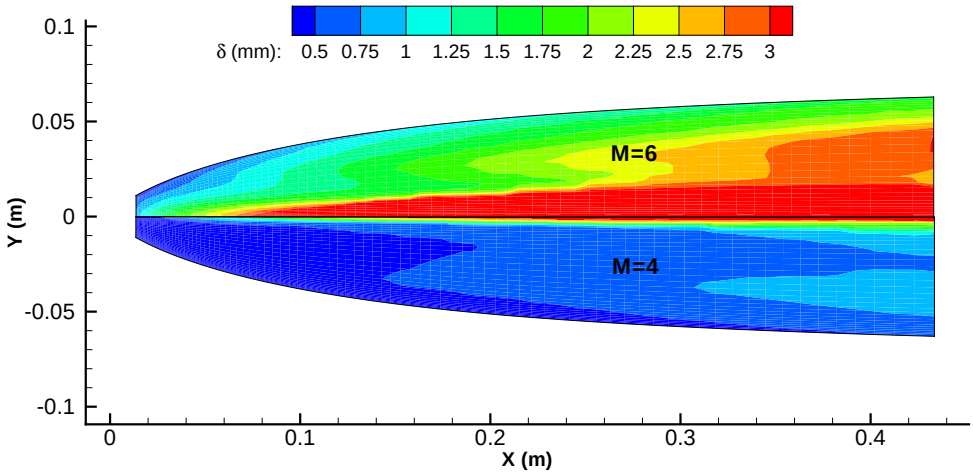

Figure 2.6: BL thickness at $M_\infty = 4$ and $M_\infty = 6$, AoA=4°, blow down T-313 WT.

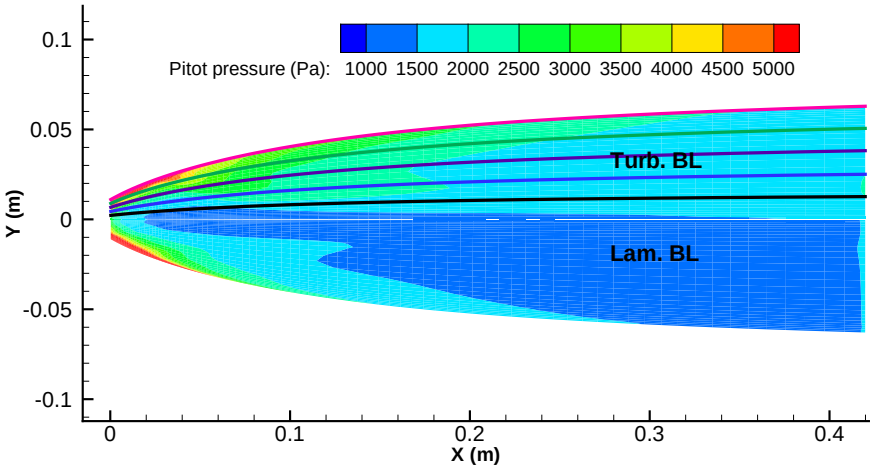

Figure 2.7: Pitot pressure map, color lines are mesh lines, $M_\infty = 6$, AoA=4°, blow down T-313 WT.

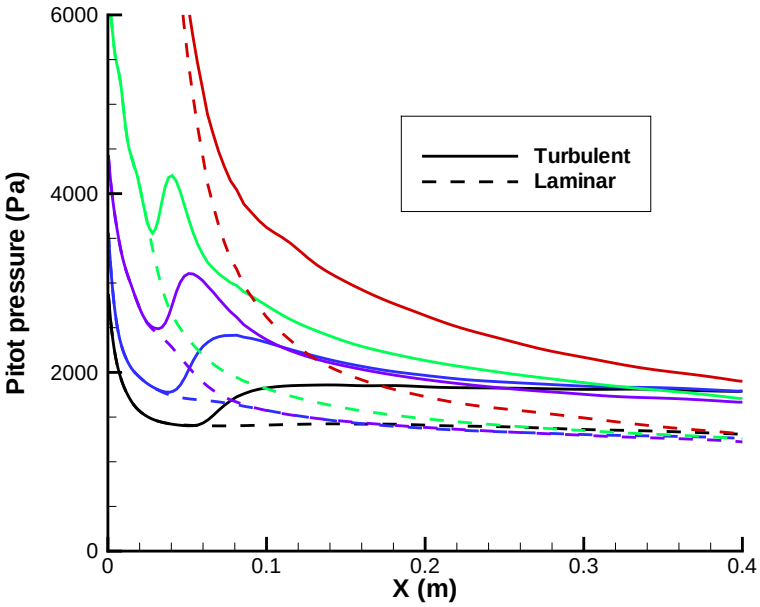

Figure 2.8: Pitot pressure along mesh lines, $M_\infty = 6$, AoA=4°, blow down T-313 WT.

Pitot pressure profiles have been computed from total pressure and real property of air. Then, these profiles have been integrated from the wall to various given heights simulating the orifice diameter, and hence the average pressure measure by the gauge. Figure 2.7 shows an example of a map of simulated Pitot pressure measurements, for height or tube diameter equal to 0.4mm. Distribution of Pitot pressure along mesh lines are given in figure 2.8.

Results of computations of laminar and turbulent boundary layers show that using temperature-based techniques for transition detection in the blow-down wind tunnel is questionable, and that a more reliable method should use Pitot tube measurements. Calculations show also that heat flux measurements should be a good indicator in the impulse wind tunnel AT-303. Comparison between computations and measurements will be discussed later in chapters 4 and 5.

Chapter 3

Roughness-induced transition: bibliography and empirical criteria

Synopsis

Les calculs ont montré que de la transition naturelle en vol est incertaine à M_∞=4 et à M_∞=6, et très improbable à M_∞=8. On a alors décidé d'étudier la possibilité de déclencher artificiellement la transition. On peut considérer des dispositifs actifs ou passifs. Les dispositifs actifs peuvent être l'aspiration/soufflage ou l'emploi de jets pariétaux, et peuvent servir à déclencher ou retarder la transition sur une large plage de paramètres de vol. Ils sont toujours chers et difficiles à mettre en oeuvre, et leur usage est peu développé en régime hypersonique. On leur préfère dans ce cas des dispositifs passifs comme l'emploi de rugosités réparties ou isolées.

L'efficacité des rugosités isolées doit être étudiée au cas par cas. On passe en revue divers critères empiriques (Potter & Whitfield, Van Driest & Blumer, Reda ...) permettant d'estimer l'efficacité d'une rugosité dans telle ou telle configuration d'écoulement, et on analyse les résultats publiés dans le cadre des programmes Hyper-X et HIFiRE en relation avec la configuration de notre étude. Certaines caractéristiques de la couche limite laminaire doivent être connues pour appliquer les critères. On les obtient par simulation numérique des conditions AT-303 à M_∞=6 et M_∞=8.

On propose enfin une forme (en losange), une hauteur (0.8mm) et une répartition optimale (espacement et position sur l'avant-corps) des rugosités pour un bon compromis d'efficacité dans les deux cas d'écoulement dans AT-303.

3.1 Introduction

At flight conditions, predicted N factors from LST at $M_\infty = 8$ reach a maximum 4.8 and are too weak for a natural transition. To be able to provoke transition in flight, roughness-induced transition has been studied in AT-303 conditions.
This means designing trips in terms of:

- shape
- size
- location

Bibliography about roughness-induced transition is given in this chapter to help design trips. A review of empirical transition criteria is done and some transition criteria are applied to

our forebody aimed to check effectiveness of trips.

Many investigations of the possibility to control the transition in hypersonic flows have been done during the last decades. Depending on the objective aimed, the control of transition may consist in triggering or delaying it. It is well known that suction or special porous covering can delay transition, while different types of roughness rather trigger transition. Control devices can influence the flow passively or actively. It is preferable to use active devices rather than passive ones because they can be adapted to necessary requirements in flight, whereas passive devices can not be effective at all regimes. The use of active devices is always associated with high cost and complicated manufacturing, installation and monitoring. Active devices in hypersonic flows have still not been widely applied and usually, simple roughness elements are used to provoke transition. The position of transition can change depending on the shape and size of trips, their position relative to the leading edge etc. Application of trips increases the drag of vehicle and may even change completely the topology of the flow. The choice of roughness must realize an optimum balance between their efficiency and their influence on the flow. From a theoretical point of view, devices of transition control may be considered as generators or amplifiers of disturbances. They can be studied and classified on that basis. Schneider [52] reviews the kind of instability which is produced by different types of roughness, and he gives some recommendations to choose adequately the trips. At the moment, there are no approaches being universally applicable to give good results for any configuration, and theory is not developed enough to allow modeling and designing of roughness for required conditions. Schneider's conclusion is [53]:

" There is as yet no scientific theory for estimating the effect of roughness on transition. Rather, the effects of roughness on transition must be evaluated using empirical wind-tunnel experiments under conditions that mimic flight as much as possible. [...] the results from several wind tunnels can then be correlated with one of several algebraic formulas. These remain useful, although none have general applicability."

In any case, experimental studies in ground test or in flight are the only reliable way to get valuable information about the efficiency of transition control devices. But investigations of different roughness elements and search for the best configuration are very costly. It is decided to use in our case already well-known configurations which are described in literature. Also different transition criteria which can help choosing the size of trips can be found in the literature and are reported here.

3.2 Empirical transition criteria and experiments : bibliography

3.2.1 Some selected criteria

Most empirical correlations for roughness-induced transition involve Reynolds number based on a height k of the roughness or characteristics of the boundary layer at the location x_k of the roughness. One distinguishes:

$$\mathrm{Re}_{kk} = \frac{\rho_k k U_k}{\mu_k} \quad ; \quad \mathrm{Re}_{ek} = \frac{\rho_e k U_e}{\mu_e} \quad ; \quad \mathrm{Re}_{x_k} = \frac{\rho_e x_k U_e}{\mu_e}$$

where the index k indicates values of flow taken at the height k, index e outside the boundary layer. Criteria are listed chronologically:

• *the Potter & Whitfield criterion* (1962) [54]

$$\boxed{\mathrm{Re}_{kk}\left(\frac{T_k}{T_w}\right)^{1.26} = A(\mathrm{M}_k)} \tag{3.1}$$

where $A(\mathrm{M}_k) = 1000\mathrm{M}_k$ if $\mathrm{M}_k < 3$ [55, 56]. For higher values of M_k (up to 10), the correlation $A(\mathrm{M}_k)$ can be found in Whitfield & Iannuzzi [57]

• *the Van Driest & Blumer criterion* (1968) [58]

$$\boxed{\mathrm{Re}_{ek} = K\left(1 + \frac{\gamma-1}{2}\mathrm{M}^2 - 0.81\frac{T_{aw}-T_w}{T_e}\right)\mathrm{Re}_{x_k}^{1/4}} \tag{3.2}$$

The constant K is 33.4 for a cone and 44.0 for a flat plate.

• *the PANT criterion* (1970s) with exponents modified by calculations based on the transient growth theory [59]

$$\boxed{\mathrm{Re}_\theta = 180\left(\frac{k}{\delta}\right)^{-1}\left(\frac{T_e}{2T_w}\right)^{-1.27}} \tag{3.3}$$

• *the Reda criterion* (1980s) [60]

$$\boxed{\mathrm{Re}_{kk} = C} \tag{3.4}$$

where C is a constant to be defined, in the range $200 \sim 450$ for ballistic re-entries cones.

• *the Shuttle criterion* (1990s) [61]

$$\boxed{\frac{\mathrm{Re}_\theta}{\mathrm{M}_e} = C\left(\frac{k}{\delta}\right)^{-1}} \tag{3.5}$$

Table 3.1: Shuttle (3.5) et Potter & Whitfield (3.1) criteria in EXPERT experiments.

	$\mathrm{Re}_u \times 10^{-6}$ (1/m)					
k (mm)	9	18	26	9	18	26
0.40	L	T	T	L	L	L
0.57	L	T	T	L	L	L
0.69	T	T	T	L	L	T
0.90	T	T	T	L	L	T
1.35	T	T	T	L	T	T
criterion	Shuttle			P & W		

All these criteria have been built from experimental data gathered on simple geometry like cones or flat plates, and of course may be questionable when applied to other more complex geometries. CFD calculations are needed to obtain the laminar flow parameters to apply all these criteria. The last listed three criteria are developed mostly for reentry vehicle and are less interesting for us. For example, experimental results and criterion predictions for the EXPERT vehicle [55, 56] are reported in table 3.1. Letters L or T correspond to the criterion prediction, and blue/red colors indicate a laminar-turbulent roughness wake in the experiments. Such comparison shows that the Potter & Whitfield criterion gives more accurate predictions than the Shuttle criterion ($C = 30$).

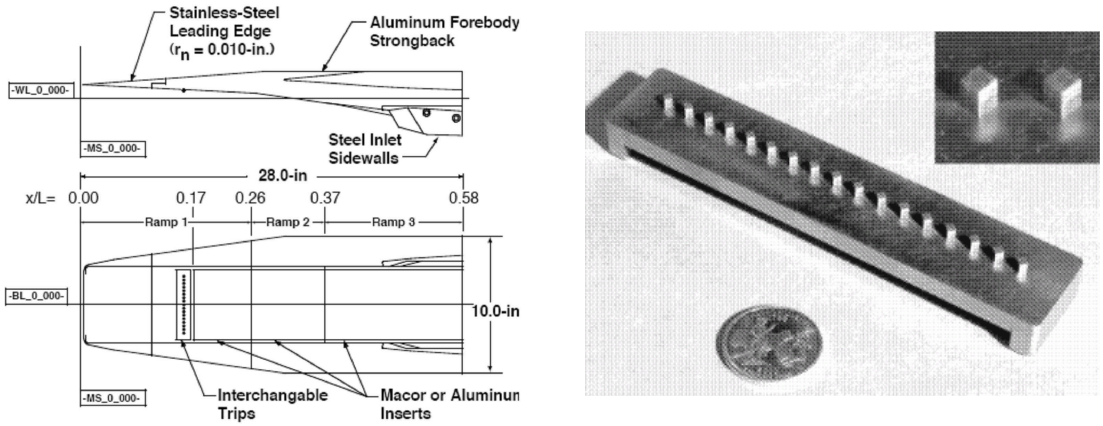

Figure 3.1: Hyper-X and example of roughness elements

3.2.2 The Hyper-X program

American NASA's Hyper-X 43A was successfully tested in March 2004 at M=6.8 and in November 2004 at M=9.6. The scramjet engine demonstrated a positive balance "thrust minus drag" during a 10 seconds flight. Careful and detailed experimental investigations have been conducted before the flight tests, including the study of laminar-turbulent transition and its control. Experiments for studying transition were carried out in different conventional wind tunnels at M =6 and 10, corresponding to flight tests. The transition was detected using specially designed luminescent thermal sensitive ceramic insertions. About 360 runs have been done to choose effective configurations [7, 62]. Description of these conventional wind tunnels and facility noise can be founded in [63, 64]. Figure 3.1 shows a photograph of diamond shaped trips and art view of the model. Also in NASA LaRC a study on the effect of different single or distributed roughness elements on the transition on a cone at M=5 is presented in [65] and reported on figure 3.2 and 3.3. Results show that a single isolated roughness with diamond shape is more efficient than other shapes tested. These results are highly influenced by the noise of the wind tunnel, except if the roughness is sufficiently high ("effective roughness") to immediately provoke the transition [66]. Tests on the forebody of X-51A showed, that in quiet conditions (the Boeing and U.S. Air Force office of Scientific Research Mach-6 Quiet Tunnel in Perdue University [67]) the diamond shape is the most effective [68].

New hypersonic vehicles equipped with air-breathing engines with adaptive (or regulated) inlets now emerge, and require the study and application of active control of transition. Nevertheless, such a task is made very difficult at hypersonic velocities due to high costs and technical constraints. Some interesting results about investigations on active control to transition also are presented in Berry's and Comp. review [69]. Different kind of jet nozzles were tested in this work. Shadowgraph pictures show the structure of the flow (figure 3.4) and indicate that air jets act like the installation of trips. Interesting results have been obtained, showing that an air injection is effective if total pressure of injections higher 40 times to static pressure in boundary layer.

3.2.3 The HIFiRE program

Some interesting results about transition in HIFiRE-1 (cone-cylinder-flare geometry) experiments have been reported in [70]. The objectives of the Americano-Australian program HIFiRE (Hypersonics International Flight Research Experimentation) are the investigation

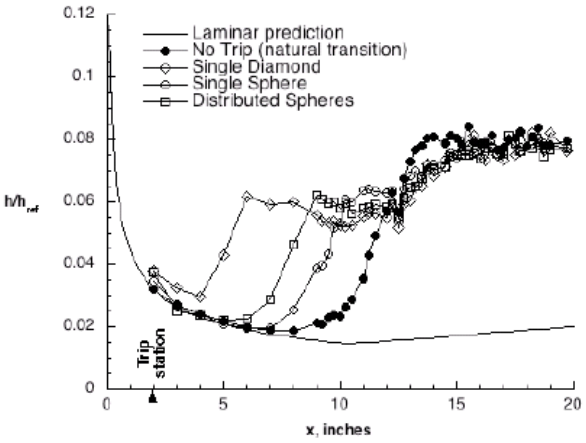

Figure 3.2: Comparison of different roughness, all with the same heights.

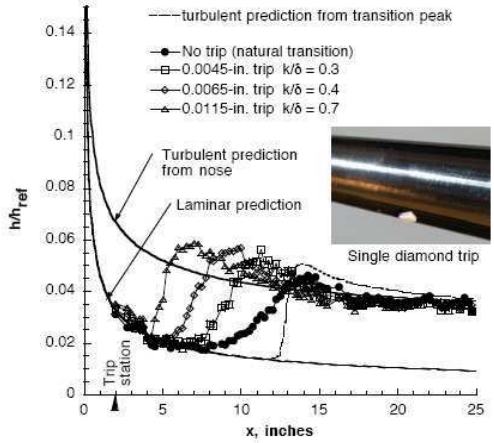

Figure 3.3: Influence of the height of roughness on transition [65].

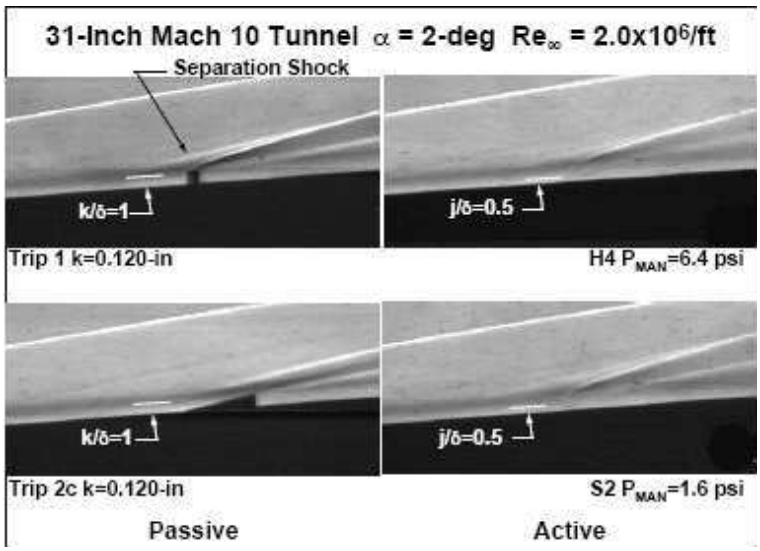

Figure 3.4: Comparison of the structure of the flow with passive and active trips.

of transition, separation, shock-boundary layer interaction in flight and to provide high-quality data for CFD validation and boundary-layer stability analysis [71]. A series of runs has been done in the NASA LaRC Mach 6 wind tunnel at Re_u 7 $\sim$ 19.5 $\times$ 10^6 1/m [71]. The geometry of the model is shown on figure 3.5. The conical section with 7° half-angle has a length of 0.2159 m with a nose bluntness of 1.19 mm. The cylindrical section has a length of 0.1003 m. Then cone with 33° half-angle has a length of 0.0124 m and final cylindrical section has length of 0.051 m. Total length of approximately is 0.381 m. Flow parameters and main results are reproduced in tables 3.2 and 3.3 extracted from [71]. An isolated diamond-shaped roughness is placed at x_k. Runs 36, 37 and 39 have been conducted on the HIFiRE model and runs 62 to 66 have been obtained on a simple blunt cone with 7° half-angle 0.381 m long. According to the results indicated in table 3.2 transition has not been observed in runs 39 and 63. Transition occurred just after the trip ("effective" trip) in runs 65 and 66. However, it was not clear for run 37 if transition occurred naturally or due to the trip, and there is some contradiction in the paper (tables 3 and 4 p.1132 in [71]).

Results indicate that trips are effective if $\mathrm{Re}_{kk} > 4500$ and $\mathrm{Re}_{x_k} > 10^6$ (table 3.3). In run 65 where transition clearly occurred due to the trip of height 0.3 mm, $k/\delta \approx 0.7$ (fig.9a p.1131 in [71]) and the edge Mach number $Me \approx 4.6$. This will help designing a roughness for the forebody in the AT-303 wind tunnel.

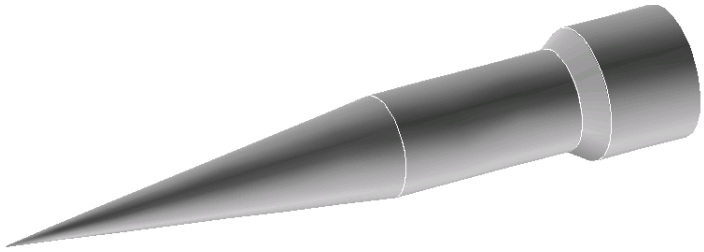

Figure 3.5: HIFiRE cone-cylinder-flare geometry.

Table 3.2: Trips and runs conditions for each tripped run, from [71].

Run	k (mm)	x_k/L	Transition ?	x_{tr}/L	AoA°	Orientation
36	0.165	0.1114	Yes	0.28	0	–
37	0.292	0.1114	Yes	0.23	0	–
39	0.1143	0.1114	No	–	0	–
62	0.292	0.18	Yes	0.27	0	–
63	0.292	0.18	No	0.37	-3	leeward
64	0.292	0.18	Yes	0.30	-5	leeward
65	0.292	0.18	Yes	0.25	3	windward
66	0.292	0.18	Yes	0.24	5	windward

Table 3.3: Roughness correlation quantities for each tripped run.

Run	Re_{kk}	$(\mathrm{M}_e)_k$	$\mathrm{Re}_{x_k} \times 10^{-6}$	$(\mathrm{Re}_{ek})_{tr} \times 10^{-3}$	$(\mathrm{Re}_\theta/\mathrm{M}_e)_{tr}$	k_{eff} ?
36	115	3.102	0.1678	1.027	77.854	No
37	500	3.142	0.1720	1.706	71.102	Yes (?)
39	53	3.140	0.1723	–	–	No
62	412	3.345	0.3461	1.740	75.451	No
63	58	3.525	0.3182	–	–	No
64	97	3.863	0.3568	2.187	547.300	No
65	4510	4.594	1.346	6.745	88.474	Yes
66	7455	4.633	1.710	7.643	85.790	Yes

3.3 Roughnesses design for the forebody in AT-303

There are 2 steps:

1. CFD calculations of the BL parameters in AT-303 conditions, and determination of the roughness height according to results of HIFiRE-1 experiments
2. application of empirical transition criteria for verification

3.3.1 Results of CFD computations in AT-303

Some calibration data of the AT-303 nozzles are given in table 3.4. Static parameters have been computed from the total parameters and the indicated Mach number. The laminar flow around the forebody at AoA=4° has been computed for the conditions gathered in table 3.4. Figures 3.6 and 3.7 show the boundary layer thickness and the edge Mach number.

Table 3.4: Flow parameters in AT-303.

M_∞	P_{tot} (bar)	T_{tot} (K)	P_{st} (Pa)	T_{st} (K)	Re_u (1/m)
5.7	47.5	1557	3500	226	6.18×10^6
7.8	104	1505	1085	124	6.05×10^6

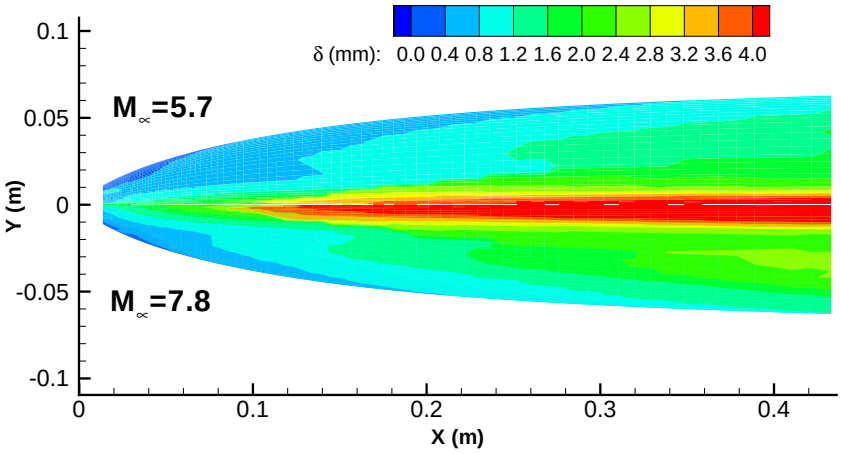

Figure 3.6: Laminar BL thickness at $M_\infty = 5.7$ et 7.8, AoA=4° in AT-303.

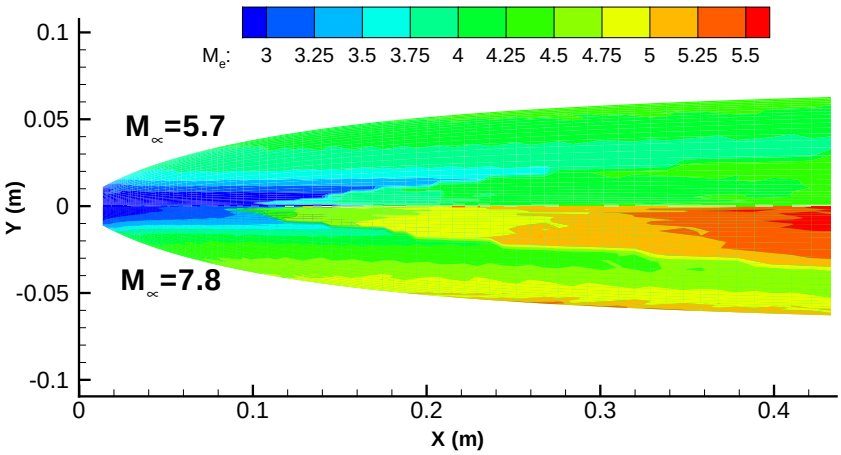

Figure 3.7: Idem figure 3.6: edge Mach number.

The average BL thickness in the area 0.1 m $< x <$ 0.2 m is 1 mm at $M_\infty = 5.7$ and 1.5 mm at $M_\infty = 7.8$. Corresponding edge Mach numbers are $3.8 < M_e < 4.0$ for $M_\infty = 5.7$ and $4.2 < M_e < 4.7$ for $M_\infty = 7.8$ respectively. If we keep the same ratio $k/\delta \approx 0.7$ than in the

HIFiRE-1 experiment ($M_e \approx 4.6$, table 3.3), an efficient roughness should be approximately

$$\boxed{k \approx 0.8mm}$$

Figure 3.8 confirms that k=0.8 mm is a good compromise for $M_\infty = 5.7$ et $M_\infty = 7.8$. In the next section, the previously listed criteria are applied to such a roughness in the AT-303 conditions.

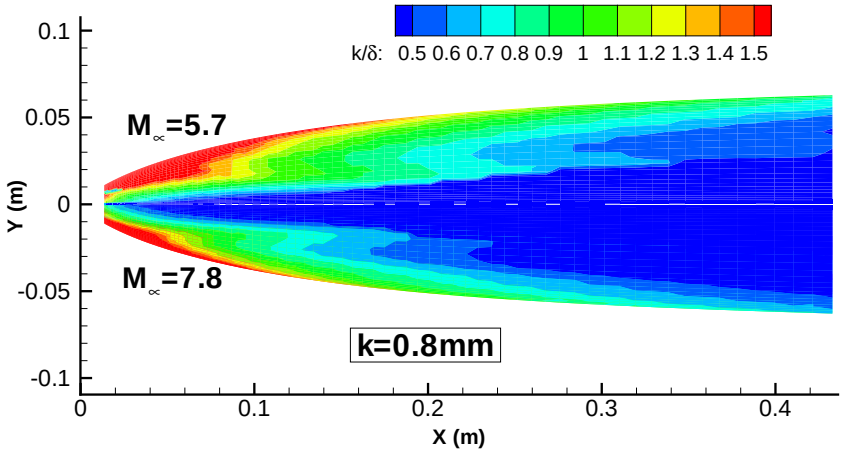

Figure 3.8: Verification that $k/\delta \approx 0.7$ at 0.1 m $< x <$ 0.2 m for $k \approx 0.8$ mm at $M_\infty = 5.7$ and 7.8, AoA 4°, in AT-303.

3.3.2 Application of transition criteria

• *Potter & Whitfield criterion*

To test this correlation, the ratio of the left-hand side to the right-hand side of (3.1) is computed and plotted on figure 3.9. The roughness is "effective" in the locations where the ratio is greater than 1. This occurs everywhere at $M_\infty = 5.7$, and very close to the nose leading edge at $M_\infty = 7.8$. Anyway, the correlation is uncertain where $M_k > 3$, and may not be accurate in the nose, as shown on Figure 3.10.

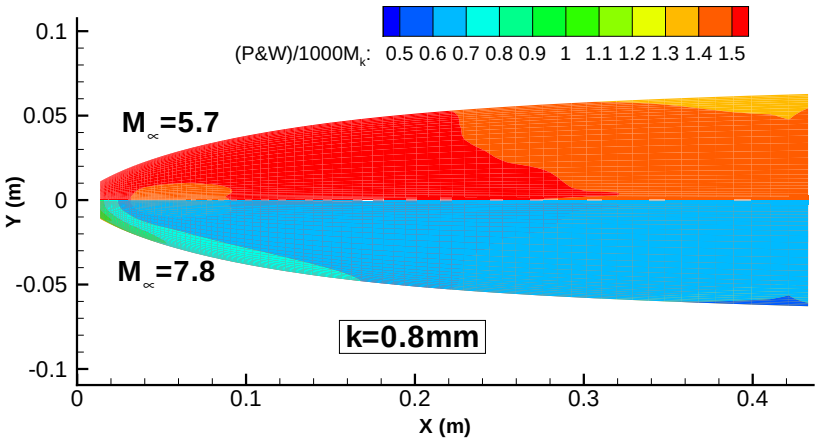

Figure 3.9: Potter & Whitfield criterion (3.1). The trip is efficient where the value is greater than 1.

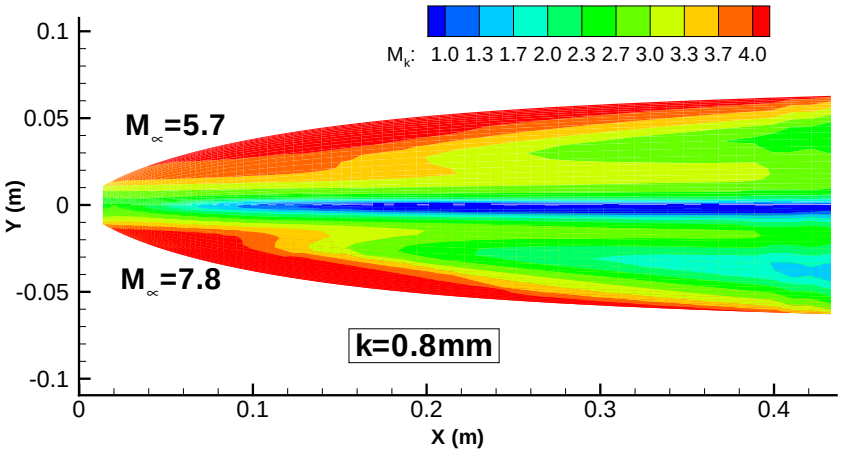

Figure 3.10: M_k at a trip height k.

• *Van Driest & Blumer criterion*
To apply the Van Driest-Blumer criterion, an efficient roughness height is computed out of eq. (3.2), where Re_{x_k} is replaced by $Re_x = \rho_e U_e X/\mu_e$. The model constant K is 44, as recommended for a flat plate [58]. Figure 3.11 shows the ratio k/k_{eff}. As for the P & W criterion, the locations where the ratio is greater than one indicate an effective k=0.8 mm trip. It is effective for at x < 0.2 m at $M_\infty = 7.8$ and everywhere at $M_\infty = 5.7$.

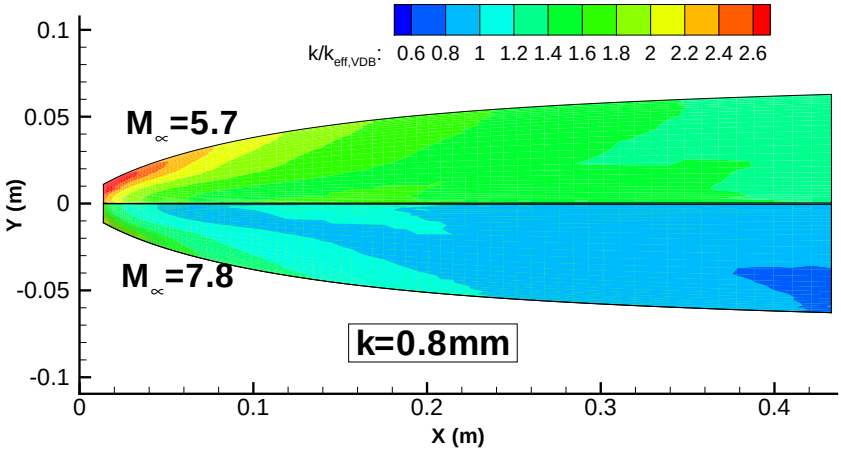

Figure 3.11: Van Driest & Blumer criterion (3.2). The trip is efficient where the value is greater than 1.

• *PANT criterion*

To apply the PANT criterion, the right-hand side of eq. (3.3) is computed and divided by Re_θ. Once again, values greater than 1 indicate an efficient location for the trip. Figure 3.12 shows that the trip can be placed anywhere, but with some uncertainty near the nose close to the symmetry plane.

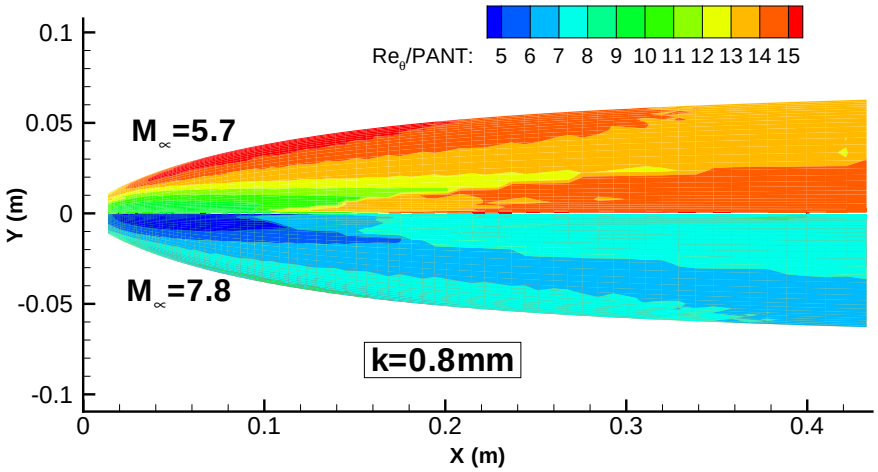

Figure 3.12: PANT criterion (3.3). The trip is efficient where the value is greater than 1.

- *Reda criterion and HIFiRE-1 experimental correlation*
  According to HIFiRE-1 experiments, we should check that:

  1. $\mathrm{Re}_{kk} > C$, relation (3.4) with $C \approx 4500$ (see table 3.3).
  2. $\mathrm{Re}_{x_k} > 10^6$.

Figures 3.13 shows the values of Re_{kk} in the location range 0.1 m $< x <$ 0.2 m. At $\mathrm{M}_\infty =$ 5.7 the condition satisfied and the roughness is "effective" except close to the symmetry plane. At $\mathrm{M}_\infty = 7.8$, Re_{kk} is too low. For completeness, figure 3.14 shows the values of Re_{ek}. In fact, Re_{kk} and Re_{ek} are close to each other. They are greater than 3000 everywhere and reach even higher values close to leading edge. Finally, figure 3.15 indicate that condition $\mathrm{Re}_{x_k} > 10^6$ is satisfied in the location range 0.1 m $< x <$ 0.2 m.

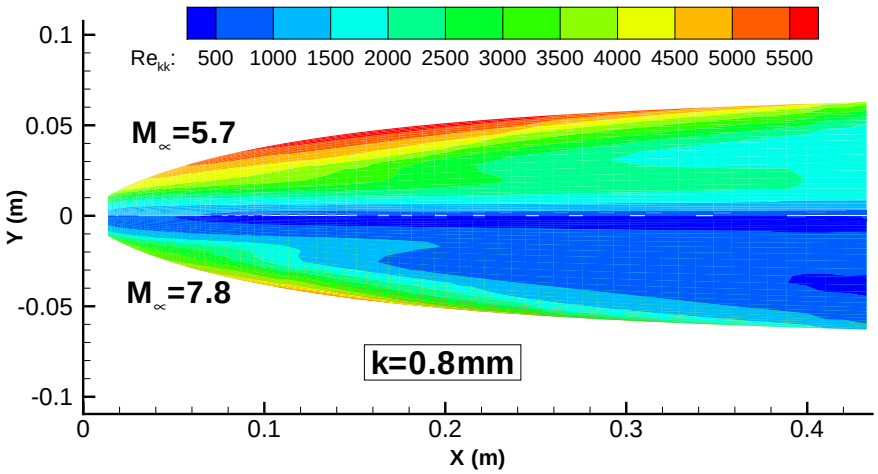

Figure 3.13: Reda criterion (3.4). The trip is efficient where $\mathrm{Re}_{kk} > 4500$.

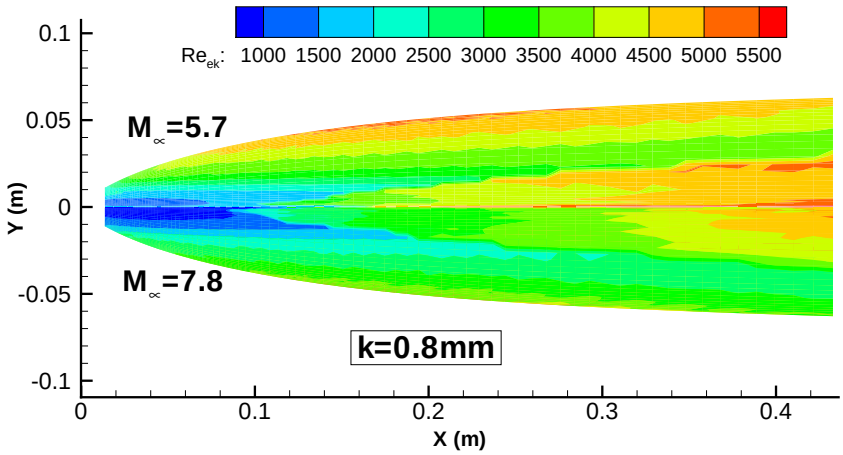

Figure 3.14: Re_{ek}, AT-303, $M_\infty = 5.7$ et 7.8, AoA=4°.

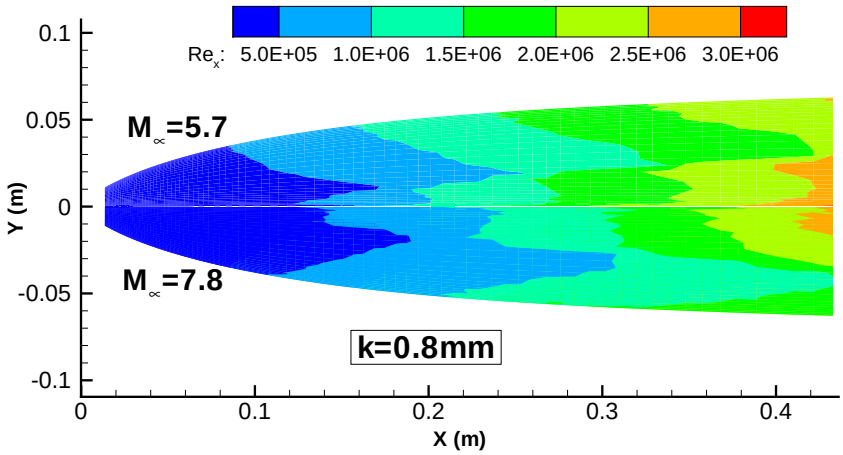

Figure 3.15: Re_x, AT-303, $M_\infty = 5.7$ et 7.8, AoA=4°. The trip is efficient where the value is greater 10^6.

3.4 Conclusion

In spite of some contradictions between the predictions of different criteria, some recommendations and proposals can be done:

- Diamond shaped trips are likely to be the most efficient
- A roughness height k=0.8 mm is a good compromise for $M_\infty = 5.7$ and $M_\infty = 7.8$
- Trips should be placed in region $x \approx 150$ mm

A scheme of installation of trips for experiments in AT-303 is shown in figure 3.16. The real installation is given in figure 5.13, for 2 position: $x \approx 150$ mm and $x \approx 200$ mm.

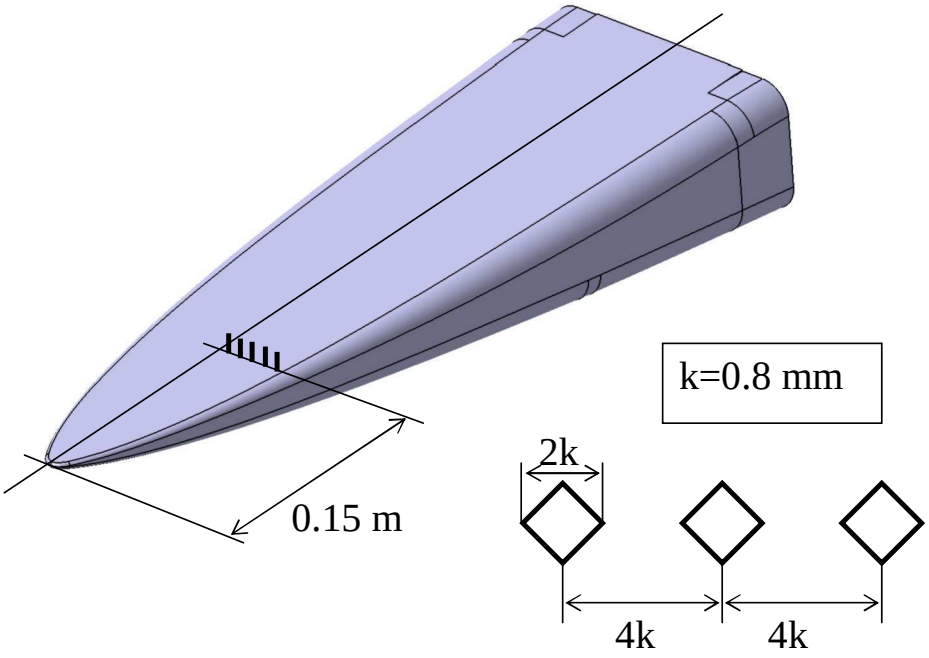

Figure 3.16: A scheme of installation of trips for experiments in AT-303.

It is important to notice that if roughness are “effective”, i.e. they trigger transition just downstream of their location, the level of noise has little influence on the phenomenon and they will be also “effective” in quiet or flight conditions ([66] p. 331).

Chapter 4

Experimental transition in wind tunnel T-313: experiments/computations

Synopsis

Ce chapitre décrit précisément les caractéristiques de la soufflerie continue T-313 et les procédés expérimentaux de mesure par sonde de Pitot. On donne les résultats d'étalonnage des tuyères pour M_∞=4 et M_∞=6, les caractéristiques des sondes de pression et les paramètres d'arrêt de l'écoulement. On montre quelques visualisation par procédé Schlieren de la structure du choc et de la couche limite. D'autres visualisations par film d'huile confirment la présence de l'écoulement "crossflow" mis en évidence numériquement.

Dans chacun des cas M_∞=4 et M_∞=6, on rapporte les résultats de mesure de la pression Pitot obtenue en faisant glisser les sondes d'amont en aval le long de la paroi. L'augmentation de la pression Pitot traduit le changement de forme du profil de vitesse dans la couche limite et donc l'apparition de la transition laminaire-turbulent. Celle-ci se situe très près du nez à M_∞=4, et plus en aval, vers le milieu de l'avant-corps à M_∞=6. On relève également les profils de pression Pitot dans la couche limite en déplaçant les sondes perpendiculairement à la paroi, à chaque extrémité des lignes de déplacement longitudinales.

Pour chaque répartition expérimentale de pression Pitot (longitudinale et normale), on effectue la comparaison avec les résultats de calculs CFD en régime laminaire et turbulent. Les calculs corroborent systématiquement les résultats expérimentaux, prouvant par là tout l'intérêt de la démarche.

On effectue enfin la comparaison entre la position de la transition expérimentale et celle prédite par l'analyse de stabilité couplée à la méthode du e^N. Les calculs de stabilité sont réalisés dans les conditions de l'expérience, mais la méthode (empirique) exige de connaître la valeur du facteur N de transition dans cette soufflerie particulière. Pour celà, on exploite les résultats expérimentaux de transition sur plaque plane obtenus par V. Kornilov de l'ITAM [43]. En superposant les positions de début et de fin de transition expérimentale sur les courbes enveloppe de facteur N calculées sur plaque plane dans les mêmes conditions, on obtient les corrélations $N_{tr,debut}$(M,Re) et $N_{tr,fin}$(M,Re) dans T-313. Les valeurs de fin de transition sont dans la plage $N \sim 3$ à 4, typique des souffleries conventionnelles.

Dans le cas M_∞=4, la prévision théorique de la transition correspond bien aux observations expérimentales car les mécanismes de transition sur l'avant-corps et sur la plaque

plane qui a servi pour la calibration sont les mêmes : 1^{er} mode oblique. Dans le cas M_∞=6, la présence d'instabilités "crossflow" au nez de l'avant-corps fausse les résultats. On doit pratiquer une intégration dite "discriminante" lors du calcul des facteurs N pour n'intégrer que les taux d'amplification des ondes de type 1^{er} mode oblique. On constate qu'éliminer l'amplification des ondes telles que $\psi_M > 80°$ donne de bons résultats par rapport à l'expérience. Cette valeur empirique doit être confirmée sur d'autres cas de figure, mais n'est néanmoins pas contradictoire avec la démarche même de la méthode du e^N, empirique par nature.

Ces travaux ont été soumis à *Journal of Spacecraft and Rockets* en novembre 2009.

4.1 Experimental setup and model

4.1.1 Description of the blow down wind tunnel T-313

The first part of the experiments has been done in the blow down wind tunnel T-313 of ITAM at M_∞=4 and 6. The blow down wind tunnel T-313 has a 0.6 x 0.6 m^2 test section and a Mach number range 2 to 7. Some pictures of this wind tunnel are given in figures 4.1 and 4.2. The principal scheme is shown in figure 4.3. Regime time of T-313 depends on conditions and are usually not less than several minutes. The total temperature for lower Mach number is the temperature of ambient air and the unit Reynolds can vary depending on total pressure in the prechamber. Above Mach number 5, the special heater used to avoid the condensation of air, and total temperature can reach 700 K.

Figure 4.1: Photograph of the blow down wind tunnel T-313.

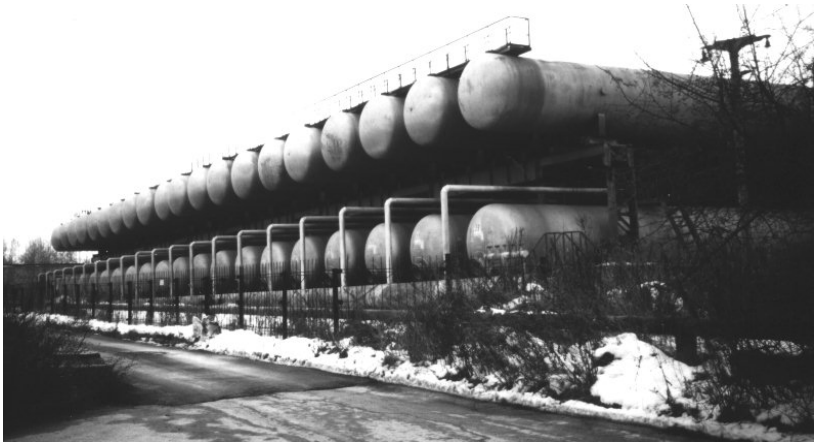

Figure 4.2: Air storage for T-313, up to 20 bar.

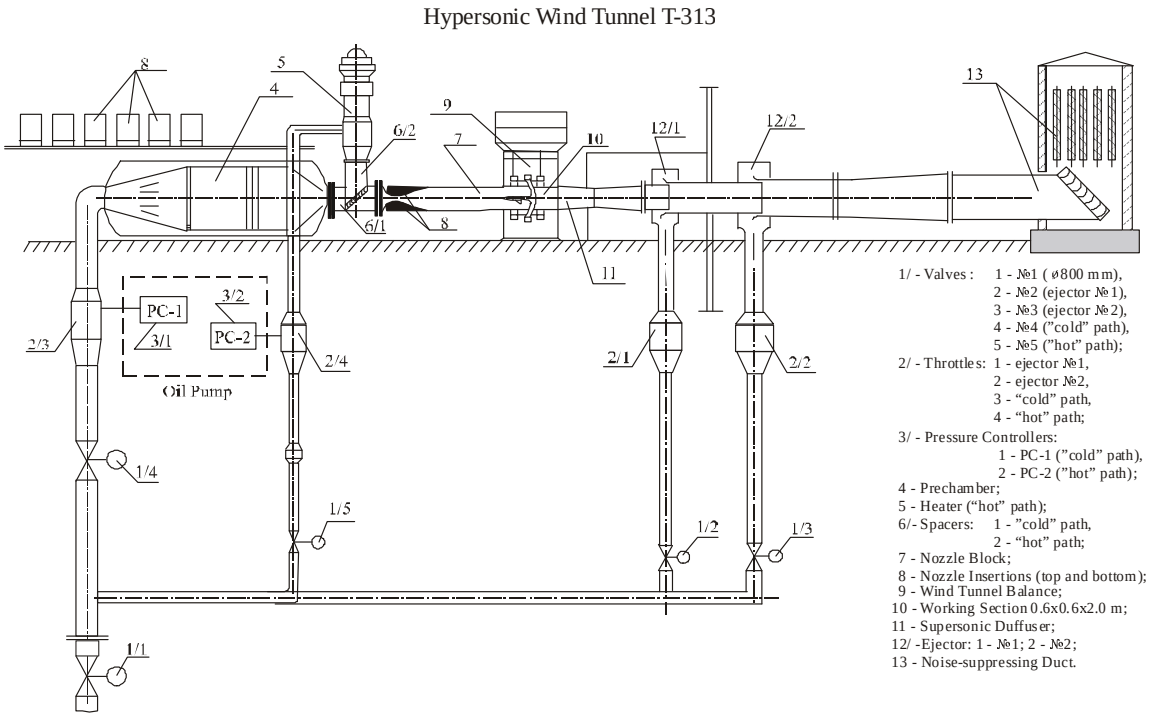

Figure 4.3: Principal scheme of T-313.

Calibrations of the nozzles $M_\infty = 4$ and $M_\infty = 6$ are shown in figures 4.4 and 4.5. Mach number fields are calculated by measurements with Pitot pressure rake. The non-uniformity of the flow is higher at Mach number 6, and is possibly due to the heater. Fluctuations of the flow in T-313 are still not well studied but this wind tunnel is considered as a conventional wind tunnel with high level of noise. Subsection 4.5.1 will discuss about stability analysis and N factors, and will show that N factor for this T-313 wind tunnel are about 3∼4 that is typical for conventional wind tunnel.

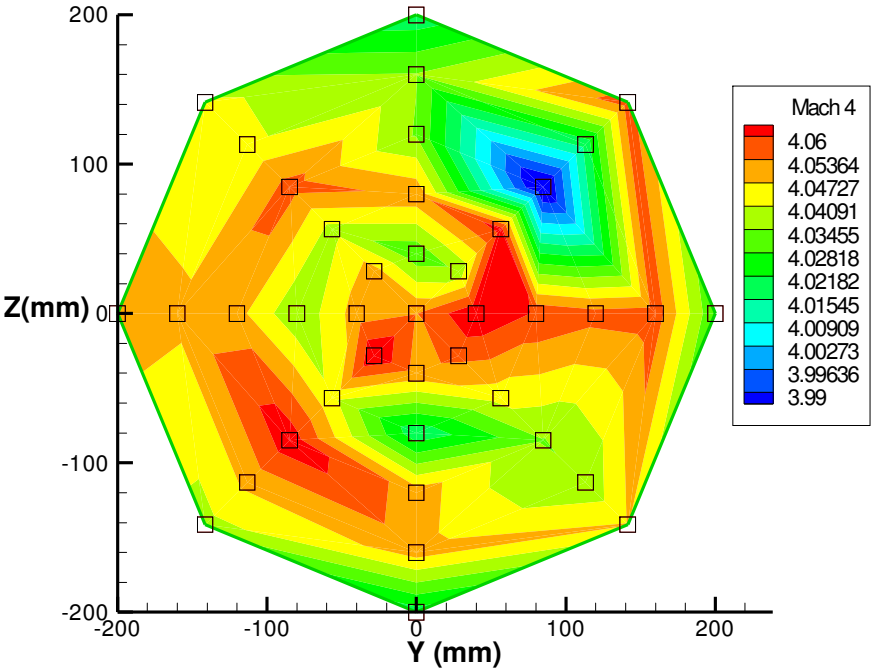

Figure 4.4: Mach number field for $M_\infty = 4$ in T-313.

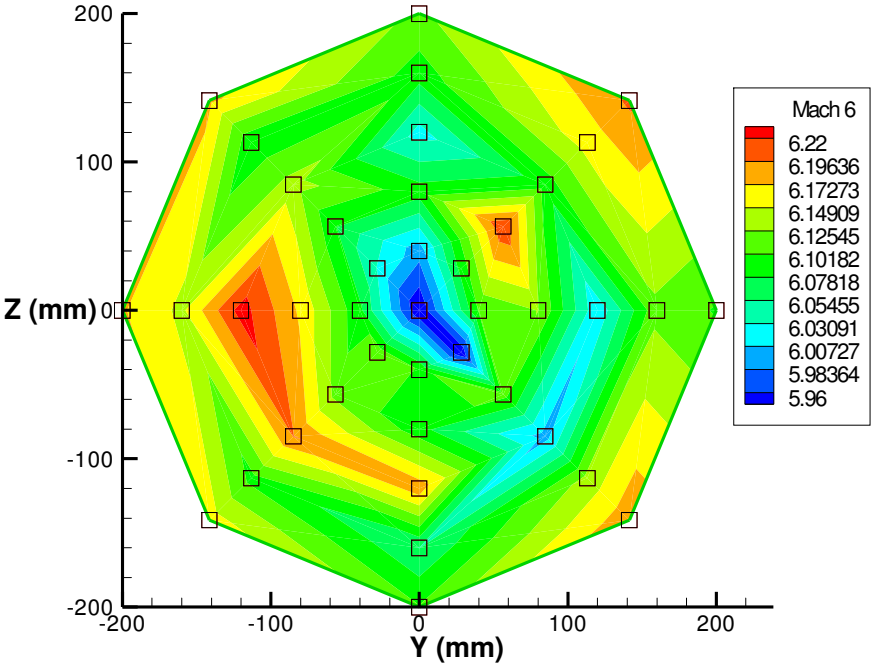

Figure 4.5: Mach number field for $M_\infty = 6$ in T-313.

4.1.2 Description of the model

The experimental model is made at the scale 1:3 according to the geometry of the body. The forebody consists in four parts (details): the nose, lower and upper parts, and a body (see figure 4.6). The forebody is made from alloyed steel to provide the necessary strength. During the experiments in T-313 blow down wind tunnel, the forebody is mounted on a holder. Measurement points on the surface of the forebody are located outside of the

Figure 4.6: Photograph of the forebody.

vortices (figure 1.31), 8.5mm away from the plane of symmetry. The surface of model is equipped with points of measurements for static pressure, as shown in figure 4.7

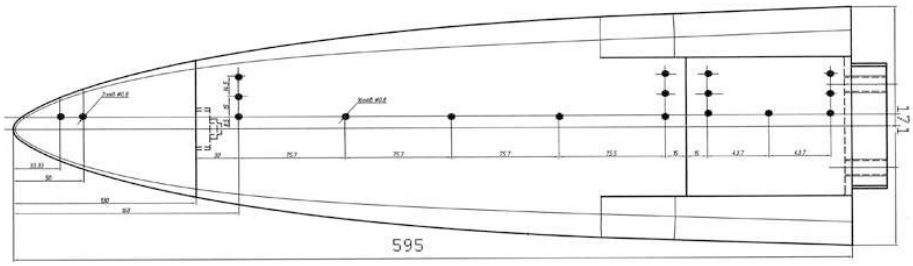

Figure 4.7: Scheme points of static pressure.

4.1.3 Description of measurements by Pitot pressure rake

The position of laminar-turbulent transition is detected using Pitot rakes, by the change in total pressure measured along surface. Two special rakes with 3 Pitot tubes have been designed to obtain a transition location along three lines in a single run. One rake has the tip of its tubes flattened down to a size of 0.1mm for $M_\infty = 4$ and the other to a size 0.2mm for $M_\infty = 6$. These values have been defined by previous experiments for flat plate in T-313 and laminar boundary layer thickness calculations (see 2.6). The drawing of rakes, the photograph of rakes and their installation are shown in figure 4.8, 4.9 and 4.10 respectively. Each of the Pitot tube is connected to an independent electrical circuit. The rake is moved downwards until one of the tubes is in contact with the wall. The rake can then be moved along the body. The displacement amplitude is limited to 200mm. Displacement rate of displacement device is about 1mm/s and accuracy along x about 1mm and 0.1mm along y abscissa. The model has to be moved to investigate all length of the forebody by displacement device.

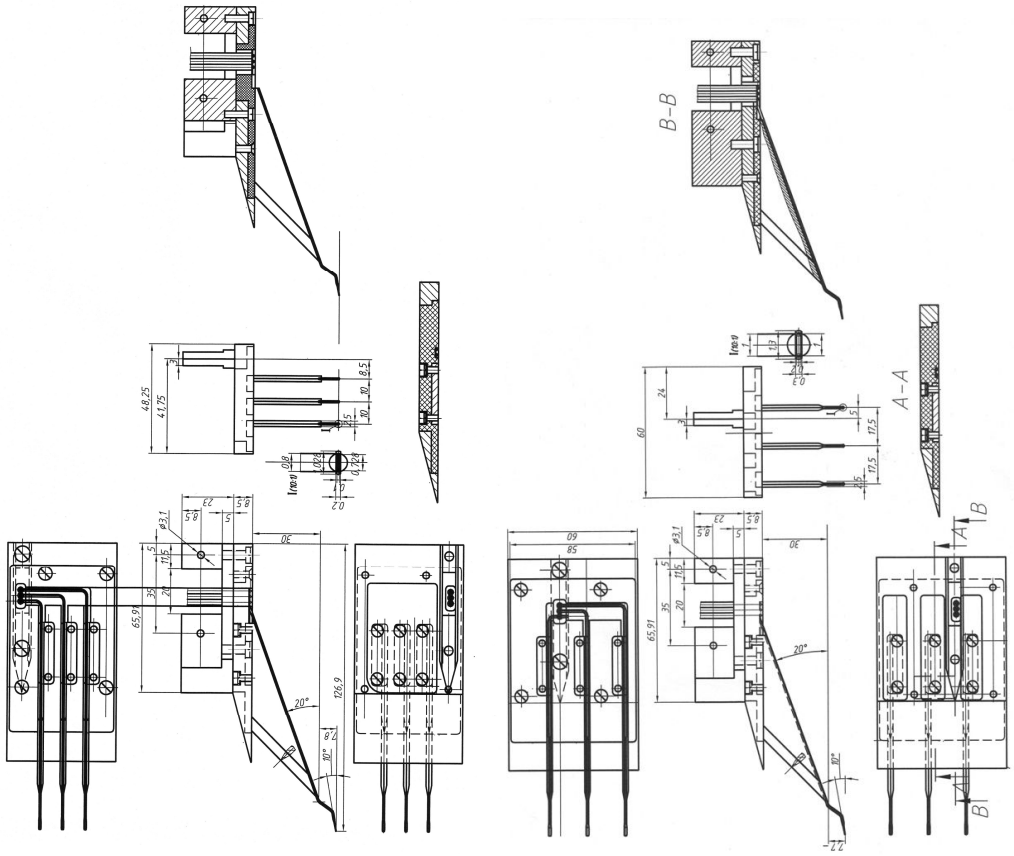

Figure 4.8: Drawing of the rakes.

At $M_\infty = 4$, transition is expected near the nose of the forebody. Hence, the distance between Pitot tubes is set to 10 mm. It allows starting measurements 25 mm downstream from the nose with the two tubes at $z = 8.5$mm and $z = 18.5$mm (the tube at $z = 28.5$mm is outside of the body at this abscissa). For the $M_\infty = 6$ rake, the distance between tubes is 17.5 mm in order to cover the maximum area of investigation. This value is also chosen for all the tubes to be within the width of the compression ramp, which is $z = 50$mm ($z = 8.5$mm, $z = 26$mm and $z = 43.5$mm). At side slip angle 2°, it was foreseen a possibility to conduct measurements by Pitot tubes rakes on both sides of the forebody.

4.1.4 Gauges

Pressure gauges from the firm "Infineon" are used to measure the static and Pitot pressure. Gauges with nominal 1.6bar (KPY-43 A) and 4bar (KPY-44 A) are used. A special calibrating device with 0.05% precision is used for their calibration. Such an example of calibration is displayed in figure 4.11. These data show the linear response of the gauges within an accuracy of 0.2%. Nominal of pressure gages chosen thus to avoid during experiments overload and keep maxsimum sensitivity of gauges. Value of pressure in experiments are calculated previosly (see section 2.2). Gauges placed in heat-insulated box (pressure gauges are sensitive to temperature) are connected with Pitot tubes by short pipelines (< 30sm) to avoid long time infilling of pipelines.

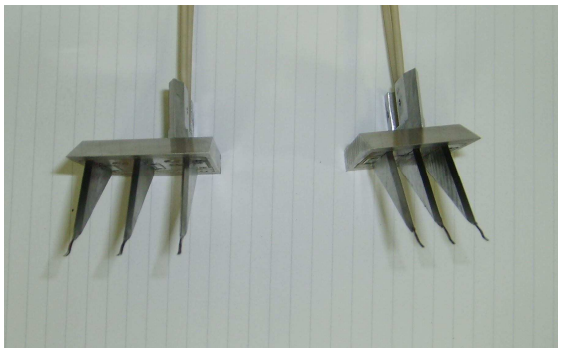

Figure 4.9: General view of the rakes.

Figure 4.10: Installation of the forebody and the rake in T-313.

Figure 4.11: Example of pressure gauges calibration.

4.1.5 Flow visualization

Schlieren and/or oil flow visualization have been done. Schlieren also allows checking visually the contact between Pitot tubes and the forebody surface during the experiment (figure 4.12). In the case of oil flow visualization, the forebody is installed as shown in 4.13, in front of the optical windows of the wind tunnel side walls to observe the surface of the forebody. This model installation permits to perform visualization directly during the experiment.

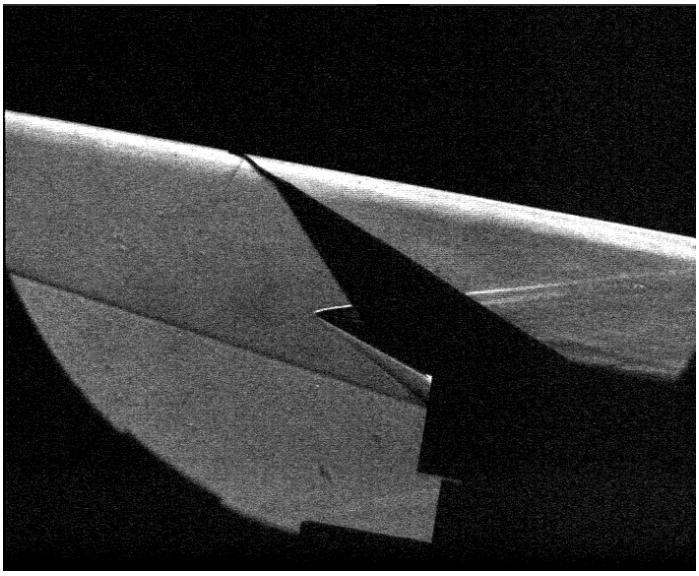

Figure 4.12: Schlieren visualization, M =6, AoA=4°

Figure 4.13: Installation of the forebody for oil-flow visualization.

4.2 Results of experiments

All the experiments for $M_\infty = 4$ and $M_\infty = 6$ have been done at AoA=4°. Special run 2916 has been performed to see effect of slip angle β=2°. Main parameters are gathered in table 4.1. Runs 2917 to 2919 have specially been done for oil-flow visualization. During a run, the total parameters of the flow vary slightly as shown in figures 4.14 and 4.15. The sudden increase in P_0 during run 2913 is due to the operator in order to recover the nominal parameters. It can be observed larger variations in the flow parameters at $M_\infty = 6$ than at $M_\infty = 4$, probably this is related to the use of heater of the flow. Hence, the following results about Pitot pressure measurements are made dimensionless by the corresponding

Table 4.1: flow parameters for the runs in T-313.

Run code	M_∞	P_{tot}(bar)	T_{tot}(K)	Re_u x 10^{-6}(1/m)	visualization
2913	4	10.3	283	49.4	Schliren
2914	6	8.5	380	10.9	Schliren
2915	6	8.2	380	10.5	Schliren
2916	6	8.4	370	11.1	Schliren
2917	6	8.0	320	13.9	oil flow
2918	6	8.0	320	13.9	oil flow
2919	4	10.0	283	48.0	oil flow

instantaneous total pressure.

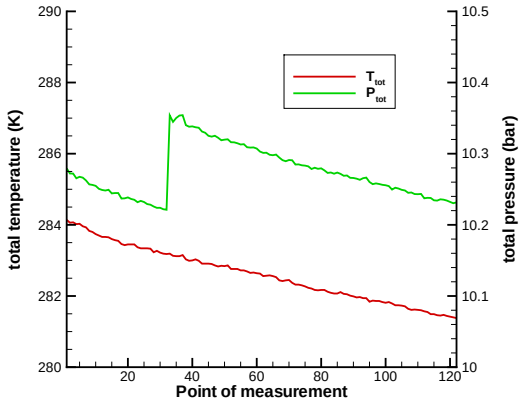

Figure 4.14: Variations of total parameters during run 2913, $M_\infty = 4$.

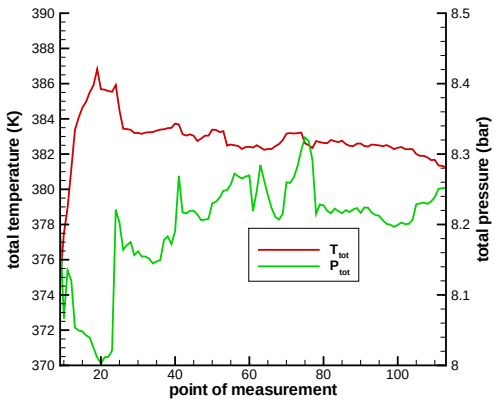

Figure 4.15: Variations of total parameters during run 2915, $M_\infty = 6$.

4.3 Global characteristics and structure of the flow

Figure 4.16 shows a nice visualization of the leading shock at $M_\infty = 4$ (run 2913). Figure 4.12 shows an up-side-down image of the Pitot rake in run 2914, $M_\infty = 6$. The lighter near-wall region corresponds to the boundary layer, warmer hence of lower density than the outer flow.

An oil flow visualization of the wall friction lines for $M_\infty = 4$ is shown in figure 4.17. It confirms the presence of crossflow from the separation line near the nose leading edge toward the plane of symmetry. An oil flow visualization for $M_\infty = 6$ at middle part of the model is shown in figure 4.18. The dark trace with width ∼15% of compression ramp in the symmetry plane illustrates these vortices.

4.4 Experimental determination of transition

All of the results are presented in the coordinate system (x, y, z) attached to the wall and used for stability calculations.

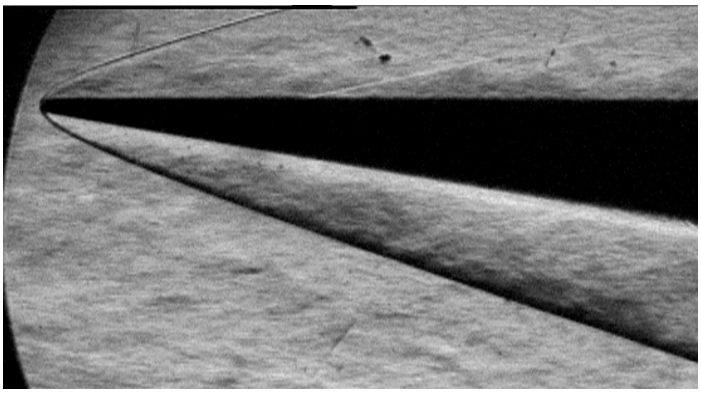

Figure 4.16: Schlieren visualization, run 2913, $M_\infty = 4$.

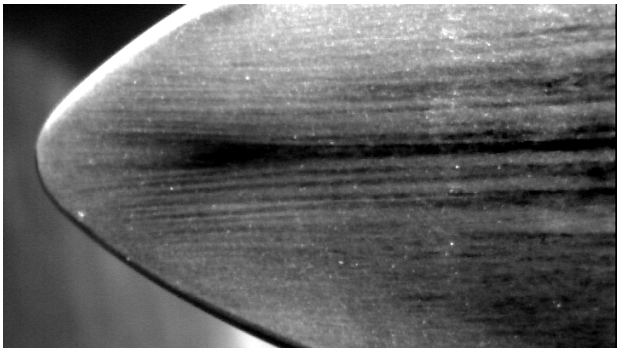

Figure 4.17: Wall friction lines show crossflow toward the plane of symmetry, $M_\infty = 4$.

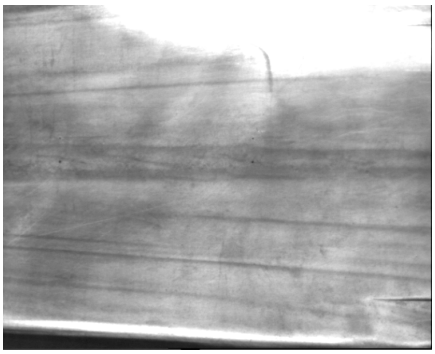

Figure 4.18: Oil flow visualization, $M_\infty = 6$.

4.4.1 M_∞=4, AoA=4°, β=0°, run 2913

Figure 4.19 shows the evolution of the Pitot pressure measured and computed along the lines of corresponding color drawn in figure 4.20. One can clearly see an increase in Pitot pressure (beginning of transition) up to maximum (end of transition), followed by a decrease typical of a turbulent boundary layer. In the calculations, the computed Pitot pressure is averaged on the Pitot tube height and confirms qualitatively the trend. The average Pitot pressure decreases because the boundary layer thickness increases. It is recalled that transition in the calculation is just obtained by turning the turbulence model on after the nose region quite arbitrarily. A laminar calculation does not correlate with the experimental data : transition has really occurred. This is confirmed by the Pitot pressure profiles measured at $x = 25$mm and $x = 205$mm (round dots at the ends of lines in figure 4.20). At $x = 25$mm, Pitot pressure profiles are those of a laminar boundary layer (figure 4.21). A calculation with the turbulence model turned on produces by the way almost similar results. One can notice that the outermost tube (squares/blue color, $z = 28.5$mm) gets in touch with the wall only after $x \approx 50$mm. Hence, at $x = 25$mm, this tube is outside the shock and the measured profile is that of the free stream at $M_\infty = 4.05$. On the contrary, at $x = 205$mm, figure 4.22 shows that Pitot pressure profiles measured and computed agree quite perfectly.
Conclusion : At $M_\infty = 4$, in the conditions of run 2913, transition occurs very close to the nose. According to the peaks of Pitot pressure observed in figure 4.19, one can estimate the end of transition at $x \approx 35$mm.

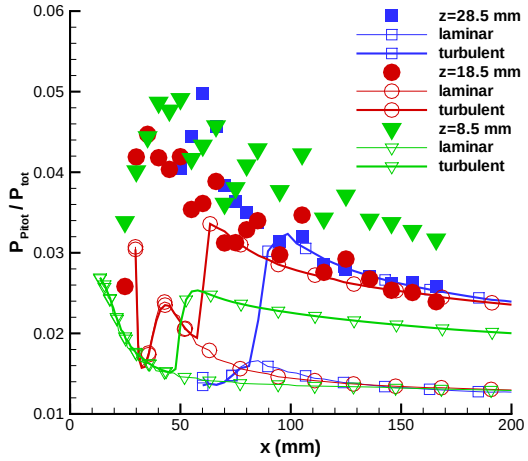

Figure 4.19: Pitot pressure measured (filled symbols) and computed along x on lines shown on figure 4.20 : run 2913, $M_\infty = 4$.

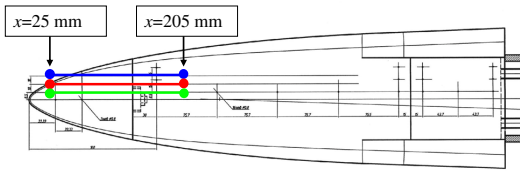

Figure 4.20: Lines of measurement along x for Pitot pressure distribution of figure 4.19, and location of Pitot pressure profiles of figures 4.21 and 4.22.

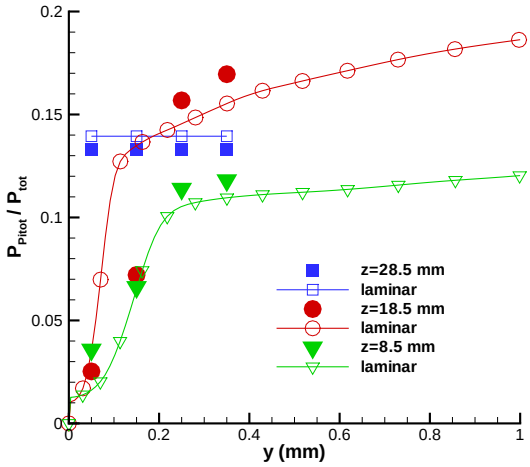

Figure 4.21: Measured (filled symbols) and computed Pitot pressure profiles, $x =$ 25 mm : run 2913, $M_\infty = 4$.

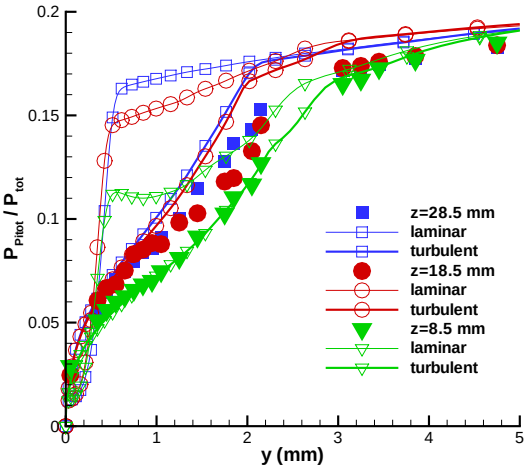

Figure 4.22: Same as figure 4.21, $x = 205$ mm.

4.4.2 M_∞=6, AoA=4°, β=0°, runs 2914 and 2915

During runs 2914 and 2915, the unit Reynolds number is much lower than during run 2913 (see table 5.2). Hence, transition is expected in the middle of the forebody. The model is placed in the test section such that measurements begin at $x = 219$mm. Figure 4.23 shows the Pitot pressure measured along the lines of figure 4.24. The beginning of transition is observed immediately for the outermost gauges. During run 2914, the Pitot pressure always increases except a peak located at $x \approx 320$mm and $z = 43.5$mm. This suggests that the end of transition is not reached during run 2914. This has been the reason for run 2915 during which the model has been placed 100 mm downstream, also allowing to test the repeatability of the measurements.

The differences between the results of run 2915 and run 2916 for the tubes located at

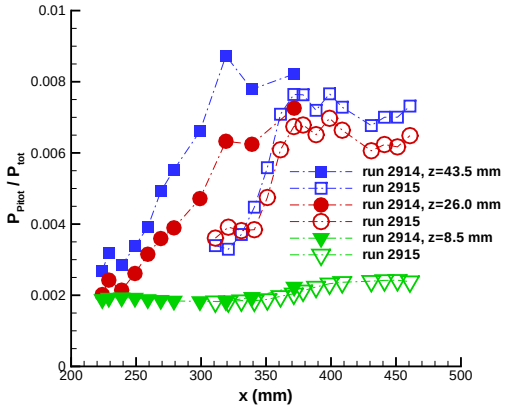

Figure 4.23: Pitot pressure measured along x during run 2914 (filled symbols) and run 2915 (open symbols), on lines shown on figure 4.24 : $M_\infty = 6$.

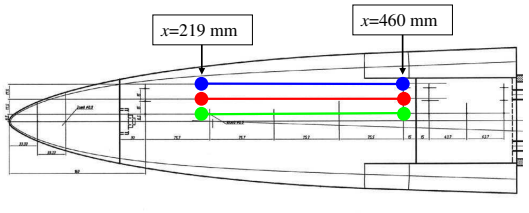

Figure 4.24: Lines of measurement along x for Pitot pressure distribution of figure 4.23, and location of Pitot pressure profiles of figures 4.25 and 4.26.

$z = 43.5$mm and $z = 26$mm have two probable causes:

1. the unit Reynolds number has changed from 10.9 $\times 10^6$/m to 10.5 $\times 10^6$/m delaying the beginning of transition

2. the position of the rake has probably been controlled by the tube at $z = 8.5$mm for which the data coincide, the other tubes being at slightly different altitudes during the different runs

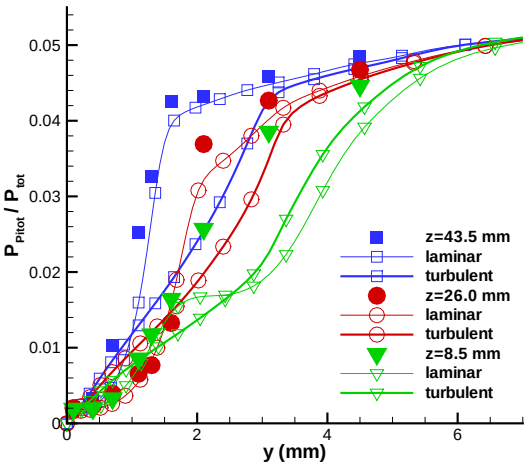

Figure 4.25: Measured (filled symbols) and computed Pitot pressure profiles, $x = 219$mm, run 2915, $M_\infty = 6$.

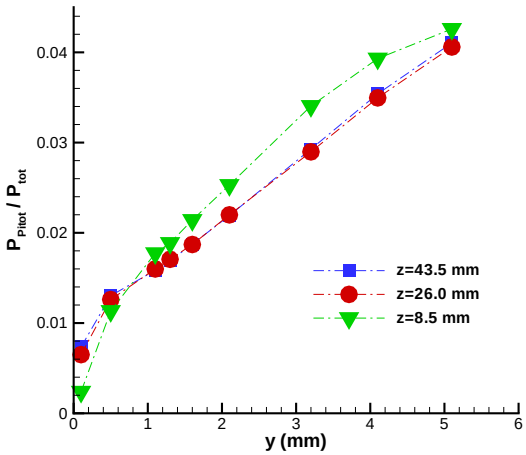

Figure 4.26: Measured Pitot pressure profiles, $x = 460$mm, run 29, $M_\infty = 6$. Calculations have not been done at this location.

The Pitot pressure profiles measured at $x = 209$mm are very similar to those of laminar calculations (figure 4.25). On the other hand, the profiles of figure 4.26 measured just before

the compression ramp of the air inlet are typical of a turbulent boundary layer (very "filled" profile and thick boundary layer). Calculations have not been done at this location.
Conclusion : At $M_\infty = 6$, in the conditions of runs 2914 and 2915, transition occurs at $x \approx 220$mm for the gauges at $z = 43.5$mm and $z = 26$mm, and at $x \approx 300$mm for the gauge at $z = 8.5$mm, close to the plane of symmetry. The end of transition is respectively $x \approx 360$ mm for the two former gauges and $x \approx 400$mm for the later.

4.4.3 M_∞=6, AoA=4°, β=2°, 2916

The distribution of Pitot pressure at slip angle β=2°, measured during run 2916, is presented in figure 4.27 together with the data from runs 2914 and 2915 in order to check the effect of the slip angle on the transition location. Positions of the probes on the forebody surface in run 2916 are indicated by color lines in figure 4.28. It is seen that the slip angle has little effect on the location of the laminar-turbulent transition.

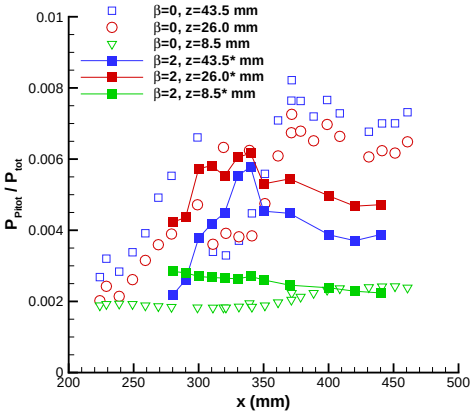

Figure 4.27: Pitot pressure measured along x during run 2916 (filled symbols) and run 2914, 2915 (open symbols).

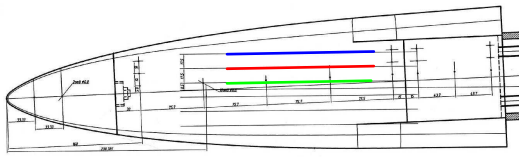

Figure 4.28: Lines of measurement along x for Pitot pressure distribution of figure 4.27. Run 2916.

4.5 Natural transition: comparison calculations/experiments

As already mentioned in the introduction, laminar/turbulent transition predictions in flight are reliable only if the same method is able to successfully predict the transition in ground test conditions. This section reports the comparison between the predicted and observed transition during experiments.

4.5.1 Wind tunnel N factors

Since the transition prediction is based on the LST coupled with the e^N method, it relies on the value of the N factor at transition. In flight conditions, the usually accepted value is $N \sim 9$ to 10. In ground test conditions, one has to know the N factors of the (conventional) wind tunnel to apply the method. They have been determined from a flat-plate experiment [49], in the Mach number range $M_\infty = M_e = 2.5$ to 6 and for two values of the unit Reynolds number : $Re_u = 11 \times 10^6$ 1/m and 16×10^6 1/m (figure 4.29). The leading edge bluntness of the plate is r=0.05mm. Open symbols show the beginning of experimental transition

and filled symbols show the end. Transition Re number for the forebody is given (diamond symbols) together with the flat plate experiments (gradient symbols are for $\mathrm{Re}_u = 11 \times 10^6$ 1/m and squares are for 16×10^6 1/m). The common tendency that the transition Reynolds number, Re_{tr}, increases with increasing Mach number is observed. The laminar-turbulent transition on the forebody begins earlier compared to the flat plate. Several reasons can be identified like: the bluntness of the nose and CF. One has also to notice that the abscissa of the graph in figure 4.29 is $\mathrm{M}_\infty = \mathrm{M}_e$ for the flat plate and M_∞ for the forebody.

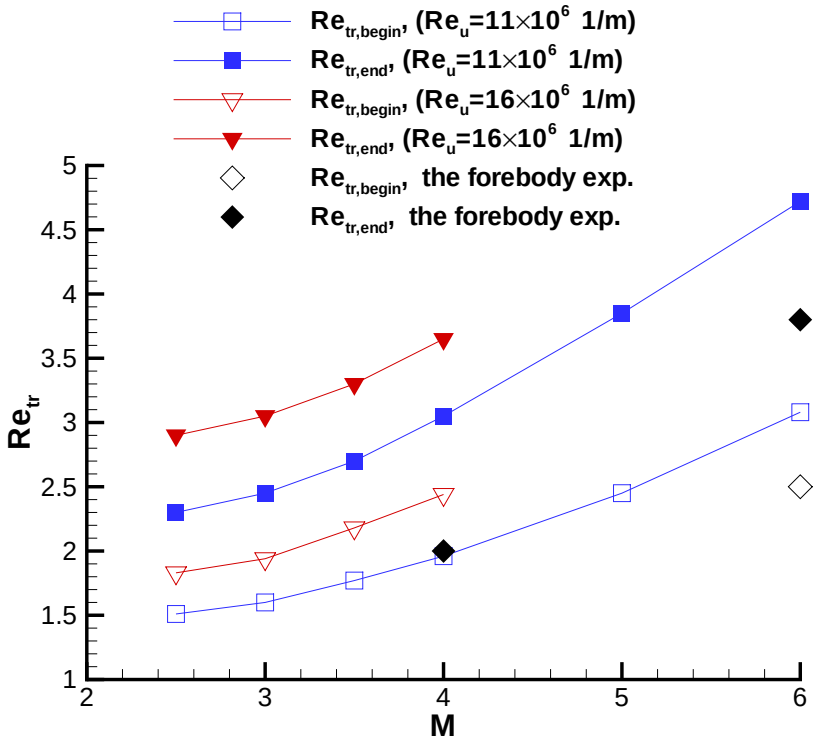

Figure 4.29: The laminar-turbulent transition Reynolds number on the flat plate and on the forebody.

The flat-plate mean flow has been computed from self-similar Levy-Lees solutions with an adiabatic wall and the LST has been applied for several frequencies ranging from 10kHz to 120kHz. At Mach numbers below 4, the most unstable waves are Mack's oblique first modes for which the envelope method has been applied at each location to find the direction of propagation ψ_M giving the maximum longitudinal amplification ($\beta_i = 0$ for a 2-D mean flow)

$$\psi_M(x) = \max_{\psi} |\alpha_i(x)| \tag{4.1}$$

At Mach number 5, the first mode begins to weaken and Mack's acoustic 2^{nd} mode ($\psi_M = 0$) appears but is not yet prevailing. At Mach number 6, the 2^{nd} mode is predominant. Then, the curves

$$N_f(x) = \int_{x_0}^{x} -\alpha_i(\xi)|_{\psi=\psi_M}\, d\xi \tag{4.2}$$

are drawn for each frequency f. In equation (4.2), x_0 is the upstream abscissa of the neutral curve for f. The procedure to obtain N factors for the beginning and end of transition is illustrated in figure 4.30 for the case $\mathrm{M}_e = 3$ and $\mathrm{Re}_u = 11 \times 10^6$ 1/m. The intersection of the line $N(x)$ which envelopes the total amplification curves $N_f(x)$ with the lines $x = x_{begin}$ and

$x = x_{end}$ of experimental beginning and end of transition give the corresponding $N_{tr,begin}$ and $N_{tr,end}$ factors. Results are given in table 4.2 and plotted in figure 4.31.

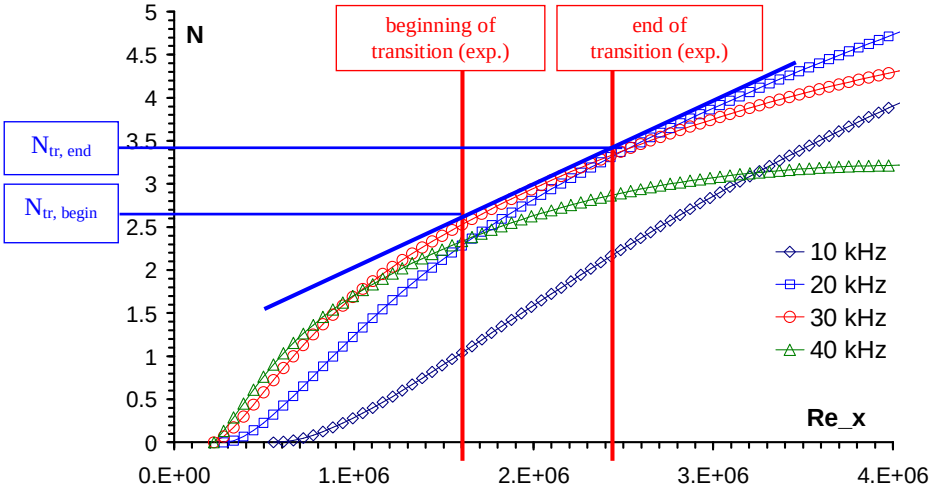

Figure 4.30: Illustration of the determination of $N_{tr,begin}$ and $N_{tr,end}$ at $M_e = 3$.

Table 4.2: N factors of beginning and end of transition for a flat-plate in the blow-down wind tunnel.

	$Re_u = 11 \times 10^6$ (1/m)		$Re_u = 16 \times 10^6$ (1/m)	
M_e	$N_{tr,begin}$	$N_{tr,end}$	$N_{tr,begin}$	$N_{tr,end}$
2.5	2.35	3.15	2.70	3.60
3	2.55	3.40	2.90	3.90
3.5	2.80	3.80	3.20	4.30
4	3.00	4.25	3.40	4.60
5	2.65	3.65		
6	2.90	4.00		

In fact, calculations have been done *before* the experiments on the forebody in T-313, for estimated values of the experimental conditions. The parameters of calculations are gathered in table 4.3, to be compared with table 4.1. In the case of run 2913, the Mach

simulated run	M_∞	P_{tot} (bar)	T_{tot} (K)	P_{st} (Pa)	T_{st} (K)	Re_u (1/m)
2913	4	10.8	282	6415	67.0	49.6×10^6
2914, 2915	6.06	8.07	400	516	48.0	9.3×10^6

Table 4.3: Parameters of calculations to simulate experimental runs.

number outside of the boundary layer on the forebody is in the range $3.4 - 3.6$, although the unit Reynolds number is much higher than in the flat-plate experiments. In the case of runs 2915 and 2916, $M_e \sim 4.2 - 4.7$ and the unit Reynolds number is almost the same as in the flat-plate experiments. Hence, the transition on the forebody is due to a 1^{st} mode instability (and also to a crossflow instability as will be shown later), the free stream Mach number being too low for the second mode to play a role. One can then consider that a

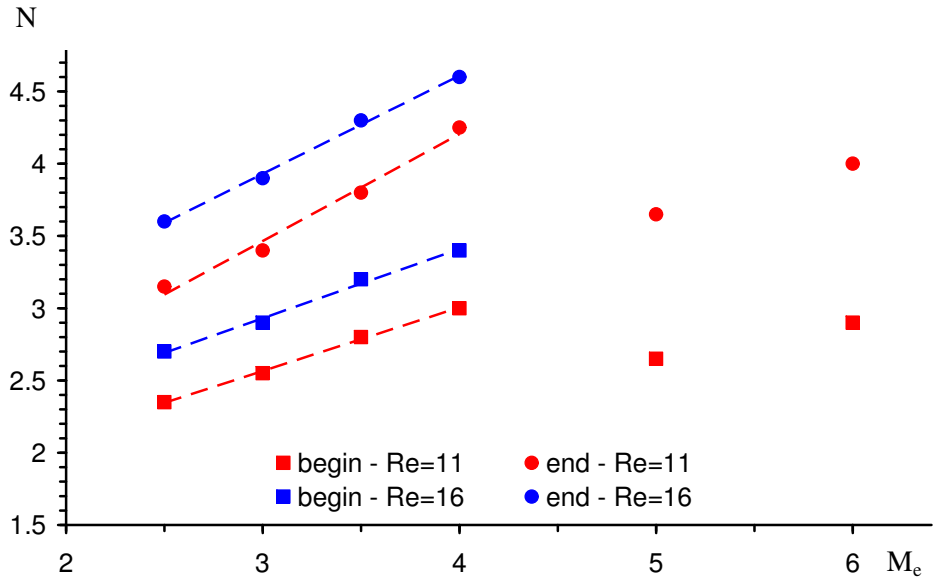

Figure 4.31: Graph of the values listed in table 4.2 with linear fits.

value $N \approx 4$ is globally representative of the end of transition in the wind tunnel in the case of a dominant oblique 1^{st} mode instability.

4.5.2 Comparison at $M_\infty = 4$: run 2913

Figure 4.32 shows the results of the LST for run 2913, for the single frequency $f = 30$ kHz that has been found to be the most unstable. The LST is very difficult to converge in the white areas near the nose which have marginal instability. Figure 4.33, which is a zoom of figure 4.32 on the nose region, shows from the computed wall friction lines that theses areas correspond to the 3D separation lines on the forebody. The direction ψ_M of propagation of the most unstable waves is always lower that 80°, indicating an oblique 1^{st} mode instability for which the flat-plate calibration applies directly, with some uncertainty however due to the difference in the Reynolds numbers. Figure 4.34 shows the map of the computed N factors over which the points of experimental end of transition determined in subsection 4.4.1 have been superimposed. They fall at places where $N \sim 1 - 4$. The integration of amplification factors done according to equation (1.14) starts at the edge of the zone of interest (see figure 1.3) where the amplification is not zero : it is not the neutral curve. Nevertheless, $N(s = 0)$ is set arbitrarily to zero. Hence, in the computation of N factors, it "misses" the total amplification for the area situated between the neutral line and the beginning of the integration path on the edge of the zone of interest. This is mainly true near the leading edge for the gauge located at $z = 28.5$ mm where the N factor is clearly too weak. On the other hand, the transition point measured by the gauge located on the line $z = 8.5$ mm close to the symmetry plane is just at $N = 4$. The black lines drawn on figure 4.34 are the integration paths tangent to the group velocity.

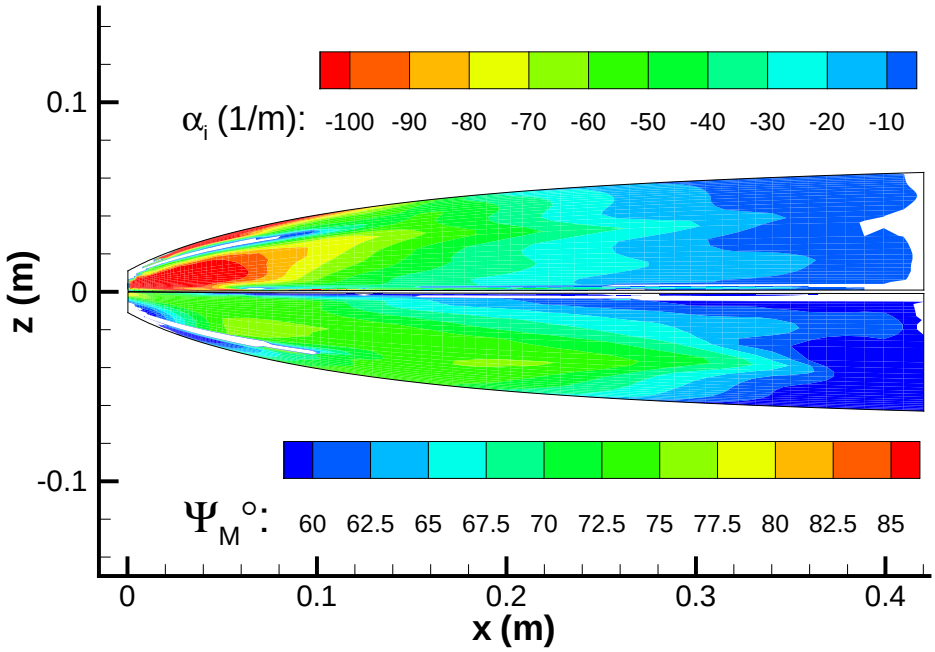

Figure 4.32: Stability results : run 2913, $M_\infty = 4$, $f = 30$ kHz.

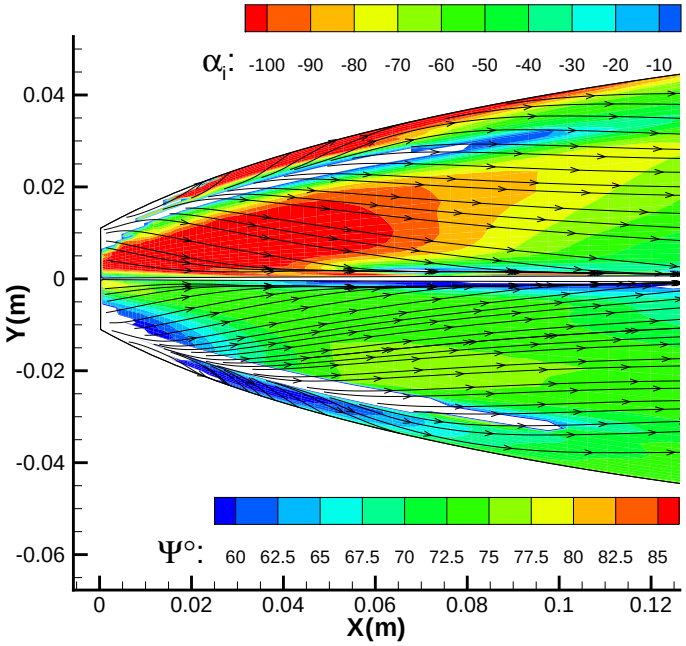

Figure 4.33: Same as figure 4.32: zoom on the nose region and wall friction lines indicating a 3D separation line.

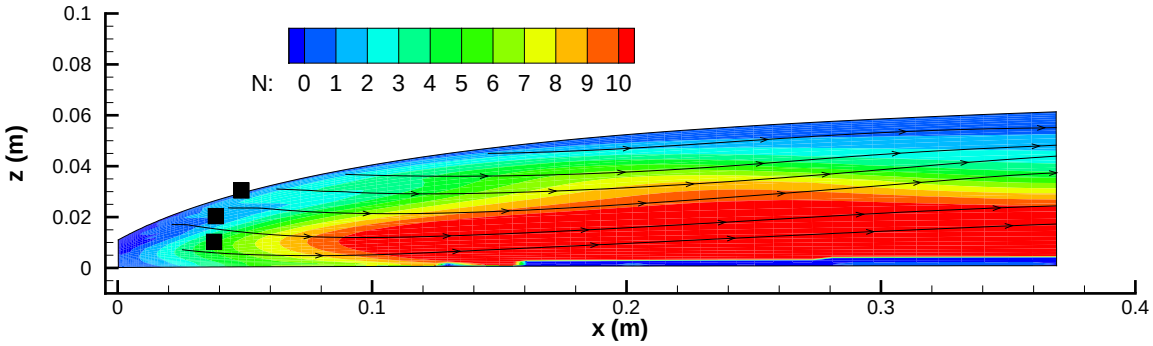

Figure 4.34: Computed N factors and points of experimental end of transition : run 2913, $M_\infty = 4$.

4.5.3 Comparison at $M_\infty = 6$: runs 2914 and 2915

At $M_\infty = 6$, the instability is clearly of the CF type near the nose and progressively turns to oblique 1^{st} mode downstream (figure 4.35). The investigated frequency is again $f = 30$ kHz. In the computation of N factors, one can integrate all (Global Integration, GI) or only a part (Discriminant Integration, DI) of the CF instability, by taking into account amplification rates of waves associated with a propagation angle ψ_M lower than a prescribed value. Flat-plate calibration will be valid for longitudinal transition.

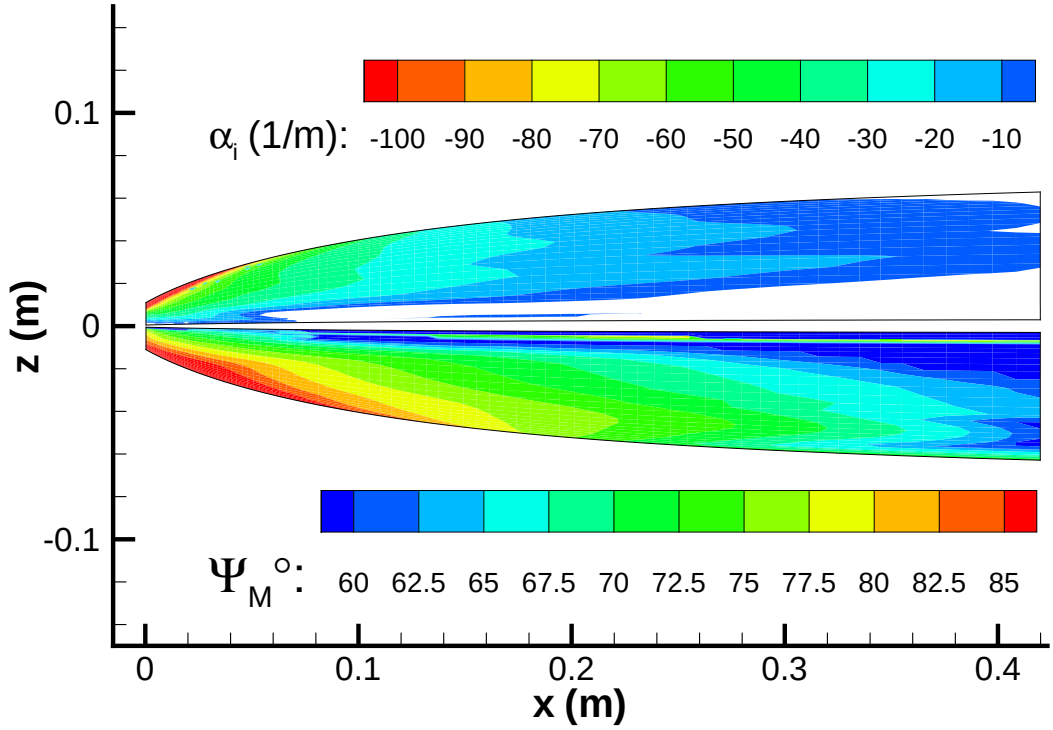

Figure 4.35: Stability results : run 2914 and 2915, $M_\infty = 6$, $f = 30$ kHz.

Figure 4.36 shows N factors obtained by the GI method (top), by the DI method with $\psi_M < 85°$ (middle) and by DI with $\psi_M < 80°$ (bottom), together with the experimental points of beginning and end of transition. In the GI strategy, N factors are too high compared

to flat-plate calibration values, because the CF instability is very high at the nose ($\alpha_i \approx -100$ 1/m, top of figure 4.35). It is the same for the DI strategy with $\psi_M < 85°$. On the contrary, the DI strategy limited to $\psi_M < 80°$ hence integrating only TS waves, produces N factors for beginning and end of transition in good accordance with the reference value $N \approx 4$, except for the region near the plane of symmetry where the influence of longitudinal vortices is out of the scope of the local LST (parallel flow assumption). Anyway, it should be emphasized that the shape of unstable regions or iso-N contours is very similar to the experimental transition area.

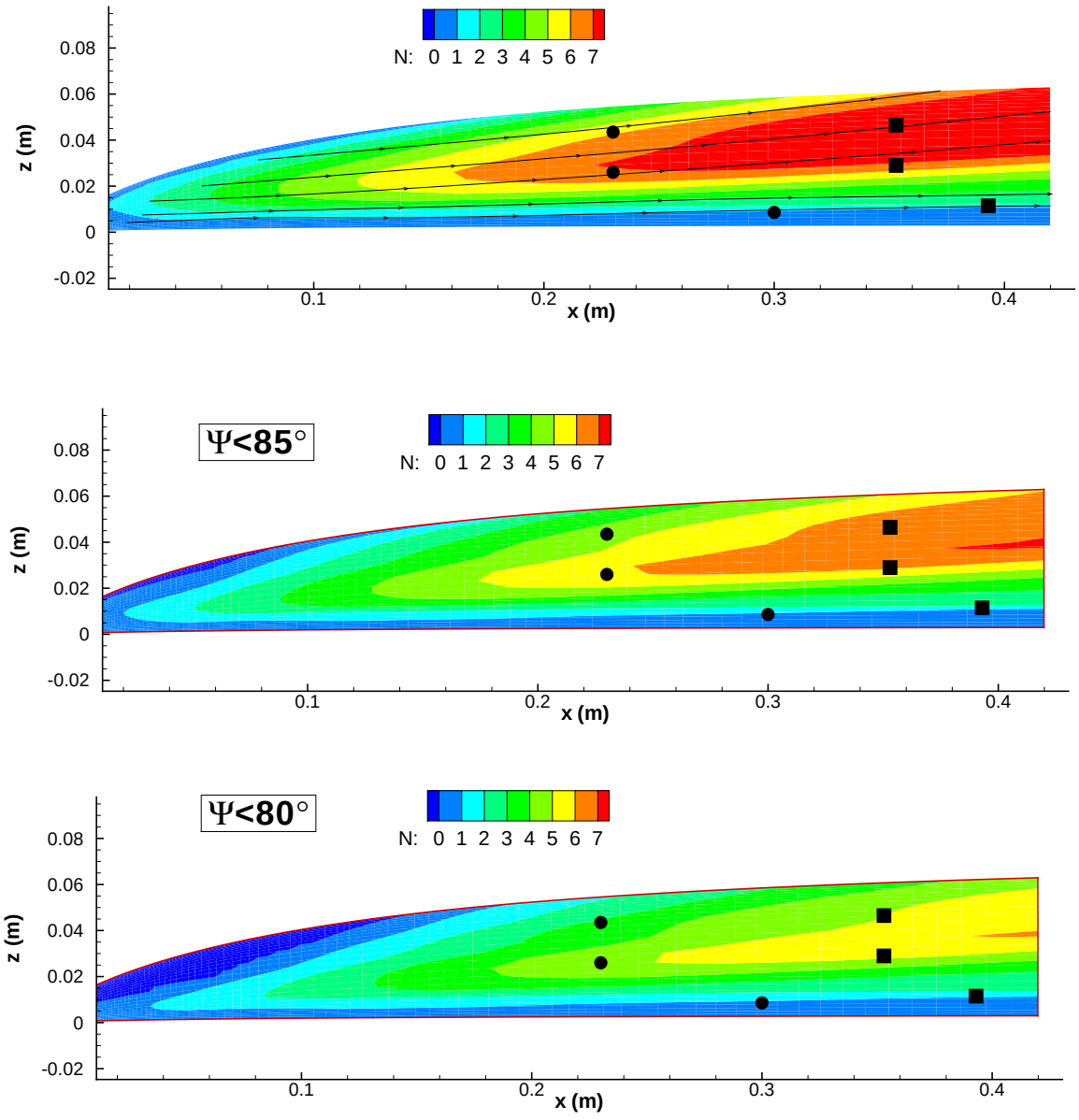

Figure 4.36: Computed N factors: GI (top), DI ψ_M <85° (middle) and DI ψ_M <80° (bottom). Round dots and squares are respectively the experimental beginning and end of transition: runs 2914 and 2915, $M_\infty = 6$.

4.6 Summary and conclusion

I: Experiments

According to the results of the experimental investigation, the position of the laminar-turbulent transition zone has been determined for Mach numbers $M_\infty = 4$ and $M_\infty = 6$. From the obtained results, the following conclusions can be drawn:

- The transition Reynolds number, Re_{tr}, increases with increasing Mach number (figure 4.29).
- At Mach number $M_\infty = 6$ and zero slip, the transition is delayed near the symmetry plane.
- A slip angle β=2° does not influence significantly the position of transition in that part of the forebody where investigations are made.

II: CFD

The crossflow found in numerical simulation has been proved by oil flow oil-flow visualization. Measured and computed Pitot pressure profiles show quite good agreement.

III: LST

The standard LST associated with the e^N method has been applied to a 3-D body in wind tunnel T-313 conditions, and the predicted transition has been compared to the experimental one. As a pre-requisite, N factors for transition in the specific wind tunnel are needed. They have been obtained from flat-plate experiments for which the LST applies easily to self-similar mean flow profiles. However, care should be taken in considering the kind of instabilities involved in the transition process. The flat-plate is only relevant to viscous instability of 1^{st} modes or TS waves. On the other hand, CF instability observed on the forebody is due to inviscid instability of the spanwise inflexional velocity component. In the case of a $M_\infty = 4$ flow, CF instability is weak, and the transition predicted using flat-plate correlations agrees very well with experiments. At $M_\infty = 6$, CF instability is dominant at the nose of the forebody, and evolves smoothly to TS waves downstream. This CF instability has to be removed from the integration process to compute the total amplification to be compared to calibration N factors. The part to be removed is somewhat arbitrary. In the present case, it is found that taking $\psi_M < 80°$ gives a good agreement between predicted and observed transition. This empirical strategy is not in contradiction with the whole methodology since the e^N method is empirical by nature. Further investigations are now needed to confirm or disprove the value $\psi_M < 80°$ to segregate TS from CF waves. This maybe discussed in relation to the N_{TS}/N_{CF} transition methods, in which different transition limits are given for TS and CF transition [74].

Chapter 5

Experimental transition in wind tunnel AT-303: experiments/computations

Synopsis

Ce chapitre est consacré aux essais de transition naturelle et par rugosités à M_∞=6 et M_∞=8 dans la soufflerie à rafale AT-303. La transition est détectée *via* le flux de chaleur pariétal (ou le nombre de Stanton qui en est la forme adimensionnée), reconstruit à partir des mesures de température par peintures thermosensibles (TSP).

On décrit d'abord le principe de fonctionnement de la soufflerie, puis on donne les résultats de calibration des tuyères pour M_{nom}=6 et M_{nom}=8. L'écoulement dans les tuyères est simulé numériquement en régime turbulent pour les conditions d'arrêt expérimentales. Les nombre de Mach obtenus en sortie (resp. 5.75 et 7.65) correspondent bien aux valeurs d'étalonnage. Le diamètre efficace du jet du jet simulé est 320mm.

L'emploi de peintures thermosensibles est très délicat et nécessite une attention particulière dans la préparation de la maquette. On doit notamment réaliser la partie de la maquette à explorer en matière plastique afin d'éviter la diffusion thermique de surface. Ces aspects techniques, ainsi que les courbes d'étalonnage des peintures sont indiqués au troisième point de ce chapitre. On détaille ensuite la chaine de mesure optique, la procédure expérimentale d'acquisition des données, les corrections optiques à apporter aux mesures brutes, et enfin le calcul du flux de chaleur à partir de deux mesures de température décalées dans le temps.

Les résultats montrent que la transition naturelle à M_{nom}=6 a lieu de part et d'autre du plan de symétrie, juste après la jonction entre le nez métallique et la partie plastique de la maquette. La répartition de nombre de Stanton est analysée le long de lignes longitudinales coïncidant avec celles des mesure de pression Pitot dans T-313. La répartition transversale de nombre de Stanton est également étudiée, et comparée aux résultats de calcul Fluent® en laminaire et en turbulent. Les résultats montrent un forte inhomogénéité transversale des flux de chaleur mesurés, et un accord médiocre aux niveaux calculés malgré une tendance globalement similaire. Il faut garder à l'esprit que les calculs en régime turbulent ne prennent pas en compte la position de la transition (calcul "tout turbulent") et doivent donc être considérés avec la plus grande réserve. L'analyse de stabilité a été effectuée avant les essais à

M_{nom}=6, pour des paramètres estimés, légèrement différents des valeurs expérimentales. On trouve une fin de transition pour $N \sim 2$, ce qui est plus faible que dans T-313 : la soufflerie AT-303 est plus bruyante que la T-313.

A M_{nom}=8, la transition naturelle a lieu également, mais un peu plus en aval. Les niveaux de nombres de Stanton mesurés dans les zones laminaires et turbulentes correspondent bien aux valeurs calculées en laminaire et en turbulent. Les répartitions transversales sont très chahutées, et la tendance est reproduite qualitativement par le calcul.

En ce qui concerne la transition par rugosités, tous les essais se sont montrés concluants : les rugosités testées se sont toutes montrées efficaces, sauf au niveau du plan de symétrie où les tourbillons longitudinaux restent très difficiles à déstabiliser. Les plus hautes (1 mm et 1.5 mm) crééent un choc qui provoque un décollement juste en amont. Les mesures transversales de nombre de Stanton juste après les rugosités montrent d'importantes fluctuations spatiales et des niveaux très élevés typiques d'un régime turbulent.

Enfin, on a constaté peu d'effet des angles d'incidence et de dérapage sur les résultats expérimentaux.

5.1 Description of the impulse wind tunnel AT-303

The second part of experiments on the laminar-turbulent transition and roughness-induced transition at $M_{nom} = 6$ and $M_{nom} = 8$ has been done in the impulse wind tunnel AT-303 at ITAM. The laminar-turbulent transition is detected using TSP paints. TsAGI scientists with my assistance provided these experiments. Alexander Shiplyuk, the head of AT-303, was responsible for the design of new nozzles and their experimental calibration. Figures 5.1 and 5.2 show the concept of this wind tunnel. The scheme of gas sources is shown in figure 5.3. Before tests, air is preheated in an electrical storage heater and during the run it is compressed by a piston to the nominal value. The operation time of AT-303 depends on conditions. For example for $M_{nom} = 6$ operation time is about 10 ms, and for $M_{nom} = 8$ increases up to 50ms. At short duration time, the total temperature in AT-303 can reach up to 3000K and the total pressure up to 3000bar. For investigations on the forebody, new profiled axisymmetric nozzles for M_{nom} =6, 7, 7.5 and 8 have been manufactured with exit diameter ∅400mm. Needed Mach numbers are obtained by changing only some parts of the nozzle.

Before tests, all configurations of the nozzle are calibrated. Results of calibration of the nozzles for M_{nom}=6 and M_{nom}=8 are given in table 5.1, where X is the position of Pitot pressure rake from the nozzle exit, M_{mean} average Mach number calculated among core, and σ_M is mean-square deviation. Figure 5.4 shows Pitot pressure rake which is used for calibration. Results of calibration studies show that quite an extended core of uniform flow forms at the nozzle exit plane, with a core diameter of about 300mm. A. Shiplyuk also provided measurements of Pitot pressure pulsation in the AT-303 wind tunnel by high-frequency pressure gauge made by PCB Piezotronics, Inc. (figure 5.4), which enables to measure pulsations of frequencies up to 450kHz. Figure shows 5.5 the Pitot pressure pulsation spectra related to the average Pitot pressure value for the M_{nom} 6, 7, 7.5 and 8.

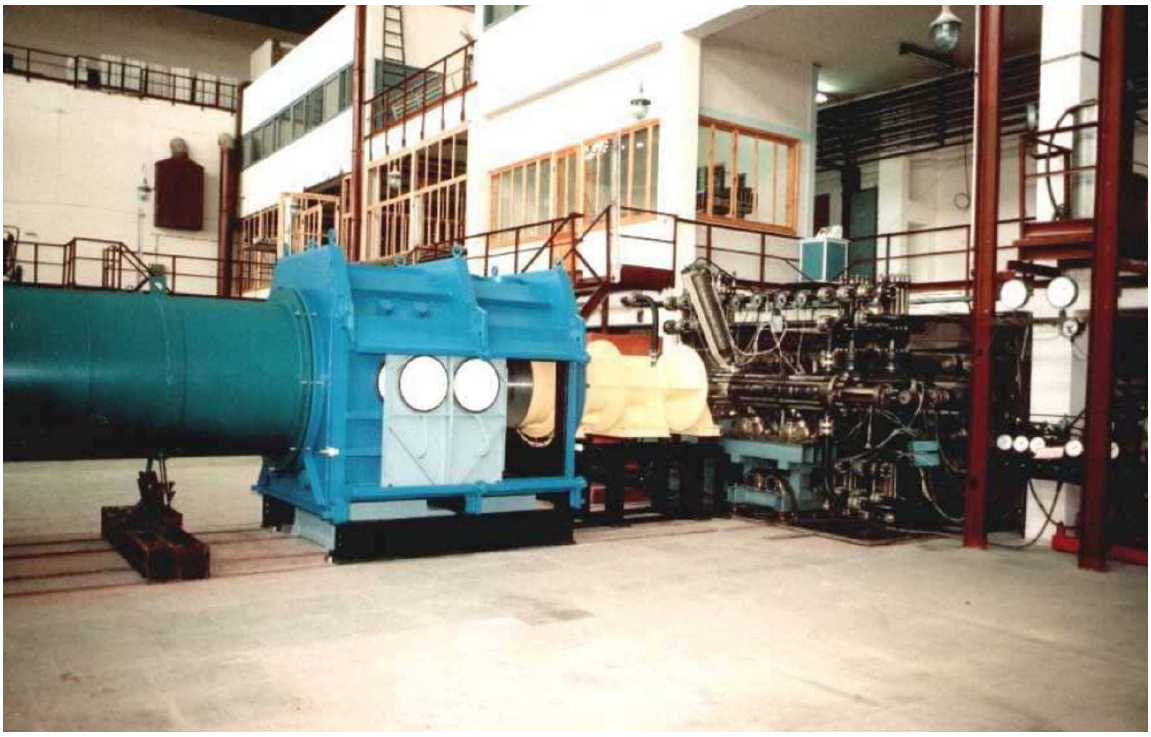

Figure 5.1: Photograph of wind tunnel AT-303.

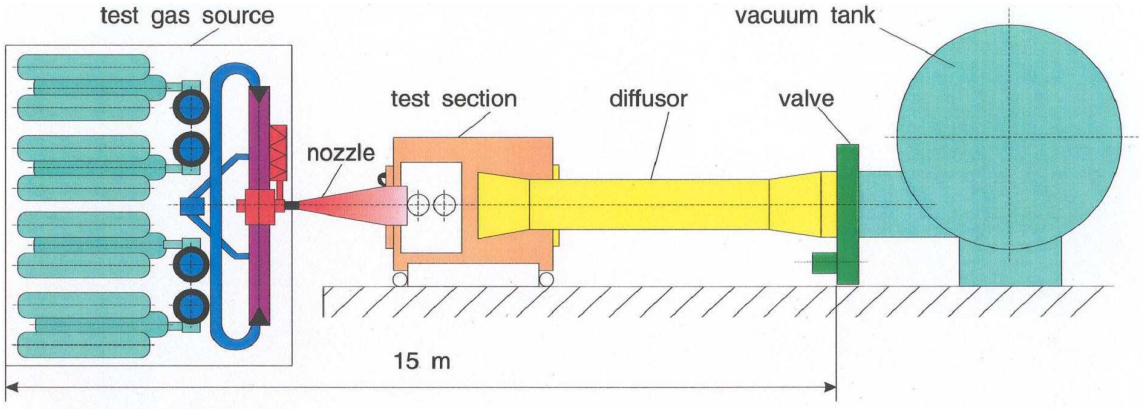

Figure 5.2: Scheme of wind tunnel AT-303.

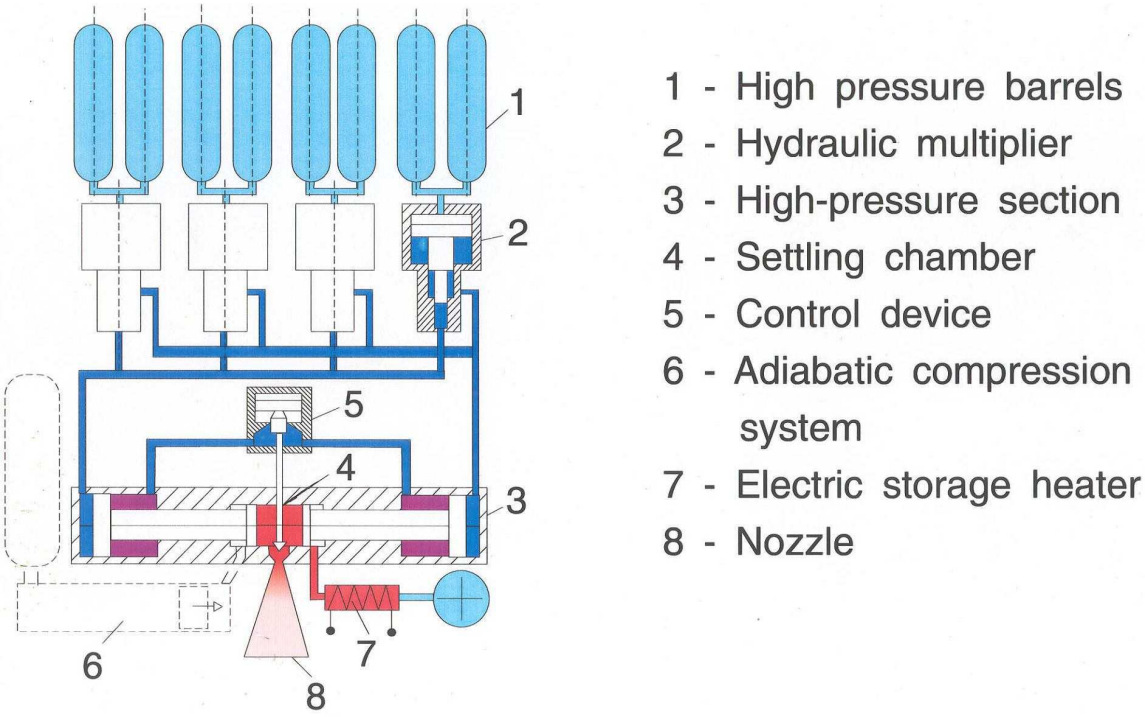

Figure 5.3: Scheme of gas source of AT-303.

M_{nom}	$P_{tot,nom}$ (Bar)	$T_{tot,nom}$ (K)	P_{tot} (Bar)	T_{tot} (K)	Re_u	X (mm)	M_{mean}	σ_M
6	40	1500	53	1470	8.4×10^6	0	5.64	0.034
6	40	1500	48	1565	7.1×10^6	200	5.71	0.027
6	40	1500	48	1580	6.9×10^6	450	5.76	0.031
6	60	1200	62	1280	12.1×10^6	0	5.73	0.040
6	60	1200	68	1320	12.2×10^6	200	5.8	0.026
6	60	1200	63	1250	12.4×10^6	450	5.8	0.032
8	100	1500	104	1500	6.5×10^6	0	7.75	0.025
8	100	1500	104	1500	6.5×10^6	200	7.75	0.055
8	100	1500	104	1500	6.5×10^6	450	7.75	0.033

Table 5.1: flow parameters for the runs in AT-303 at M_{nom}=6 and 8.

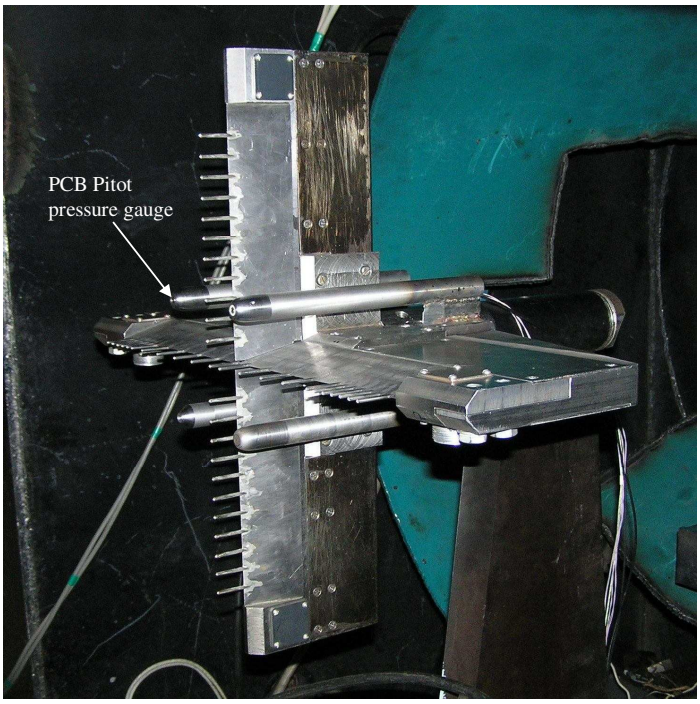

Figure 5.4: Calibration Pitot pressure rake.

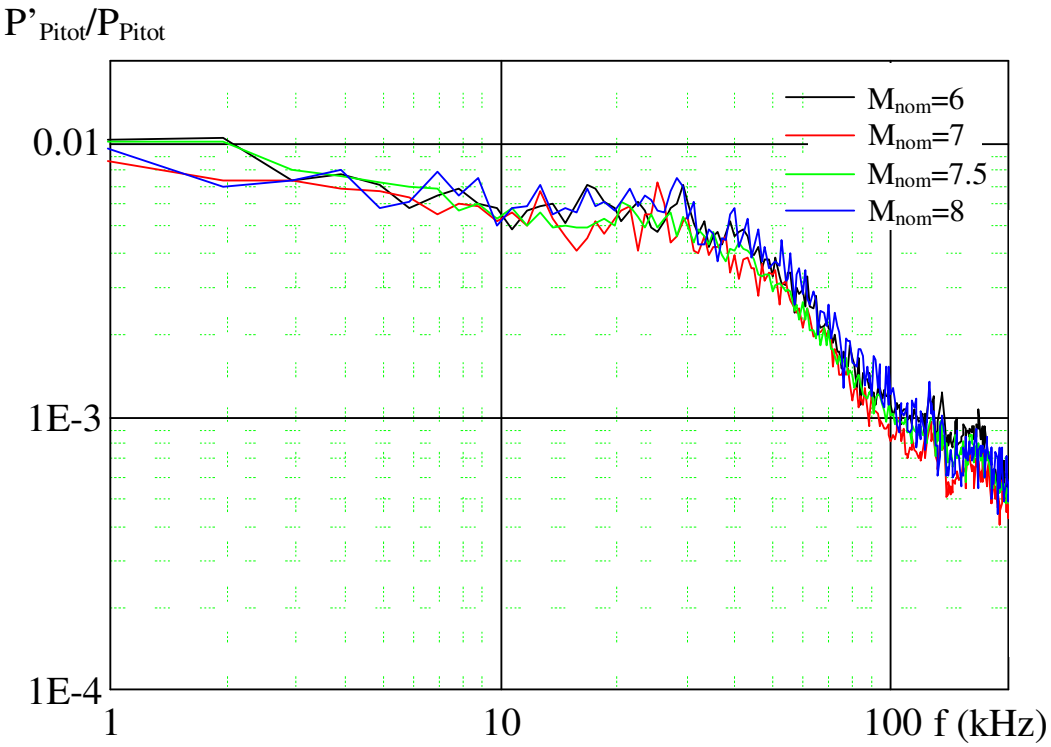

Figure 5.5: Pitot pressure pulsation spectra for various Mach numbers.

A. Shiplyuk gives the following conclusions:

- The normalized *r.m.s.* Pitot pressure pulsations are 3.7±0.2%, 3.3±0.3%, 3.4±0.4% and 3.6±0.1% for M_{nom}=6, M_{nom}=7, M_{nom}=7.5 and M_{nom}=8 respectively.
- Based on these results, it can be concluded that the *r.m.s.* Pitot pressure pulsations weakly depend on the Mach number.
- The double fall in the pulsation amplitude occurs in the frequency band of PCB gauges from 30 to 40 kHz.
- The signal of the rake gauges (not shown here) has typical low-frequency pulsations, which are not observed in the signal of PCB gauges.
- The pressure pulsations level corresponds to the values for ordinary wind tunnels.

This last conclusion is very important for our stability/e^N analysis. Schneider reports that:

" [...] experiments are contaminated by the high level of noise that radiate from the turbulent boundary layers normally present on the wind tunnel walls. These noise level typically 0.5∼1% of mean [...][10, 66]."

It is difficult to convert Pitot pressure pulsations to level of noise in the hypersonic flow (due to compressibility effects), nevertheless the present value 3∼4% in AT-303 seems a little bit higher than the order of magnitude of noise for ordinary wind tunnels.

5.2 FLUENT® simulations of nozzles for M_{nom}=6 and 8

Two-dimensional axisymmetric turbulent simulation in FLUENT® have been done using the Menter's k-ω-SST turbulence model [51]. Figure 5.6 shows the contour of the supersonic part of the nozzle.

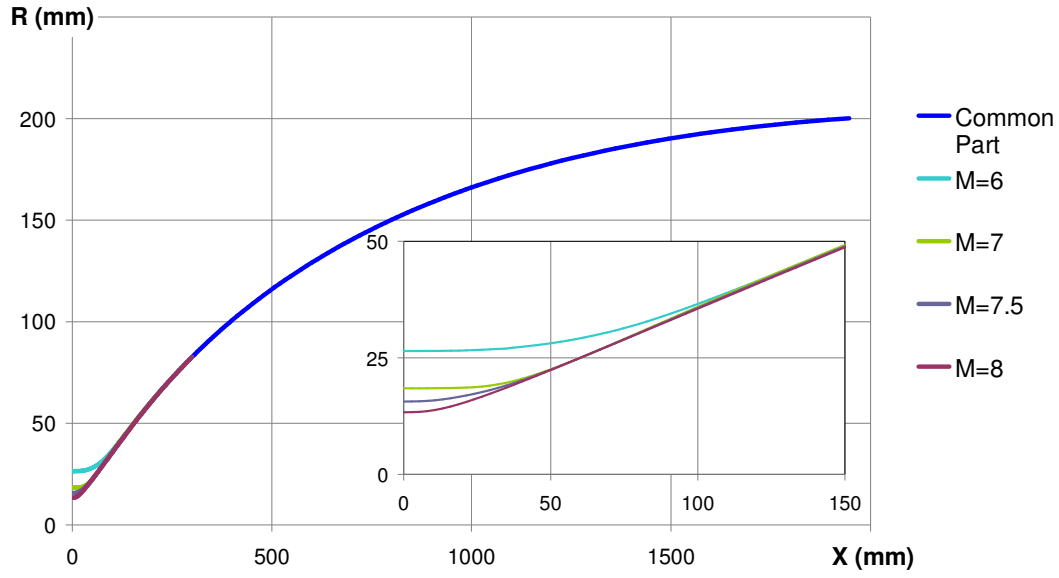

Figure 5.6: Contour of supersonic part of nozzle for AT-303.

Results of computed Mach number fields are presented for the M_{nom}=6 and M_{nom}=8 in figures 5.7 and 5.8. The calculated value of Mach number in the exit M=5.75 for M_{nom}=6 nozzle reproduces accurately the experimental one. The Mach number value of 7.65 in the exit section of the computed nozzle gives a difference less than 1.5% with the value 7.75 in the calibration experiments. The simulated core diameter of the flow is ≈320mm for the M_{nom}=6 and the M_{nom}=8 nozzle.

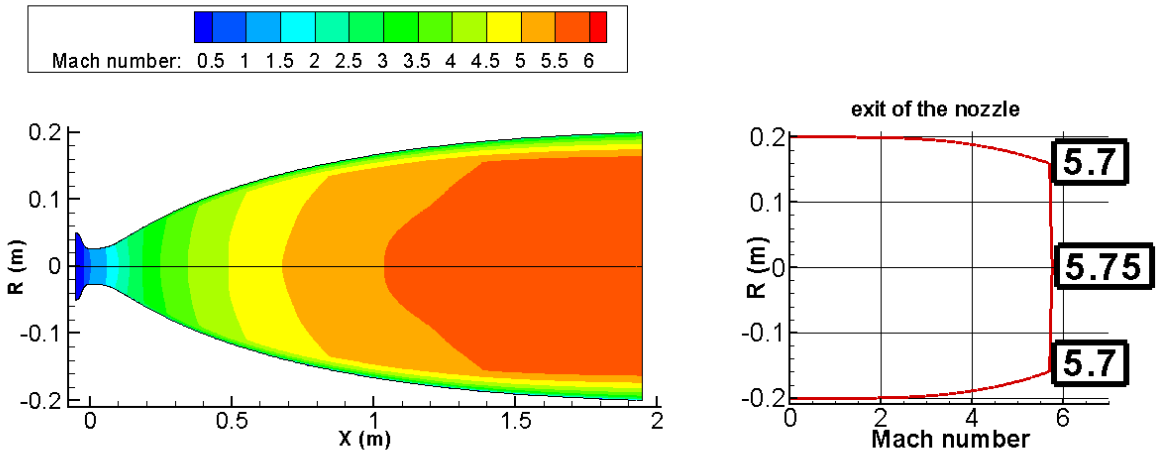

Figure 5.7: Contour of Mach number for M_{nom}=6, P_{tot}=60 bar and T_{tot}=1500 K.

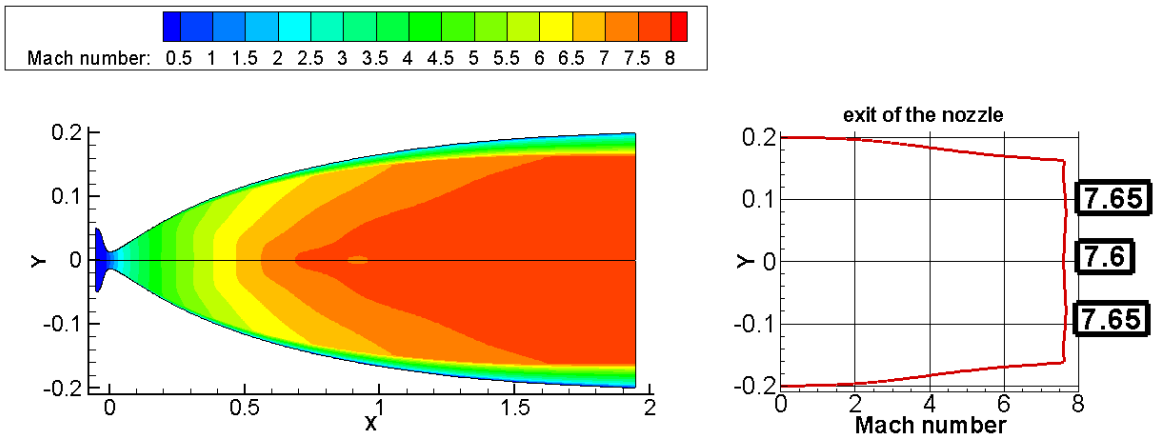

Figure 5.8: Contour of Mach number for M_{nom}=8, P_{tot}=100 bar and T_{tot}=1500 K.

5.3 Temperature Sensitive Paints and preparation of the model

5.3.1 TSP characteristics

In the experiments at ITAM in AT-303, a reversible two-color TSP based on a complex of europium (temperature-sensitive phosphor), Coumarin (reference luminophore) and epoxy resin has been used. The complex of europium (active) has red luminescence, and Coumarin (reference) glows in the blue spectral range. The TSP calibration curve, which is the dependence of the luminescence intensity on the temperature, is shown in figure 5.9. The curve is

normalized by the intensity at 20°C. The optimal temperature for this TSP is 20-60°C. In this range the average sensitivity is 3% /°C. Outside of this range, the luminescence is very low. At a temperature of 80°C, the coating softens (it becomes sticky) and may be deformed under the action of the wall shear stress. At 120°C the irreversible destruction of phosphors contained in TSP begins. It is therefore mandatory to carefully avoid an overheating above 100°C of the TSP during the experiment to ensure its reversibility. Spectral characteristics of TSP are shown in figure 5.10. The luminescence spectrum of sensitive phosphor is very narrow and segregated from the reference phosphor and from the excitation: indeed, it is convenient to separate luminescence from exciting radiation.

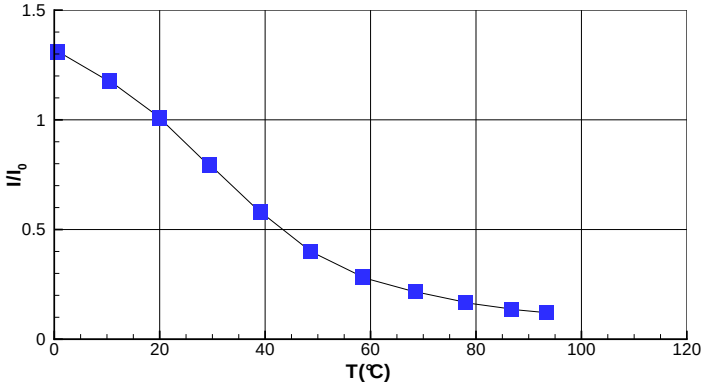

Figure 5.9: Calibration curve of TSP.

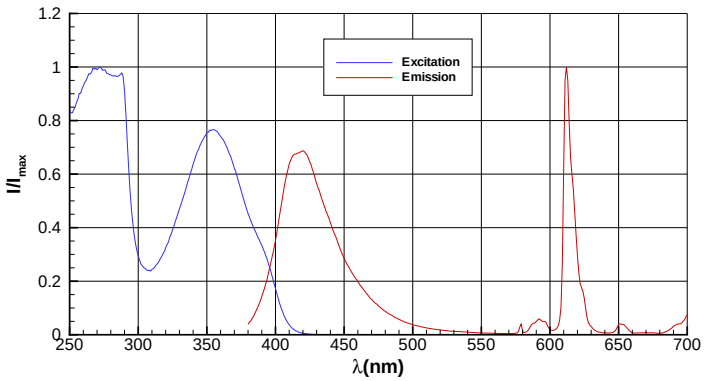

Figure 5.10: Spectrum of excitation and fluorescence of two colors TSP.

5.3.2 Preparation of the model surface

To avoid heat diffusion at the surface of the model, a plastic insulation insert has been used locally instead of the metallic material (see figure 5.11). Before applying the TSP which is almost transparent, the insulation insert is covered with several layers of white epoxy paint (total thickness of about 0.1mm). This layer has several advantages:

- it acts like a mirror and increases both the exciting radiation and the intensity of the coating luminescence by reflection;
- it increases the optical homogeneity of the coating (heat-insulating material has a texture that can lead to noise in division of images);

- it is compatible with the TSP and allows a thin and uniform TSP coating.

Before applying the TSP layer, the white paint is carefully polished with fine sandpaper, which greatly improves the quality of the surface but does not eliminate totally the surface roughness. In order to improve the air inlet, the model has been modified after the application of the white paint. The width of the inlet has been increased; hence some areas are no more covered with the white paint. The white paint has also been removed by polishing the leading edge at the junction with the nose of the model to eliminate the step at the junction. This is visible in the photograph of the model in the work section of the AT-303 shown in figure 5.12. For experimental studies of roughness induced transition, metallic diamond trips with height k of 0.8mm, 1mm and 1.5mm can be installed at locations 150mm and 200mm from the nose as shown in figure 5.13 (see chapter 3).

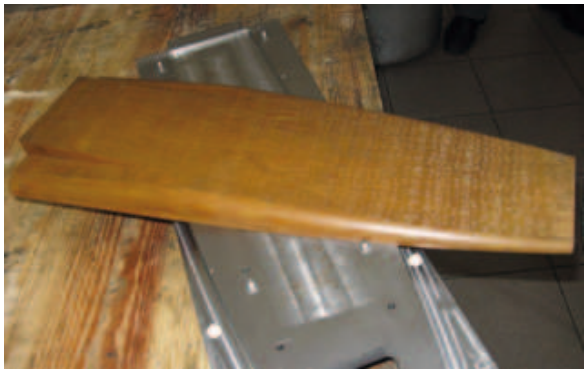

Figure 5.11: Upper plastic part for TSP measurements.

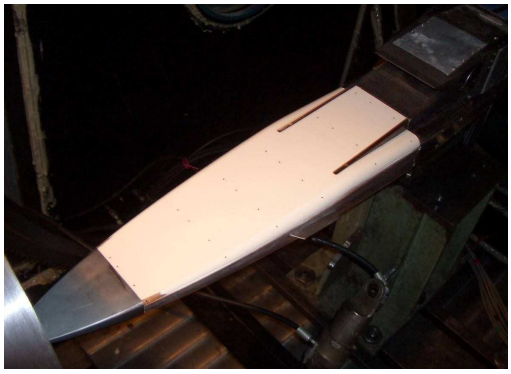

Figure 5.12: The painted model in AT-303.

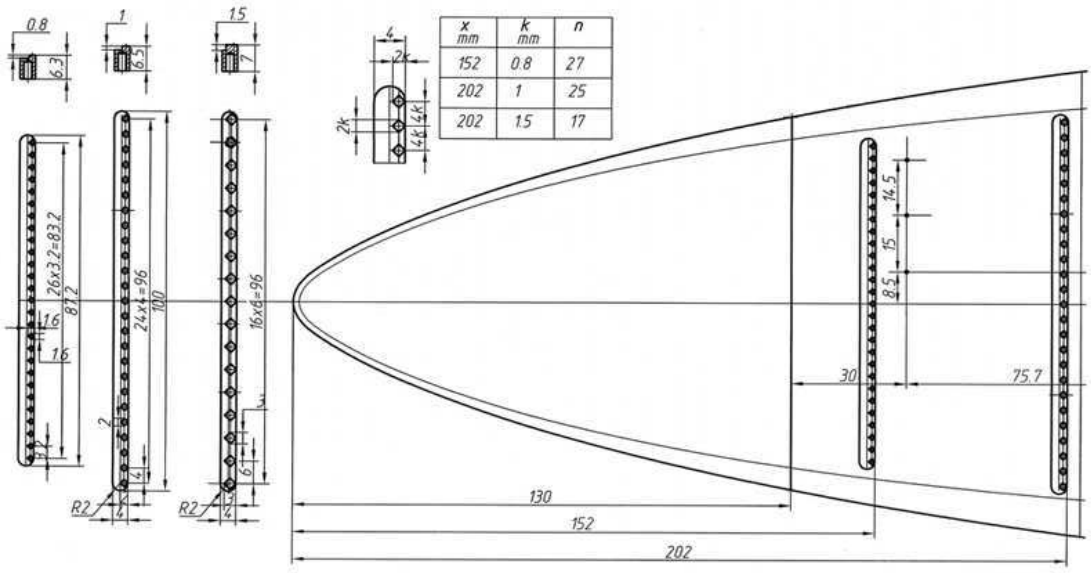

Figure 5.13: Scheme of trips and their installation.

5.3.3 TSP coating

TSP coating is sprayed to the model surface. The thickness of the TSP after drying is from 3 to 5 μm. A metallic sample required to obtain the calibration curve (figure 5.9) is also prepared together with the model. TSP is applied to the model at least 20 hours before the test. This is necessary in order to complete the relaxation processes in the TSP coating after application and to stabilize the calibration curve of the TSP. In order to link the reference images to the wind-on images and the images to the real geometry, markers that are 2 mm dots with no TSP coating are placed on the model. These markers appear as dark dots in ultraviolet light. After the experiments, three-dimensional coordinates of the markers are measured with a measuring machine.

5.4 Measurement system and experimental methodology

5.4.1 The measuring system

The measuring system is constituted with a source of ultraviolet radiation, a CCD camera and an image splitter prism. The luminescence intensity of the model surface with the TSP coating has to be measured in two spectral ranges (400-500 nm and 600-650 nm) at a given time. The measurement time must be less than the duration of a run.

- The flash of UV radiation is produced from two linear laser lamps with filters. The total thickness of the filters on each lamp is 6mm which allows removing the infrared radiations of the lamps in the red channel of the measuring system. A high-power supply is used to supply and ignite lamps. The electrical energy of a flash is about 200J.

- The digital Alta U16M CCD camera equipped with a mechanical shutter is provided by Apogee (USA). The matrix is cooled and has a resolution of 4098 x 4098 pixels. The pixel size is 9 x 9μm. A 16-bit ADC is used to record images.

- The image splitter prism giving two separate images of the object to the matrix is installed before the camera lens (focal length 50mm). Glass filters placed before the faces of the prism select the appropriate spectrum range. Hence two images of the same object in two different spectral areas can be sent to a single matrix at the same time (5.14) [72]. Figure 5.15 shows the images of the model obtained with the splitter (Figure 5.16), slightly distorted by the lenses.

The lamps and the camera are installed in a window on the top of the work section of the wind tunnel, 1m above the model, as shown in Figures 5.17. The work section is darkened to prevent unwanted incoming light.

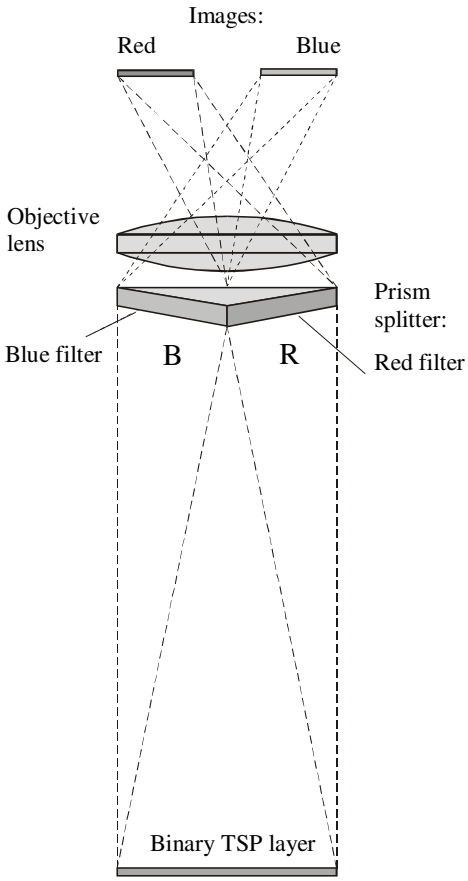

Figure 5.14: Metodology of two pictures on single frame

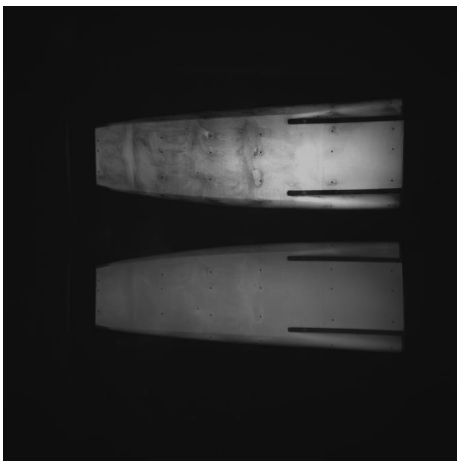

Figure 5.15: Image of luminescence through splitter.

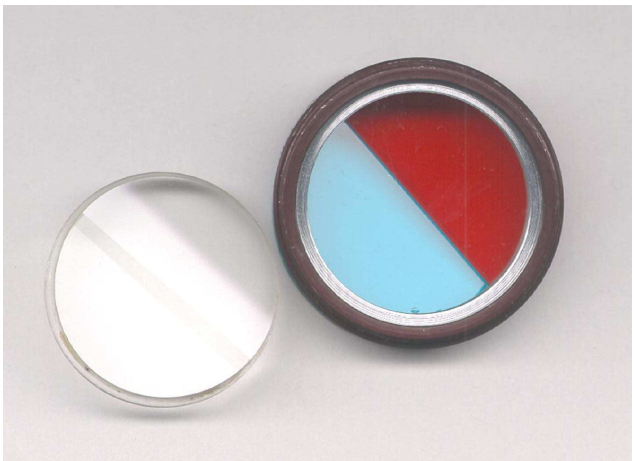

Figure 5.16: Prism splitter and color filters.

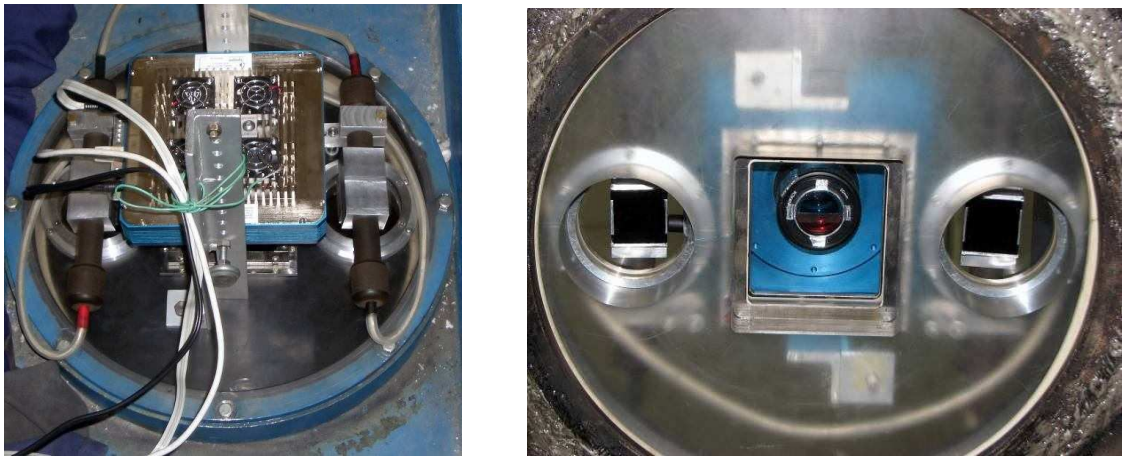

Figure 5.17: Placing of measuring system on top window of work section.

5.4.2 Experimental methodology

The time sequence of a run is the following:

1. t=0ms: *starting of the wind tunnel.* More than 1 second is needed for the pressure to increase in the pressure chamber. This time depends on stagnation pressure and temperature, but it is quite stable (± 1ms) for fixed parameters of flow;

2. t=1050ms: *starting of the measurement sequence.* At this time, triggered by the time generator, the mechanical shutter of the camera starts to open. It takes about 40 ms to be fully opened. The pulse with fixed delay (100ms at $M_{nom} = 6$, item 5) is sent to the lamps by camera;

3. t=1090ms: *mechanical shutter of the camera opened.*

4. t=1140ms: *setting up of the flow.* The duration time is about 10ms at $M_{nom} = 6$ (figure 5.22) and , 50ms at $M_{nom} = 8$ (figure 5.22);

5. t=1150ms ($M_{nom} = 6$): *flash of the lamps.* The flash duration is less than 1.5ms. The camera shutter is closed after the flash.

Three images of the model in two spectral ranges are needed to obtain the temperature field: the reference image recorded at a known uniform temperature model, wind-on image recorded at the time of measurement and the dark image recorded without flash. Reference and dark images are recorded before each experiment. During the run, the model may be moved under the action of aerodynamic loads. Hence the position of the model on the reference and on the wind-on images may not coincide. Using the markers, the images with and without flow are made coincident, and the ratio of intensities of luminescence at each point of the model is computed.

5.4.3 Correction of optical errors

The pixels of the CCD matrix are non-uniformly sensitive, mainly due to vignetting. This error may be eliminated by normalization of images with a “flat field” image. The flat field image is obtained by recording a uniformly illuminated screen. For each of the two

images formed by the splitter, a "flat field" is recorded separately, the other half of the prism being closed to the light. A view of the "flat field" image for the lens with a splitter is shown in figure 5.18. Intensity is represented in pseudocolor. A correction of the distortion of the lens with the splitter prism is necessary for the presentation of geometrically undistorted results on the flat plate, and to correctly transfer the results on the 3D mesh describing the geometry of the model. The correction is achieved by recording a reference object with contrasted points whose coordinates are precisely known. Imaging of the reference object is made only for the red image, because the processing of the blue image is combined with the red one. An image of the reference object is shown in figure 5.19. The following distortion model is used:

$$r_d = F_d r^3 \tag{5.1}$$

with r - the radius of the original undistorted pixel from the center of distortion (x_{d0}, y_{d0}), r_d - the radius of the distorted pixel, F - the coefficient of distortion. The coefficient of distortion and the coordinates of the center of distortion are found from the reference object, so as the rectangular grid of markers is the most accurately restored from its distorted image.

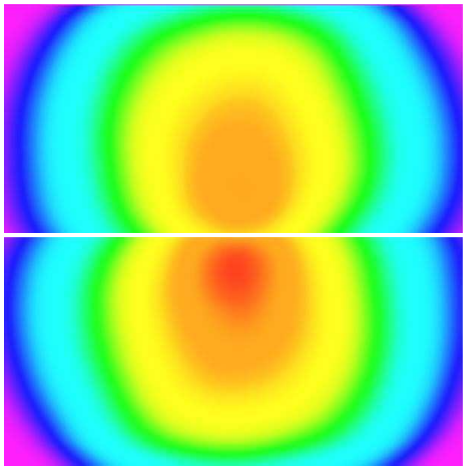

Figure 5.18: View of "flat field" (top - "red" half image, down - "blue").

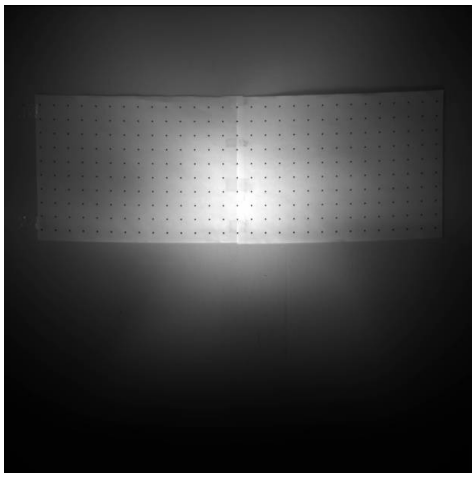

Figure 5.19: View of sample with known coordinates for red chanel.

5.4.4 The problem of parasitic light

During the experiment, some "parasitic" light - the cause of which is not clear - is observed on the red image, but not on the blue one: it is of thermal nature. This light is present not only on the surface of the model, but also in the flow. Figure 5.20 (a, b) shows the luminous tracks of particles flying out from the nozzle. The particles themselves can shine or reflect light coming from the pre-chamber. Pure gas at temperatures of 1200-1500K can not produce light. The parasitic light strongly varies from run to run, sometimes reaching 25% of the useful signal in intensity. It causes a non-uniform overestimation of the wind-on image intensity hence an underestimation of the temperature and of the heat flux down to negative values. A solution to this problem would be to use a camera with an electronic shutter to reduce the parasitic light by a factor 100, but none was available at the time of experiments. The distribution of parasitic light over the surface of the model has been investigated in a $M_{nom} = 6$ experiment without flash of lamps. The result, shown in

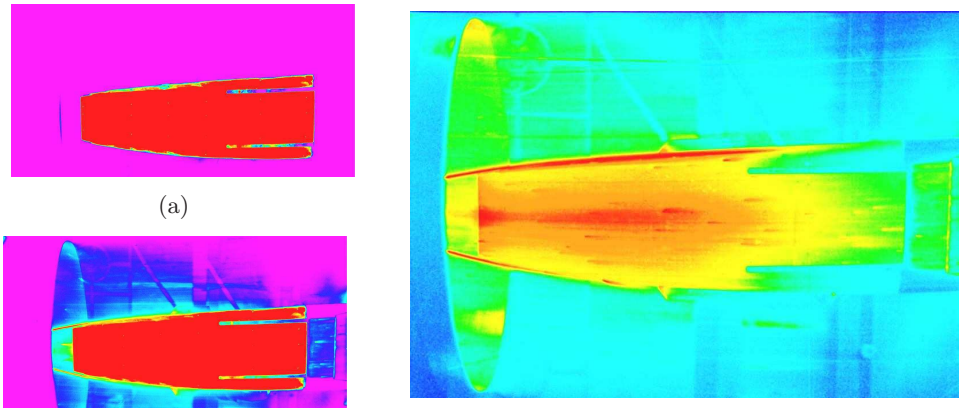

(a)

(b)

(c)

Figure 5.20: Distribution of parasitic light on the surface of the of the model.

figure 5.20 (c), indicates a low level of illumination but of complex distribution, probably not repeatable from run to run. The level of parasitic light is higher on the sidewall of the model facing the nozzle. The spots on the surface of the model seem to be markers of large particles colliding with the surface. The value of the parasitic light on the white-painted insulated part is approximately two times higher than on the metallic part of the nose of the model. This is used to model the parasitic light to be subtracted from measurements as a correction. The 2-parameters (A, x_0) model is built as follows: it is assumed that the parasitic light comes from the nozzle and decreases from the nose to the end of the model like the square of the distance from the light source, the transverse distribution being uniform

$$I_{pl} \approx \frac{A}{(x - x_0)^2} \tag{5.2}$$

This roughly agrees with the distribution presented in figure 5.20 (c). The location x_0 of the source of parasitic light is adjusted manually so the corrections of temperature near the nose and near the end of the forebody are quite adequate. For $M_{nom} = 6$, the source of parasitic light should be near the throat of the nozzle, and for $M_{nom} = 8$ near the nozzle exit. The level of parasitic light is tuned by hand with the constant A to be twice its value on the metallic nose of the model. It should also match the constrain of avoiding areas with too low, especially negative, heat fluxes.

5.5 Method of data processing

The data processing is the following:

- Separation of individual images in the red and blue spectrum range
- Subtraction of parasitic light modeled approximately as previously described from the red wind-on image
- Subtraction of the dark images from the wind-on images and the reference images
- Correction of all the images using the corresponding “flat field”
- Using the markers on the model surface, make all images (blue, dark, and reference) coincide to the red (temperature sensitive) image

- Division of the sensitive (red) image by the blue image, and wind-on images by the reference (no wind) images
- Finding of the temperature fields based on the calibration curve (see figure 2.1) obtained by testing a sample of TSP coating with the calibration camera. The calibration curve is nonlinear, therefore, the temperature of the model has to be taken into account in the recorded reference frames
- Calculation of the heat transfer coefficient h ($W/m^2.K$) and of the Stanton number St (see below)
- Masking of the markers, cutting the patterns and spatial filtering of the images
- Correction of distortion by formula (5.1)
- Last operation: transfer the field of Stanton numbers on a 3D grid that describes the geometry of the model. After this operation, the image of the model with the measured heat flux field can be viewed from any direction

5.5.1 Calculation of the heat transfer coefficient and of the Stanton number

The energy balance can be used to compute out of temperature measurements the amount of heat which comes from the flow to the model. An example how heat flux can be recovered from the time evolution of the temperature measurement is demonstrated. The left-hand side of equation (5.3) is the Fourier law. The right-hand side of equation (5.3) is the heat taken from the flow per second on the surface S, where $\rho_m S l$ is the mass of an insulated piece of model (for example a thermocouple), C_m the heat capacity of the material, ΔT_m the temperature increase of the model during the time interval Δt. The time evolution of the temperature of the surface S finally gives the heat flux which comes from the flow to the model.

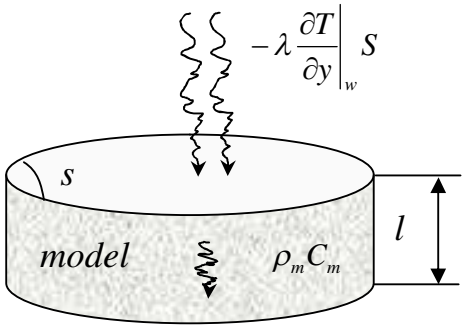

$$-\lambda_{air} \left.\frac{\partial T}{\partial y}\right|_w S = \rho_m C_m l \frac{\Delta T_m}{\Delta t} S \qquad (5.3)$$

Figure 5.21: Illustration of (5.3).

Heat transfer coefficient and of the Stanton number distributions are obtained from the value of the heat flux q from the flow to the model:

$$q = h(T_r - T_{init,m}) \qquad (5.4)$$

$$\mathrm{St} = \frac{q}{\rho_\infty V_\infty C_{p,air}(T_r - T_{init,m})} = \frac{h}{\rho_\infty V_\infty C_{p,air}} \qquad (5.5)$$

where ρ_∞, V_∞, $C_{p,air}$ are respectively the density, velocity and heat capacity of the flow, T_r and $T_{init,m}$ the recovery temperature (it was decided $T_r \approx T_{tot}$) and the initial temperature of the model.

In fact, equation (5.3) in practice because the camera takes only 1 frame in the experiments (see subsection 5.4.2) and the discrete time derivation can not be applied. To find the heat flux, the solution of the one-dimensional heat equation for a semi-infinite body with given initial temperature and constant heat transfer coefficient is used. If it is moreover assumed that the model is only slightly heated, i.e.

$$\theta = \frac{T(t) - T_{init,m}}{T_r - T_{init,m}} \ll 1 \tag{5.6}$$

then:

$$q(t) = \sqrt{\pi}/2 \frac{\sqrt{\rho_m C_m \lambda_m}}{\sqrt{t}} (T(t) - T_{init,m}) \tag{5.7}$$

where T_t is temperature of the surface of the model at time t, and C_m and ρ_m, C_m, λ_m are the density, heat capacity and thermal conductivity of the model respectively. For the material of the model $\sqrt{\rho_m C_m \lambda_m}$=0.891 KJ/m^2.K). In the more general case where (5.6) does not apply, one may use the exact solution:

$$\theta = 1 - \exp(\beta^2)\,\mathrm{erfc}(\beta); \qquad \beta = h \frac{\sqrt{t}}{\sqrt{\rho_m C_m \lambda_m}} \tag{5.8}$$

It is natural to assume that the thickness of the TSP is negligible, or that the thermal properties of the TSP and of the model material are similar, so that the TSP measures the temperature of the external surface of the model. The condition of constant heat transfer coefficient is well satisfied in shock tubes, Ludwig wind tunnels and blow-down wind tunnels with some device to input the model into the flow. In these wind tunnels, the time needed to establish the heat flux is much smaller than the operation time. In AT-303, the situation is more complicated. At low Mach numbers, in particular at $M_\infty = 5.73$, practically no steady state (plateau of pressure) can be reached (figure 5.22). At $M_\infty = 7.75$, things look better (figure 5.22). At $M_\infty = 5.73$, solution (5.8) do not apply, and one would have to solve the heat equation with time variable boundary conditions. However, the aim of this work is not to obtain accurately the Stanton number, but to compare the results for various parameters of the flow. So, the solution (5.7) is used anyway. The actual time evolution of the pressure is approximated with a top hat curve, as shown in figures 5.22 and 5.23. Stanton numbers calculated this way are then approximate.

5.6 Results of experiments

Ten runs have been performed. Parameters of the flow, angles of attack and slip angles are given in table 5.2. Results of relative Stanton number are shown in figures 5.24 and 5.25. Symmetry of the flow in experiments with β=0° is observed, that confirms proper installation and correct measurements.

5.6.1 Parasitic light

In runs 2663 and 2664, the correction for parasitic light was not able to completely remove zones of negative heat flux. Otherwise, it would have resulted in an unacceptable distortion of the heat flux. A high level of parasitic light on the side walls and near the symmetry plane of the model leads to an underestimation of the heat flux in these areas. It is recalled

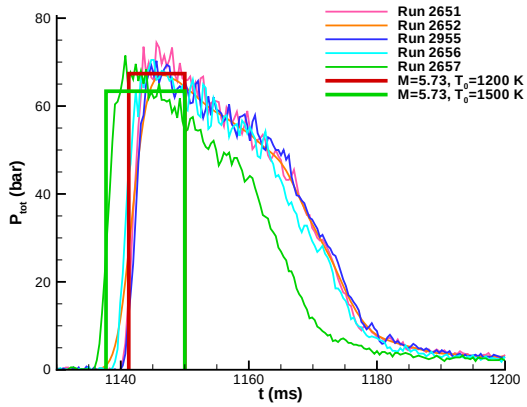

Figure 5.22: Measurement of total pressure at $M_{nom} = 6$ and value of pressure taken to compute Stanton number. Optical measurement is taken at t=1150 ms.

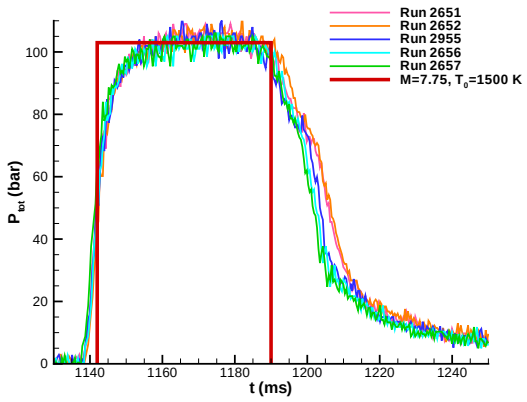

Figure 5.23: Same as figure 5.22. Optical measurement is taken at t=1190 ms.

Table 5.2: Flow parameters for the runs in AT-303.

Run	M_∞	P_{tot}(bar)	T_{tot}(K)	Re_u x 10^{-6}(1/m)	AoA° / β°	trips x(mm) / k(mm)
2651	5.73	67	1200	13.8	4 / 0	no
2654	5.73	67	1200	13.8	4 / 0	no
2655	5.73	67	1200	13.8	6 / 0	no
2656	5.73	67	1200	13.8	4 / 2	no
2657	5.73	63	1500	9.2	4 / 0	no
2661	7.75	103	1500	6.1	4 / 0	200 / 1
2662	7.75	103	1500	6.1	4/ 0	no
2663	7.75	103	1500	6.1	4 / 0	150 / 0.8
2664	7.75	103	1500	6.1	4 / 2	150 / 0.8
2665	7.75	103	1500	6.1	4 / 0	200 / 1.5

that there is no mean to exactly correct the parasitic light distribution, and therefore this correction is always subjective and can only slightly improve the final distribution of heat flux. Hence, the obtained heat fluxes are only relative. Nevertheless they may be used for a qualitative comparison with the level of calculated values. Figures 5.26 and 5.26) show that the levels of computed Stanton numbers with the turbulence model "on" and turned "off" are very similar to those observed in the turbulent and laminar areas in the experiments.

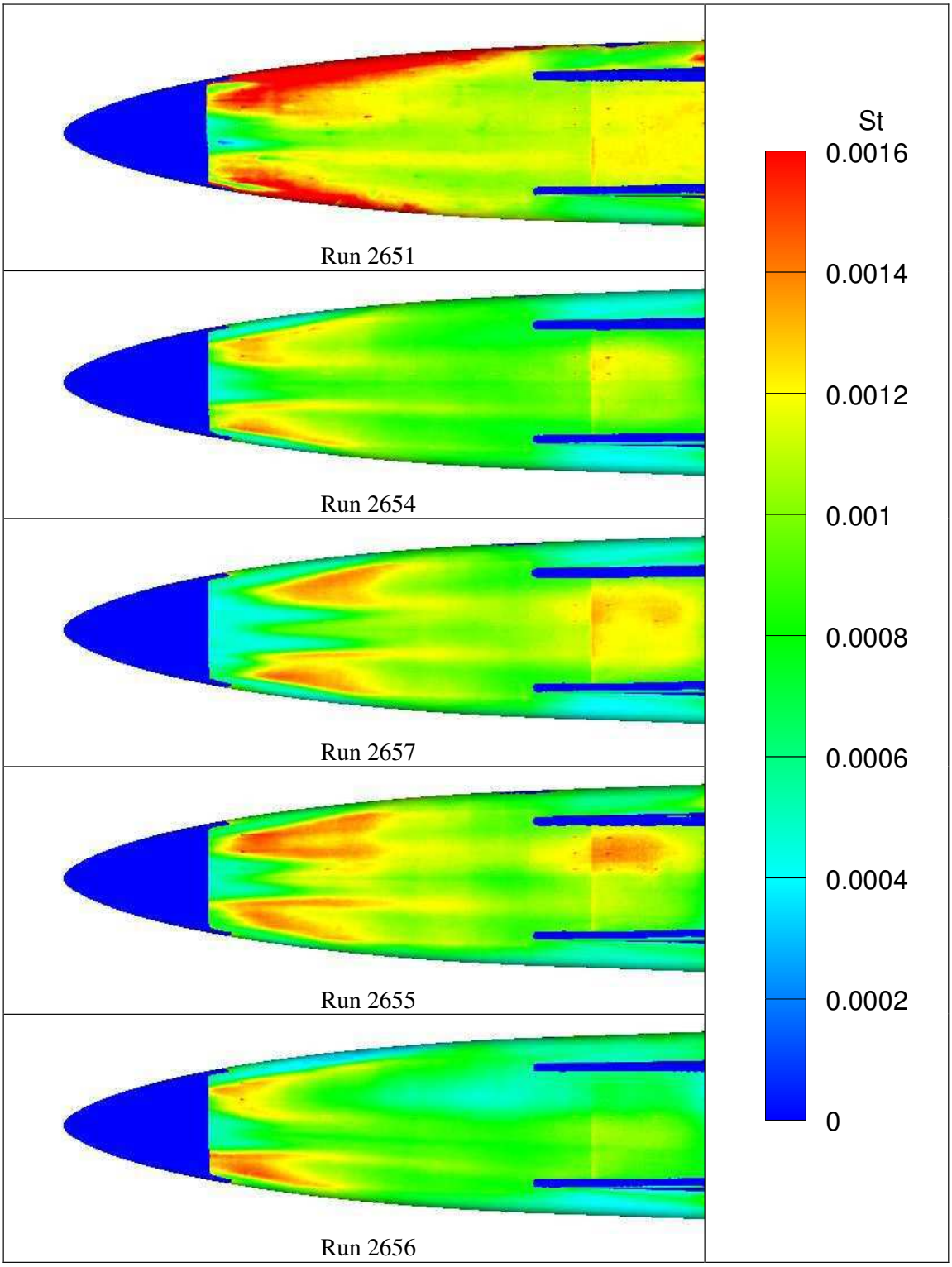

Figure 5.24: Fields of relative Stanton number at $M_\infty = 5.73$.

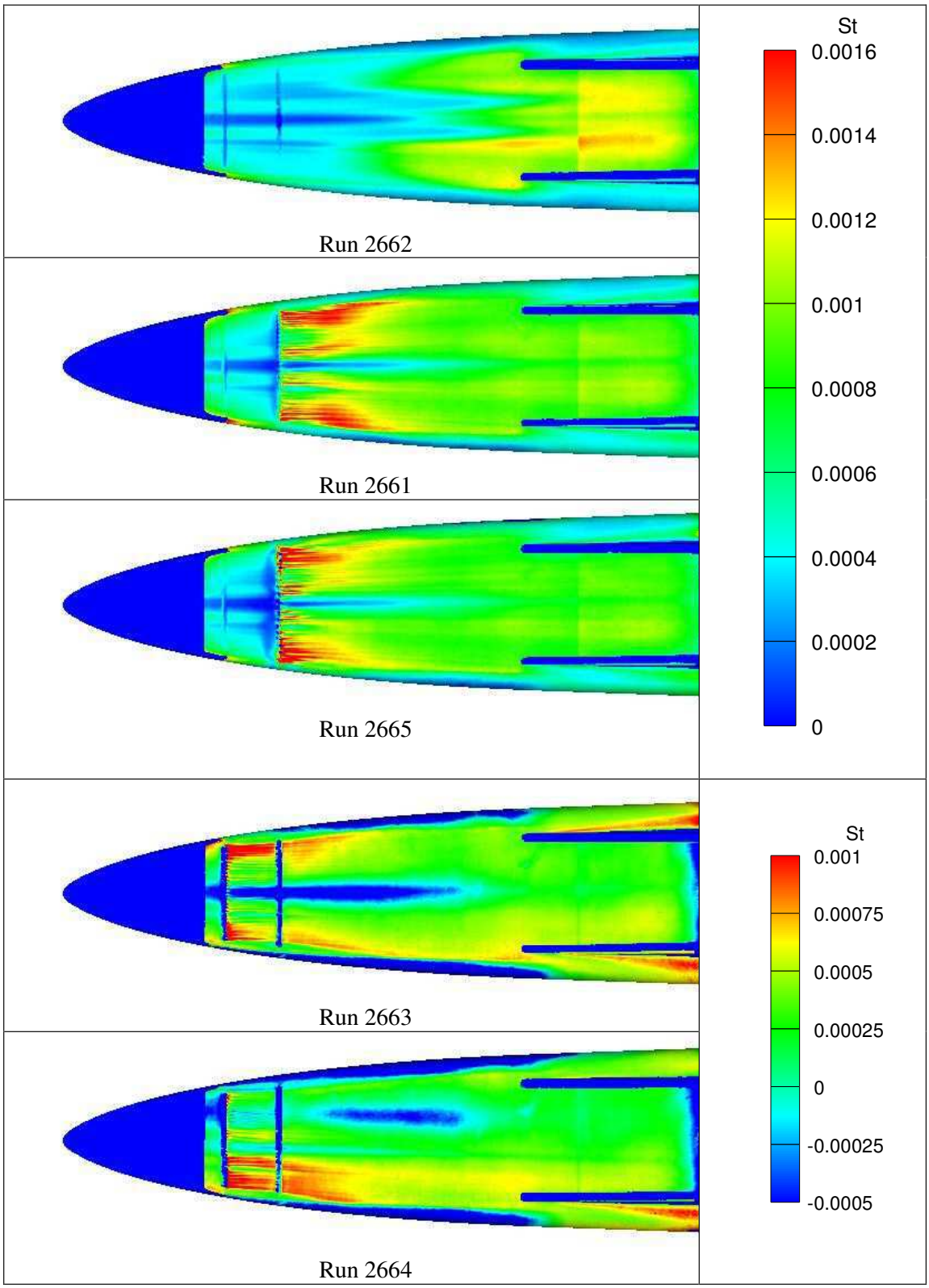

Figure 5.25: Fields of relative Stanton number at $M_\infty = 7.75$.

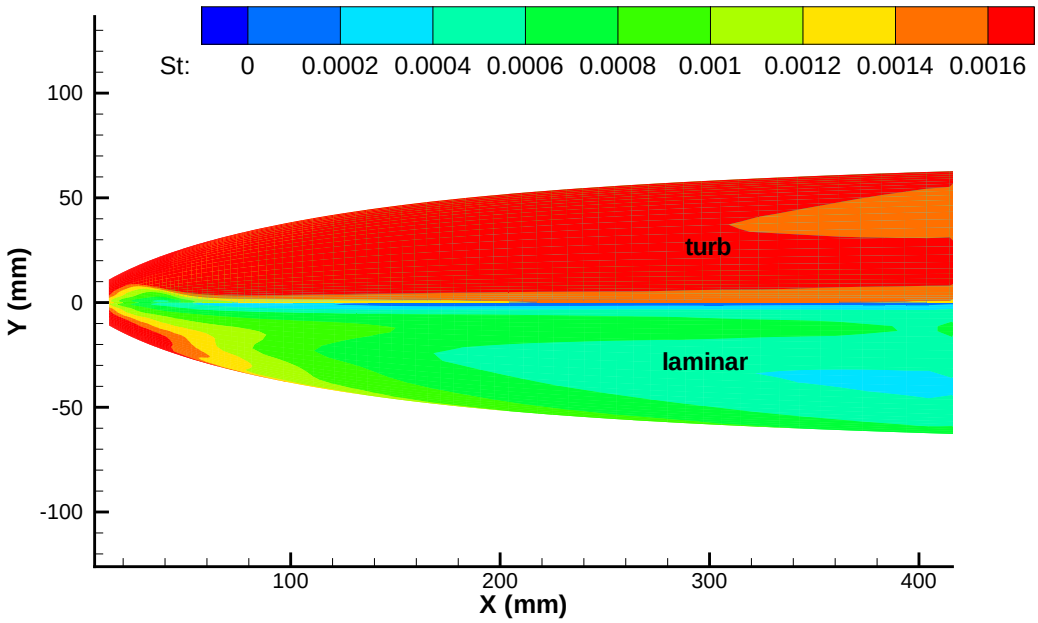

Figure 5.26: Computed Stanton number at $M_\infty = 5.73$.

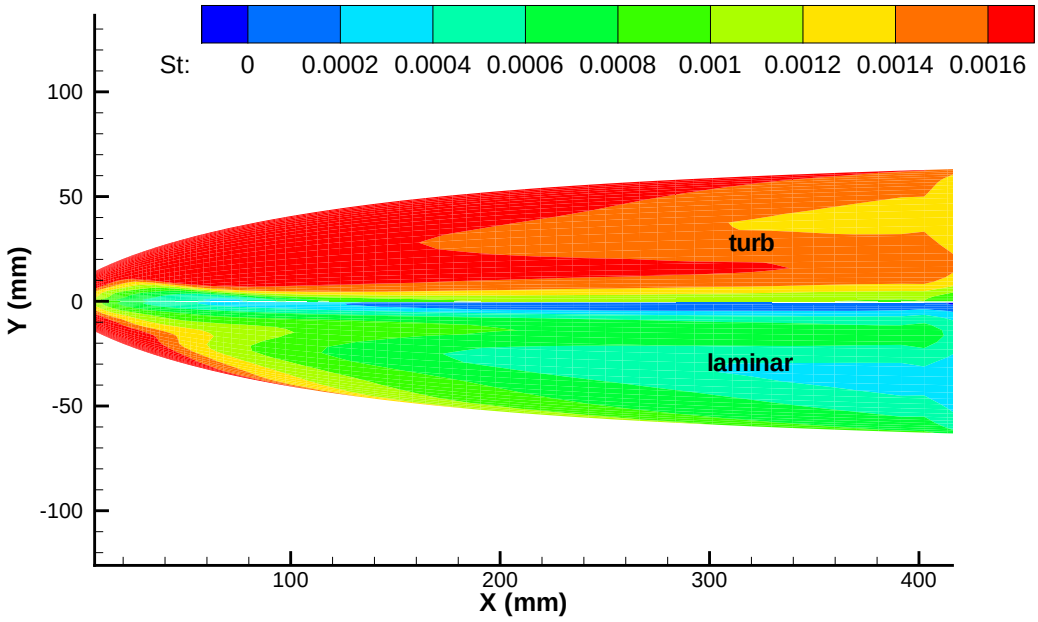

Figure 5.27: Computed Stanton number at $M_\infty = 7.75$.

5.6.2 Experimental determination of natural transition

$M_\infty = 5.73$

One case (AoA=4°, β=0°) is performed twice (2651 and 2654). The large heat fluxes observed on the lateral surfaces in run 2651 are the consequence of a default (step) at the junction of the insertion and the nose of the model. After the run, this step has been polished out. In all the runs at $M_\infty = 5.73$ the heat flux increases approximately by a factor $2 \sim 3$ after the nose part of the model. One can then conclude to a natural transition of the boundary layer. Near the plane of symmetry, where crossflow and longitudinal vortices have been identified by FLUENT® computations and oil-flow visualization in the blow-down T-313 experiments, transition is delayed.

The shape of laminar-turbulent transition is wavy. Two streaks of transition begin in the middle part between the symmetry plane and the leading edge and a third streak begins at the symmetry plane and the streaks join downstream . The streak in the symmetry plane may be related with EL instability or two very small contra-rotative vortices under the big vortices, which are observed in FLUENT® computation (figure 1.32). When the unit Reynolds number is reduced from 13.8 to 9.2 million (run 2657) the transition slightly moves downstream. It is illustrated in figures 5.28. The Stanton number is plotted along lines which are chosen to be the same as those for Pitot tubes measurements in T-313 (z = 8.5mm, z = 26mm and z = 43.5mm). An increasing heat flux corresponds to the beginning of transition and the maximum in distribution indicates the end of transition. In the compression ramp (+1°) the heat exchange intensifies. The end of transition in run 2654 at line z = 26mm and z = 43.5mm occurs at the same location $x \approx 170$mm and slightly moves downstream in run 2657 ($x \approx 200$mm). In run 2654 at $z = 8.5$mm laminar-turbulent transition takes place at $x \approx 217$mm and $x \approx 300$mm in run 2957. These results are gathered in table 5.3.

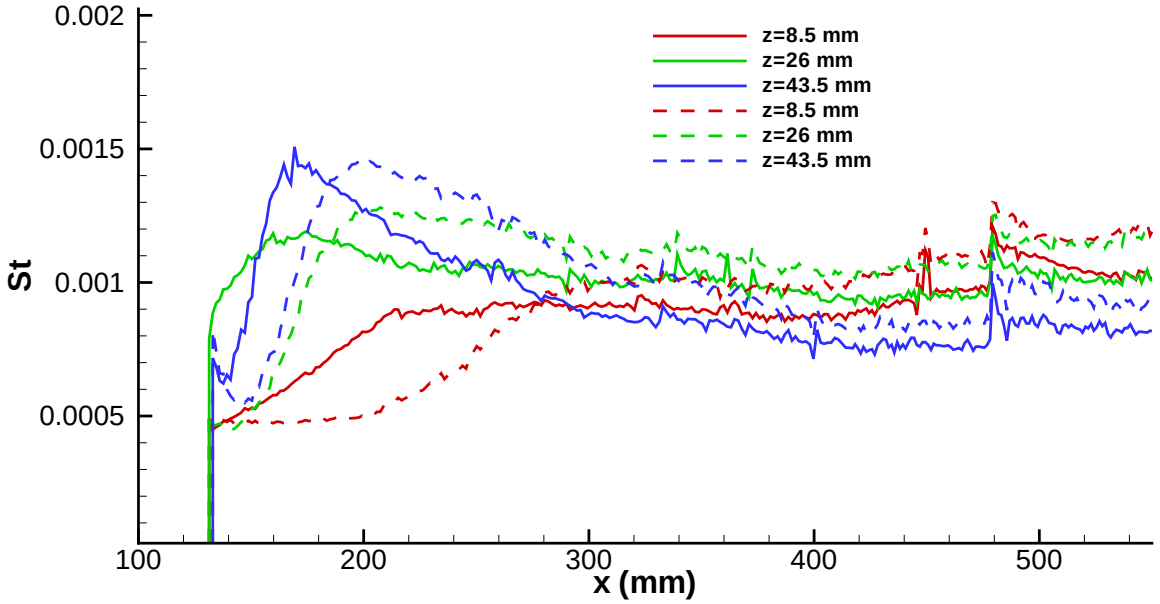

Figure 5.28: Distribution of Stanton number along x $M_\infty = 5.73$, runs 2654 (solid line) and 2657 (dashed line).

Table 5.3: End of transition at $M_\infty = 5.73$, runs 2654 and 2657.

Run	$z = 8.5$mm	$z = 26$mm	$z = 43.5$mm
	$x_{tr,end}$ (mm)	$x_{tr,end}$ (mm)	$x_{tr,end}$(mm)
2654	217	170	170
2657	300	200	200

Spanwise distributions of the Stanton number at several location are shown in figure 5.29. Computed values of the Stanton number for laminar (green dashed line) and turbulent (red dash-dot line) boundary layer are plotted together with experimental data. The boundary layer at cross-section $x = 135$ mm in run 2657 is obviously laminar. Moreover the value

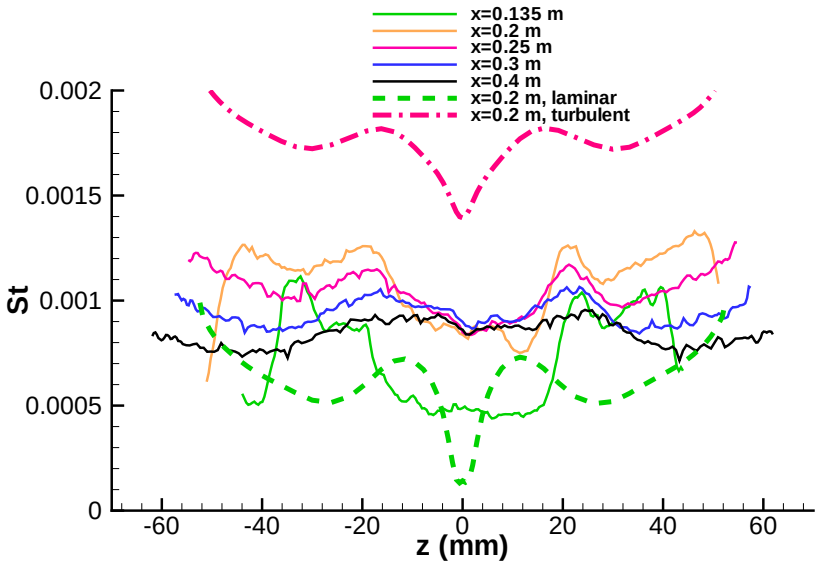

(a) P_{tot}=67 bar, T_{tot}=1200K, run 2654

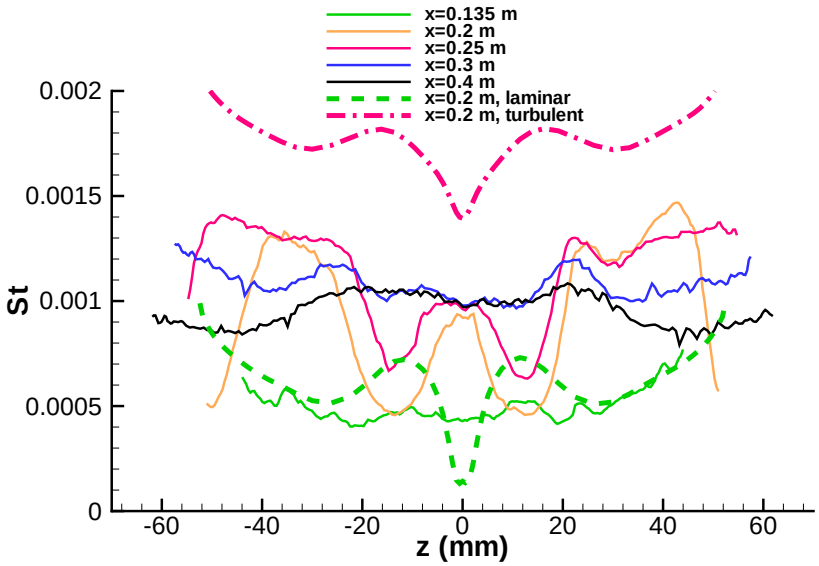

(b) P_{tot}=63 bar, T_{tot}=1500K, run 2657

Figure 5.29: Spanwise distribution of Stanton number at M_∞=5.73, runs 2654 and 2657.

and behavior of the relative Stanton number coincide well with laminar calculation. In run 2954 at the same cross-section $x = 135$mm boundary layer is turbulent in the middle part and laminar close to the leading edge and to the symmetry plane. This leads to strong non-uniformity (2 times) of heat flux in the spanwise direction. The boundary layer is turbulent at cross-section $x = 200$mm in run 2654 except small area close to the leading edge. When the boundary layer becomes turbulent the level of non-uniformity decreases down to 30%. In run 2657 at cross-section $x = 200$mm the wide laminar area are still present. At cross-section $x = 300$mm in run 2957 a boundary layer is everywhere turbulent. Levels of the relative Stanton number in experiments are lower than computed ones. This is due on one hand to parasitic light and to assumption (5.7) and on the other hand to computations that do not account to the position of the laminar-turbulent transition. At the same time, a qualitatively good agreement in behavior of the Stanton number is observed. There are local maximums and minimums on experimental and computed curves and their position coincide quite well.

Increasing the AoA from 4° to 6° does not effect much the transition (see run 2655 in figure 5.24). The results from stability analysis that increasing the AoA moves a little downstream the transition can not be proved.

M_∞=7.75

At Mach number M = 7.75 (run 2662, Re = 6.1×10^6 /m), the natural transition is also observed. Figure 5.30 shows the distributions of Stanton number along lines at $z = 8.5$mm, $z = 26$mm and $z = 43.5$mm. The line in the symmetry plane is also plotted to show presence of streaks. Computed value of the Stanton number for the laminar (dashed line) and the turbulent (dash-dot line) boundary layer are plotted together with experimental data. The beginning of transition at $z = 26$mm, $z = 43.5$mm and $z = 0$ mm is observed at $x \approx 240$mm. At $z = 8.5$mm, the beginning of transition is delayed and observed at $x \approx 360$mm. End of transition observes at $x \approx 350$mm for $z = 26$mm and 43.5mm. Close to the symmetry plane transition moves downstream. End of transition occurs at $x \approx 450$mm in the symmetry plane transition and $x \approx 470$mm at $z = 8.5$mm respectively. On the compression ramp (+1°) value heat flux jumps about 10% and it is seen at all lines.

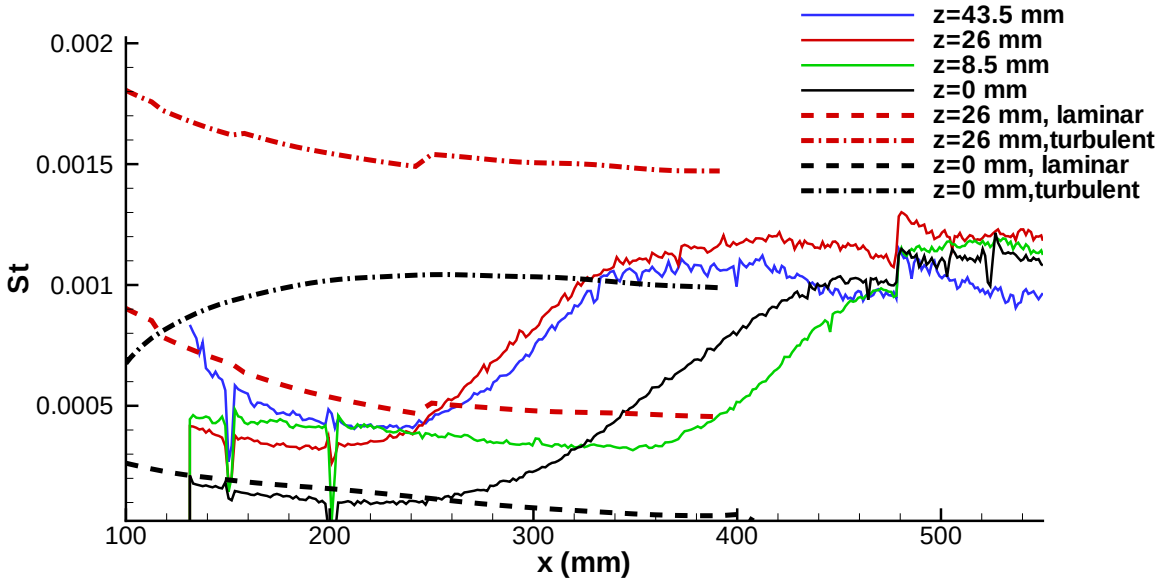

Figure 5.30: longitudinal distribution of Stanton number at M_∞=7.75, run 2662.

Table 5.4: End of transition at $M_\infty = 7.75$, runs 2662.

	$z = 0$mm	$z = 8.5$mm	$z = 26$mm	$z = 43.5$mm
$x_{tr,begin}$(mm)	350	240	240	240
$x_{tr,end}$(mm)	470	450	360	360

Figure 5.31 shows the spanwise distribution of the Stanton number, which is highly non-uniform. The general tendency observed at $M_\infty = 5.73$ is reproduced again. The position of local maxima and minima on experimental and computed curves coincide quite well. A qualitatively good agreement between computed and experimentally measured values of Stanton number is found and the prediction is almost perfect in the symmetry plane (black curves in longitudinal distribution).

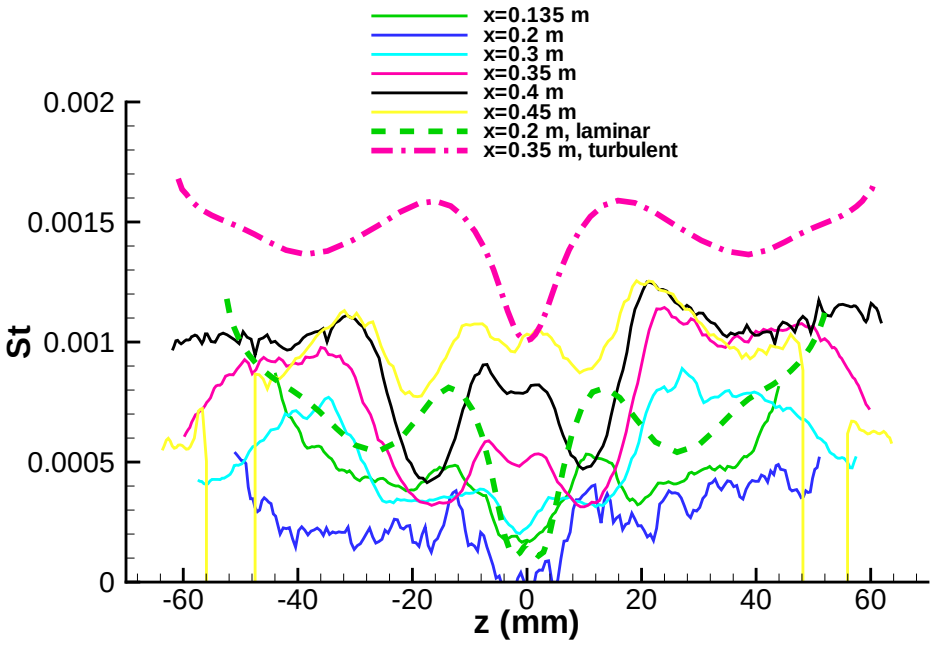

Figure 5.31: Spanwise distribution of Stanton number at M_∞=7.75, run 2662.

5.6.3 Natural transition: comparison calculations/experiments

In fact, calculations have been done before the experiments. The parameters of calculations are gathered in table 5.5. Stability analysis for case #1 has been done by Marc Ferrier and is shown in his thesis [12]. The main results obtained from this study is that a cold wall stabilizes the flow. It is well known that cooling the wall stabilizes the 1^{st} mode and destabilizes the 2^{nd} mode. In our case M_e is not high enough for the presence of a 2^{nd} mode. Case #2 has been done after the nozzle calibration with experimental M and the high temperature to see its effect on stability. Case #2 reproduces the temperature and Mach number of run 2657, but P_{tot}=47.5bar is lower than P_{tot}=63bar in the experiment. For case #2 the flow is unstable only close to the nose where CF mode is detected. Integration of amplification factors shows that values of N factors are even less than 1. Parameters of the flow in case #1 are very close to the experimental conditions (see table 5.2) and then can be comparable. At M=8 at experimental conditions the stability analysis shows that the flow

is stable and hence calculations are difficult to converge.

Table 5.5: Parameters of calculations to apply LST to simulate experimental runs in AT-303.

case #	M_∞	P_{tot} (bar)	T_{tot} (K)	P_{st} (Pa)	T_{st} (K)	Re_u (1/m)
1	6	64	1094	3776	139	13.8 $\times 10^6$
2	5.7	47.5	1554	3496	226	6.2 $\times 10^6$

Figure 5.32 shows the map of N factors fore case #1 and heat fluxes related to the position of laminar-turbulent transition in run 2654. Globally a stability prediction shows the same trend as in experiments: the laminar-turbulent transition occurs in the middle part, where N factor reach their maximum and transition is delayed close to the symmetry plane and the flow is stable in this location. The same is observed in blow down T-313 experiments (see sections 4.5). Figure 5.32 shows that $N_{tr,end}$ ~2. That is less compared to blow down T-313 experiments where $N_{tr,end}$ ~4. Two reasons may be involved: higher noise and flow pulsations in AT-303 (see section 5.1) compared to T-313. Probably the junction between the metallic nose and the plastic part may generate disturbances and as a result induce transition.

Recommendations regarding future tests:

- Check the effect of junction with fully plastic part.
- Obtain N factors of wind tunnel, as previously done for T-313 in the flat plate experiments: additional studies are needed on simpler configurations.

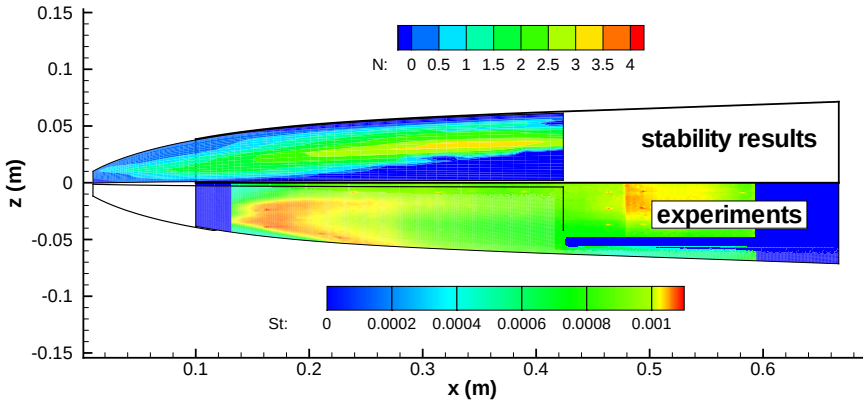

Figure 5.32: Computed N factor for case #1, $f = 15$ kHz. The Stanton number in run 2654.

5.6.4 Roughness-induced transition

Overview

It was mentioned in section 3 that there is no theory and no evidence how trips generally act on transition. It can be referred to Schneider's report [53] where three modes have been

suggested by which roughness may affect transition. In present study we considered only laminar-turbulent transition and not mechanisms which are more related to fundamental aspects.

- instabilities may grow in the wake of the trips,
- instabilities may grow via crossflow, Görtler, or transient-growth mechanisms associated with streamwise vorticity,
- freestream disturbances may interact with surface roughness and generate first-mode or second-mode waves.

Regarding measurements it is more complicated to distinguish in experimental results where induced transition occurs, compared to natural transition experiments. Trips may generate counter-rotating longitudinal vortices and if these vortices touch or get close they can push each other downward, squeeze boundary layer and increase the velocity gradient and consequently the surface heating [73]. Experiments without trips and CFD for laminar and turbulent boundary layer are needed for a comparison between measured and predicted values and may help detect the position of induced transition. Locations where roughness wakes merge due to turbulence may also indicate transition. Figures 5.33 and 5.34 show typical pictures obtained by IR and streamwise distribution of Stanton number for single trips of different shapes [73].

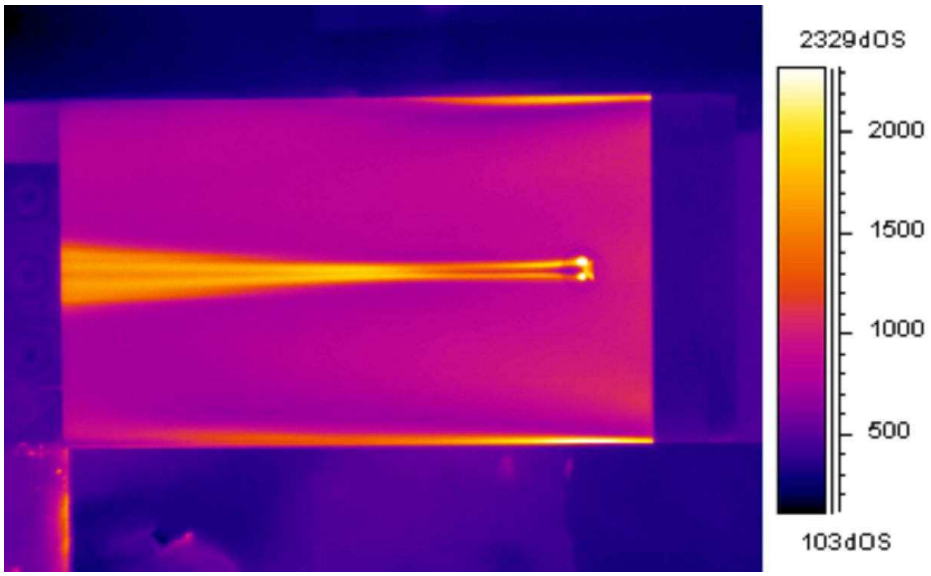

Figure 5.33: IR picture of roughness-induced transition in the Expert program.

Present study

A scheme of trips installation is shown in figure 5.13, and a photograph in figure 5.35.

Trips with height of 1 mm (run 2661) and particularly 1.5 mm (run 2665) create shock waves which seem to merge spanwise in a single shock (see figure 5.36). This causes the separation of the boundary layer ahead of the trips, as indicated by the low heat flux observed just before the trips (see figure 5.25). The influence of trips is different in different parts of the body. Close to the symmetry plane trips do not influence the laminar-turbulent

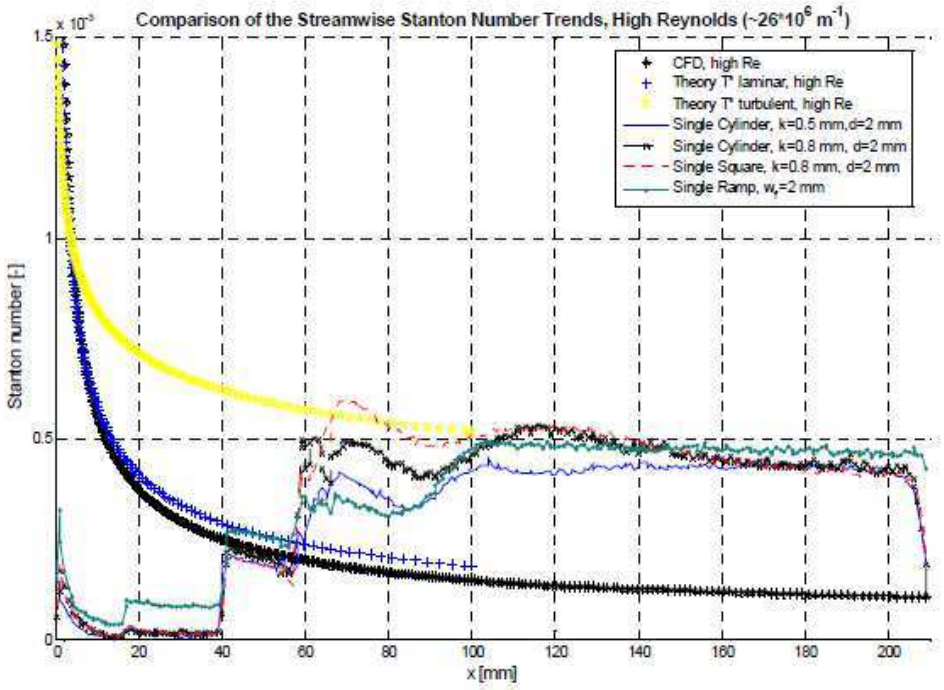

Figure 5.34: Streamwise distribution of St for different single trips.

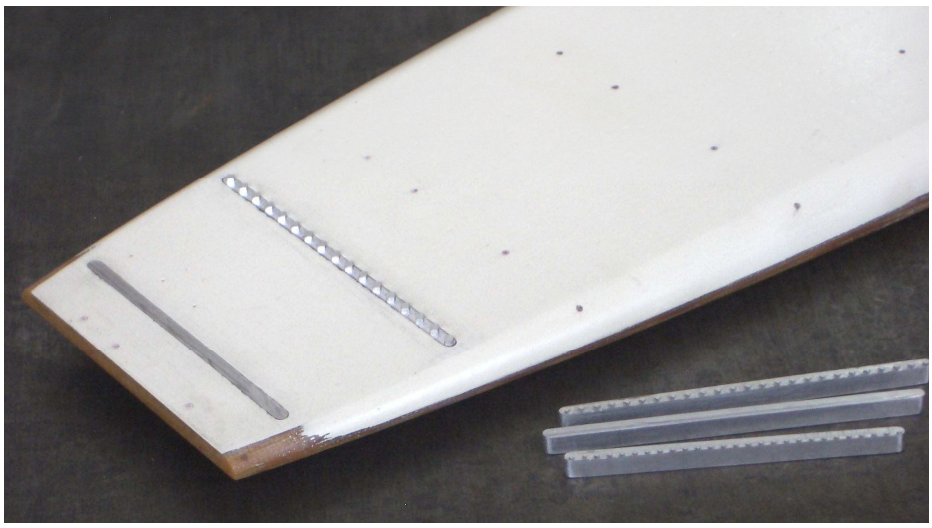

Figure 5.35: Photograph of trips installation.

transition. At lateral parts of the body, the laminar-turbulent transition occurs just after the trips. Clearly visible traces of individual trips merge at a distance of about 100 mm from trips. Figure 5.37 shows a comparison of the computed ratio k/δ at location $x \approx 200$mm where trips with size 1.5mm are installed in run 2665, with the spanwise distribution of heat flux just after the trips. Some correlation between them is found and may explain why laminar-turbulent transition is not provoked close to the symmetry plane. On the other hand, the vortices can be stable and are not affected by trips. Future experimental tests can give answer to this problem.

Figure 5.38 shows streamwise distributions of Stanton number for trips at $x \approx 200$mm

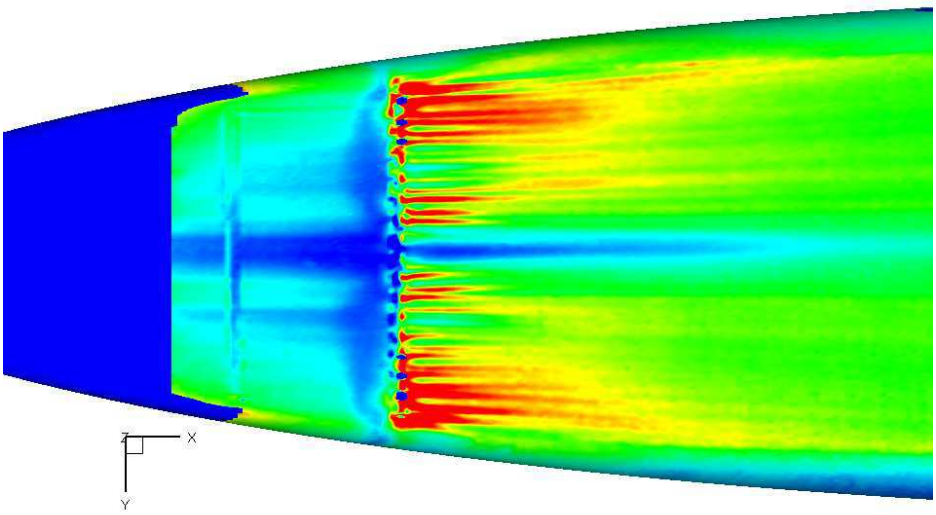

Figure 5.36: Photograph of trips installation.

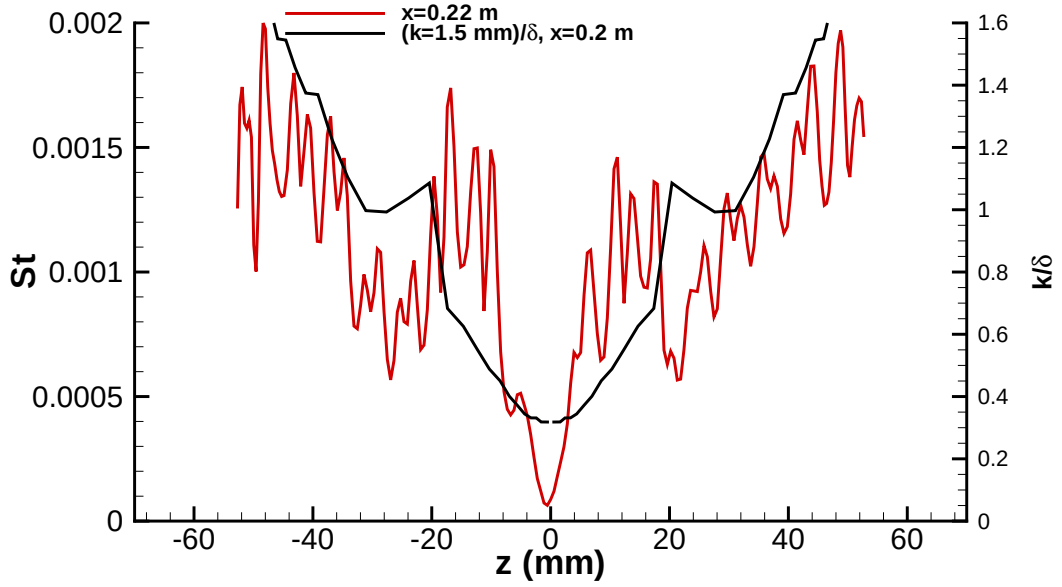

Figure 5.37: Comparison of Stanton number just after trips and ratio k/δ, where k=1.5 mm.

and comparison with run 2662 without trips. Just after trips the level of heat flux increases dramatically and reach the turbulent level 100 mm downstream from trips. Figures 5.39 and 5.40 illustrate the distribution of Stanton number in different cross-sections for trips installed at $x \approx 200$mm and figure 5.41 is the same for trips installed at $x \approx 150$ mm. For clarity, two cross-sections from run 2662 without trips with laminar boundary layer at $x = 220$mm and turbulent boundary layer at $x = 450$ mm are plotted. Spanwise distributions of the Stanton number before trips in run 2661 and 2665 match the curve at $x = 220$ mm in run 2662. Just after the trips, the value of the Stanton number greatly increases (red curves with big peaks). Comparison of cross-sections at $x = 450$ mm shows that with or without trips turbulent level of the Stanton number is more or less the same. In run 2663, the level of Stanton number is low, and at some locations, negatives values are observed (influence of

parasitic lights). Nevertheless, results allow to conclude that trips installed at $x \approx 150\,\text{mm}$ are also effective.

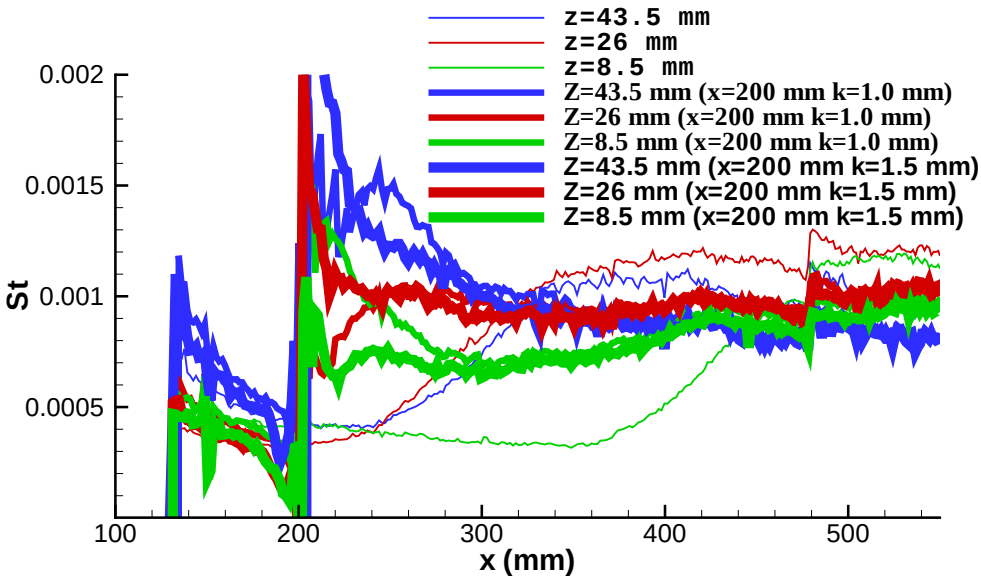

Figure 5.38: Effect of trips, streamwise distribution, $x = 200$ mm, k=1 mm and 1.5 mm.

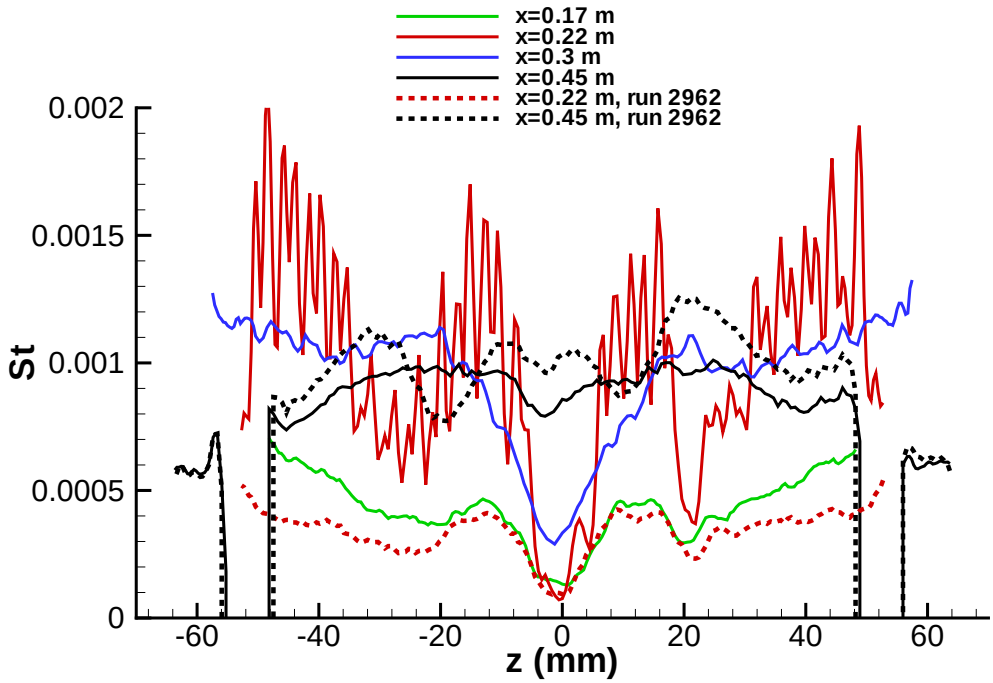

Figure 5.39: Effect of trips, spanwise distribution, $x = 200$ mm, k=1 mm, run 2661.

Regarding results of measurements, conclusion can be done that neither increasing the size of trips from 1 mm to 1.5 mm at $x \approx 200\,\text{mm}$ nor changing their location from 150 mm to 200 mm does move upstream (or just slightly) the laminar-turbulent transition close to

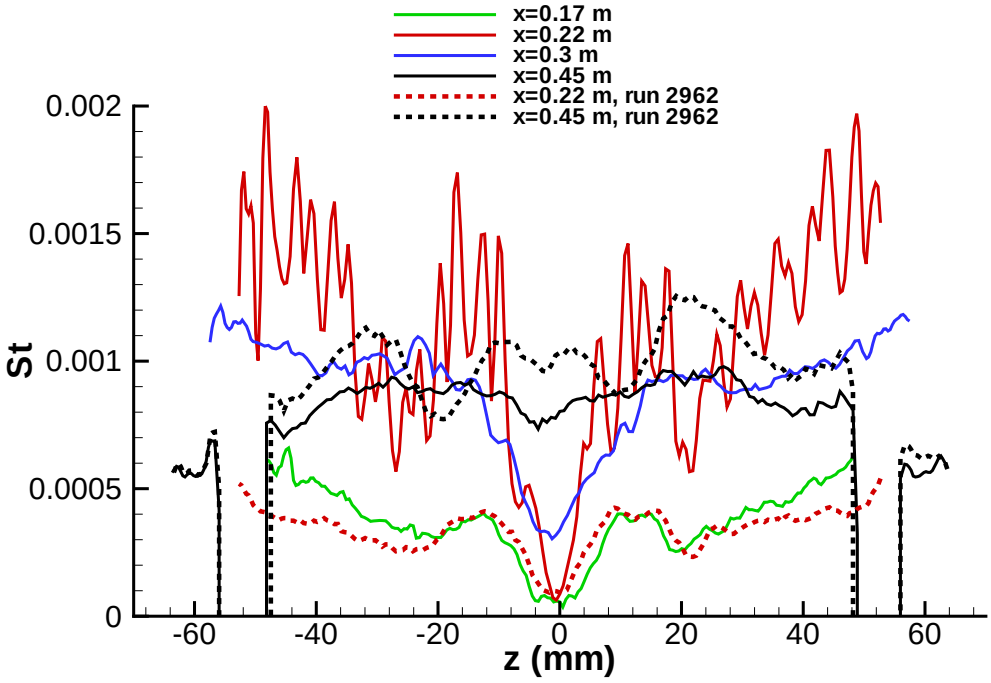

Figure 5.40: Same as figure 5.39, $x = 200$ mm, k=1.5 mm, run 2665.

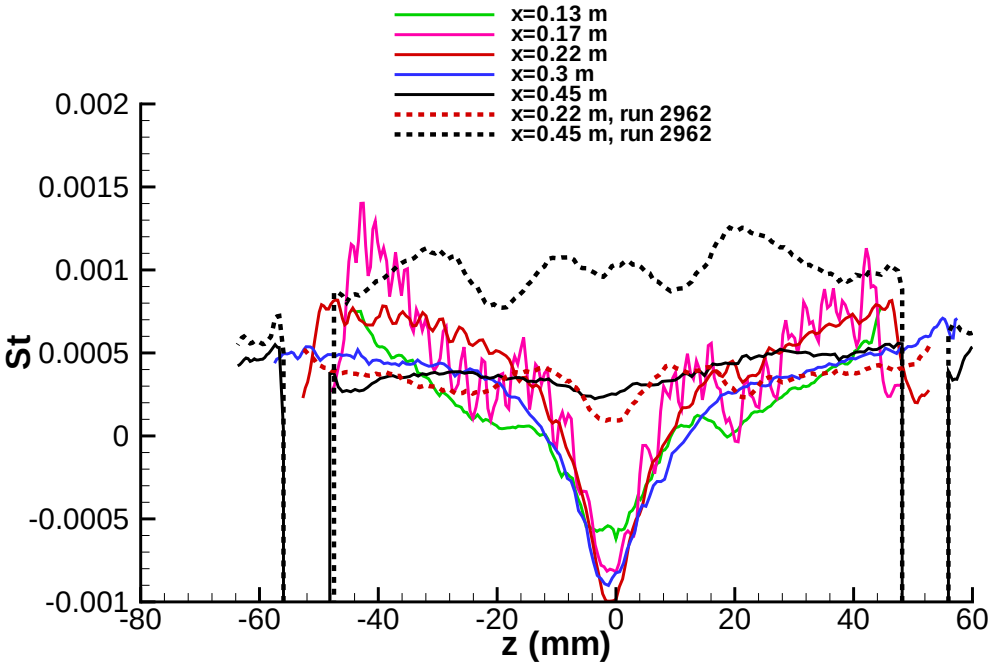

Figure 5.41: Same as figure 5.39, $x = 150$ mm, k=0.8 mm, run 2663.

the symmetry plane, but greatly reduce the width of the laminar zone close to the symmetry plane. Comparison between spanwise distributions at $x = 300$ mm in tests with (run 2661, 2663 and 2665) and without trips (run 2662) shows that the central wide laminar/transitional zone is reduced from about 60 mm to 40 mm by the trips. An important conclusion follows: all of the three inserts of diamond trips are effective, and empirical transition criteria which

have been used to choose the size of trips are valid in the conditions of AT-303 on this geometry. In further study it would be interesting to find minimal effective size and to apply empirical transition criteria to check their reliability.

5.6.5 Slip angle 2°

Two runs 2663 and 2664 at slip angle 2° have been done without trips at $M_\infty = 5.73$ and with trips at $M_\infty = 7.75$. Interesting results from experiments with or without trips are that in the middle part of the body, heat fluxes are lower in the windward side than in the leeward side. First idea was that is caused probably by parasitic light (see subsection 5.4.4). Figure 5.42 shows the laminar computation at slip angle 2° at $M_\infty = 5.73$. Computation shows the same tendency as in the experiments.

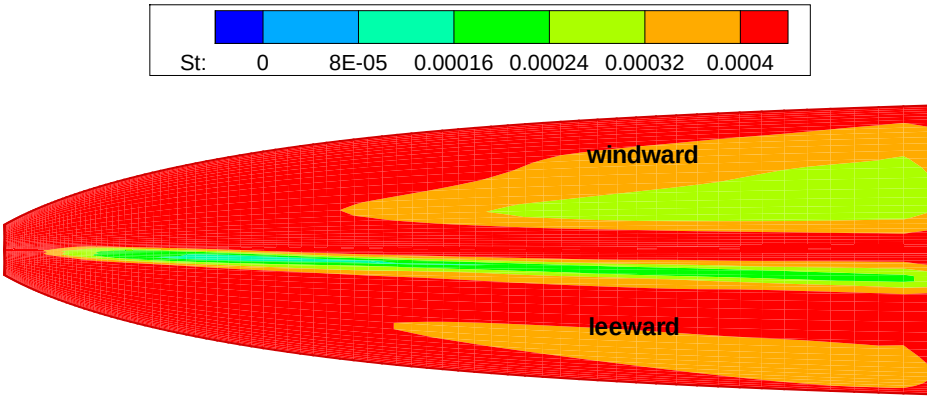

Figure 5.42: Map of computed wall heat flux at slip angle 2° at $M_\infty = 5.73$, laminar flow.

5.7 Conclusion

I: Experiments

According to the results of the experimental investigation in the impulse AT-303 wind tunnel, the position of the laminar-turbulent transition zone has been determined for Mach numbers 5.73 and 7.75.

- At $M_\infty = 5.73$, the natural laminar-turbulent boundary layer transition occurs immediately after the metallic nose of the model at Re_u=13.8×10^6 1/m.
- Decreasing the Reynolds number moves slightly the transition downstream.
- At $M_\infty = 7.75$ natural transition is also observed at $x \approx 400$ mm.
- All trips that have been tested proved their effectiveness.
- Both angle of attack and slip angle have little effect on the transition of the boundary layer.
- Near the plane of symmetry, transition is delayed.
- At slip angle heat fluxes are lower in the windward side than in the leeward side.

II: TSP

Two-color TSP paints have proved their good characteristics and reliability to detect the laminar-turbulent transition in an impulse wind tunnel like AT-303 in ITAM Novosibirsk.

III: CFD

Some conclusions can be drawn after the comparison between experiments and computations:

- Computed and measured Mach numbers by Pitot rake during nozzles calibration in AT-303 show an almost perfect agreement at $M_{nom} = 6$. At $M_{nom} = 8$, computed Mach numbers are about 1.5% lower.
- Recovered relative Stanton numbers in the experiments are comparable with FLUENT® computations. A qualitatively good agreement in the behavior of the computed and experimentally recovered Stanton numbers is observed.

IV: LST

Globally, stability predictions show the same trend as in experiments. N factors of transition in AT-303 are ~ 2, lower than in the blow down wind tunnel T-313, where $N \sim 4$. Two factors can be involved: disturbances in environments or junction between metallic nose and plastic part.

Conclusions and perspectives

The present work is related to the study of the laminar-turbulent transition on a generic hypersonic forebody. The LST coupled with the e^N method has been used to predict the transition in flight and in ground test conditions. The position of the laminar-turbulent transition zone has been determined during a limited number of experimental investigations: 4 tests at Mach numbers 4 and 6 in the T-313 blow down wind tunnel and 10 tests at Mach numbers 6 and 8 in the AT-303 impulse wind tunnel. The aim of these experiments was to understand (or at least to observe) how transition depends on the different environmental conditions typical of a blow down or an impulse wind tunnel (level of noise, tunnel or free jet test section...), to check the influence of flow conditions (total and wall conditions, angle of attack, slip angle, etc), and to check the stability predictions. From the results gained, some conclusions and perspectives can be drawn regarding both the experimental part related to ground tests and the computational part including CFD and the LST/e^N method for the prediction of transition in flight and in ground tests.

Concerning experimental methods, it has been proved that a simple technique like Pitot tube measurements is sufficient for the detection of the laminar-turbulent transition on the 3D forebody in the blow down wind tunnel. We did n't found any article about the use of Pitot tube measurements in the literature on 3D body, and from this point of view, the present study is original. The use of two-color TSP paints is a very efficient technique for heat flux measurements and is the best solution for the detection of the laminar-turbulent transition on a 3D body in a wind tunnel with short operation time. Using a camera with an electronic shutter (in the present study, the camera has a mechanical shutter) would reduce the level of parasitic light and increase the accuracy of measurements. The intensive development of infrared technologies with increasing spatial resolution may give in the future comparable results, but using TSP paints remains cheaper than the use of an infrared camera (price of camera, special glasses for IR). Some additional tests on a model with a full plastic upper part are needed to check the effect of the junction between the metallic nose and the plastic body part. Another interesting perspective would be to detect transition by measuring pressure pulsations in both wind tunnels. The question of how many gauges are needed to identify laminar and turbulent boundary layer regions is of interest, especially for flight tests where optical techniques can not be applied.

Concerning roughness-induced transition, the conclusions and perspectives are the following: all tested roughness have shown their effectiveness and hence could be used to induce transition in flight. However, they are quite high and modify dramatically the flow locally (shock and boundary layer separation). In a future work, it would be interesting to study active devices that would be able to control the transition along all the flight trajectory. The direct numerical simulations of active control by wall injection would be of great interest, and much easier than the simulation of transition by solid trips.

The present study has also dealt with CFD computations. CFD was used to prepare the experimental studies from which intelligible results have been obtained. Results of computations have also shown that the commercial code FLUENT® can be applied to compute the flow field around a full scale 3D forebody. Some local non-uniformities in the flow due to the marginal resolution of the shock have been observed in the nose region. However, their influence on the LST results in the ZI has been found to be negligible. Hence FLUENT® can be used to obtain the mean flow profiles for the LST : this is original. The crossflow found in the simulations has been confirmed by oil-flow visualization in the experiments. The measured and computed Pitot pressure profiles show quite a good agreement. The magnitude of Stanton numbers obtained in the experiments are comparable with the results from FLUENT® computations. A qualitatively good agreement in their distribution is observed. In order to recover the experimental Stanton number, the one-dimensional heat equation and the assumption that the model is only slightly heated have been used. The positive comparison with CFD results shows that this approach is effective.

The standard LST coupled with the e^N method has been applied to the 3D flow around the forebody for flight and wind tunnel conditions. N factors for transition have been obtained from flat-plate calibration in T-313 ($N \sim 4$) but remain unknown for the AT-303 wind tunnel. It would be interesting to carry reference experiments on simple geometries like cones or flat-plates in this wind tunnel. In the blow down wind tunnel T-313, at M_∞=4, the crossflow instability is weak, and the predicted transition using flat-plate correlations agrees very well with experiments. At M_∞=6, the crossflow instability is dominant at the nose of the body and a good agreement is found using the so-called "discriminant integration". The angle retained to segregate the crossflow instability is empirical and needs to be confirmed with further comparison between calculated and experimental transition results. In AT-303, stability predictions on the forebody show the same trend as in experiments. N factors at transition are about 2, lower than in T-313. Two factors may be involved: a noisy environment and the junction between the metallic nose and the plastic part of the model. Previous studies have been done showing that the level of noise in AT-303 corresponds to about 3% of the Pitot pressure with a frequency band wide enough (up to 40 kHz) to destabilize the 1^{st} mode. Some informations about spectra in the boundary layer in AT-303 conditions could be found using ALTP fast-response gauges [75] which allow to measure heat flux with a frequency band up to 1 MHz.

Some uncertainty remains about the longitudinal vortices close to the plane of symmetry. Their effect on the air inlet characteristics should be investigated and if their influence is negative, a mean to control these vortices should be found. In the present study, roughness-induced transition has shown that trips can not remove these vortices but only reduce their width.

The results from this thesis have been presented at four international conferences [76, 77, 78, 79]. An article has been published in *Journal of Spacecraft and Rockets* [13], and another has been submitted and is under review.

Conclusions et perspectives

Ce travail a concerné l'étude de la transition laminaire-turbulent sur un avant-corps hypersonique générique. L'analyse de stabilité linéaire couplée à la méthode du e^N a été mise en œuvre pour prévoir la transition en vol et dans les conditions d'essais au sol. La position de la zone de transition laminaire-turbulent a été déterminée lors d'un nombre limité d'expériences : 4 essais à nombres de Mach 4 et 6 dans la soufflerie continue T-313 et 10 essais à nombres de Mach 6 et 8 dans la soufflerie à rafale AT-303. Le but de ces expériences était de comprendre (ou au moins d'observer) comment la transition dépend des conditions environnementales typiques d'une soufflerie continue ou à rafale (niveau de bruit, veine fermée ou jet libre...), de vérifier l'influence des conditions d'écoulement (conditions génératrices, conditions de paroi, angles d'incidence et de dérapage etc), et de vérifier les prédictions de l'analyse de stabilité. A partir des résultats obtenus, on peut tirer quelques conclusions et perspectives concernant à la fois la partie expérimentale liée aux essais au sol et la partie calculs comprenant les simulations numériques et l'analyse de stabilité/méthode du e^N pour la prédiction de la transition en vol et au sol.

En ce qui concerne les méthodes expérimentales, on a pu montrer qu'une technique simple de mesure par tubes de Pitot est suffisante pour détecter la transition sur l'avant-corps 3D dans la soufflerie continue. Nous n'avons pas trouvé d'article dans la littérature faisant référence à l'emploi de tubes de Pitot, et en ce sens, la présente étude est originale. L'emploi de peintures thermosensibles (TSP) bicolores est une technique très efficace pour la mesure des flux de chaleur et est la meilleure façon de détecter la transition laminaire-turbulent sur un corps 3D dans une soufflerie à rafale. L'emploi d'une caméra à obturateur électronique (lors de cette étude, la caméra avait un obturateur mécanique) permettrait de réduire le niveau de lumière parasite et d'augmenter la précision des mesures. Le développement intensif des techniques de mesure infrarouge et l'aumentation de leur résolution spatiale permettra probablement d'obtenir à l'avenir des résultats comparables, mais l'emploi des TSP reste moins cher que celui d'une camera infrarouge. D'autres essais sur une maquette avec partie supérieure entièrement en plastique sont nécessaires pour tester l'effet de la jonction entre le nez métallique et corps en plastique. Une autre perspective intéressante serait de détecter la transition par la mesure des fluctuations de pression dans les deux souffleries. La question de savoir combien de capteurs sont nécessaires pour repérer les régions où la couche limite est laminaire ou turbulente est importante, principalement pour les essais en vol lors desquels les techniques optiques sont impossibles.

Concernant la transition par rugosités, les conclusions et perspectives sont les suivantes : toutes les rugosités testées se sont avérées efficaces et peuvent donc être utilisées pour déclencher la transition en vol. Cependant, elles sont assez hautes et modifient de façon importante l'écoulement localement (choc et décollement de la couche limite). Lors de travaux futurs, il serait intéressant d'étudier des dispositifs actifs qui permettraient de contrôler la transition sur tout le domaine de vol. La simulation numérique directe du contrôle actif par injection pariétale serait d'un grand intérêt, et plus facile à réaliser que la simulation directe

de la transition par rugosité.

Ce travail a eu aussi recours à la simulation numérique (CFD). La CFD a été utilisée pour préparer les expériences dont on a pu tirer des résultats parlants. Les résultats des calculs ont aussi montré qu'on peut utiliser le code commercial FLUENT® pour simuler l'écoulement autour d'un avant-corps 3D à l'échelle 1. On a pu malgré tout observer quelques oscillations numériques dans l'écoulement dues à une médiocre résolution du choc dans la région du nez. Néanmoins, une étude de convergence en maillage a montré que les profils de base ainsi obtenus avec FLUENT® étaient convenables pour les calculs de stabilité en aval, dans la ZI : ceci est original. L'écoulement de déversement transversal (crossflow) identifié dans les simulations a été confirmé par les visualisations expérimentales par film d'huile. Les profils de pression Pitot mesurés et calculés sont en bon accord. Les niveaux de nombres de Stanton obtenus lors des expériences sont comparables à ceux calculés par FLUENT®. Leur répartition est qualitativement en bon accord. La reconstruction des nombres de Stanton expérimentaux repose sur l'équation de la chaleur 1D et sur l'hypothèse que la paroi est faiblement chauffée. La comparaison favorable aux résultats de la CFD montre que cette démarche est valide.

L'analyse de stabilité modale couplée à la méthode du e^N a été appliquée à l'écoulement 3D autour de l'avant corps dans les conditions de vol et des essais au sol. Les facteurs N de transition ont été obtenus à partir de résultats de calibration sur plaque-plane dans T-313 ($N \sim 4$) mais restent inconnus dans la soufflerie AT-303. Il serait intéressant de réaliser des expériences de référence sur des géométries simples comme des cones ou des plaques planes dans cette soufflerie. Dans la soufflerie continue T-313, à M_∞=4, l'instabilité crossflow est faible et la transition prédite à partir des corrélations sur plaque-plane est en bon accord avec l'expérience. A M_∞=6, l'instabilité crossflow domine près du nez de l'avant-corps et un bon accord est obtenu moyennant l'emploi de la méthode dite "d'intégration discriminante". L'angle retenu pour isoler l'instabilité crossflow est empirique et doit être confirmé par d'autres comparaisons calculs-expérience. Dans AT-303, les prévisions de stabilité sur l'avant-corps montrent la même tendance que lors des expériences. Les facteurs N à la transition sont de l'ordre de 2, plus faibles que dans T-313. Deux facteurs peuvent être invoqués : un environnement plus bruyant et la jonction entre le nez métallique et le corps en plastique de la maquette. Des études précédentes ont montré que le niveau de bruit dans AT-303 correspond à environ 3% de la pression Pitot avec une gamme de fréquences suffisamment grande (jusqu'à 40 kHz) pour exciter l'instabilité crossflow ou le 1^{er} mode. Des informations spectrales dans la couche limite pourraient être obtenues à l'aide de capteurs ALTP à réponse rapide [75] qui permettent des mesures de flux chaleur sur une plage de fréquences allant jusqu'à 1MHz.

Quelques incertitudes demeurent à propos des tourbillons longitudinaux de part et d'autre du plan du symétrie. Leur effet sur les caractéristiques de l'entrée d'air doit être étudié et s'il est défavorable, il faudra trouver un moyen de contrôler ces tourbillons. Lors de cette étude, on a vu que la transition induite par rugosités ne supprimait pas ces tourbillons, mais réduisait seulement leur envergure.

Les résultats de cette thèse on fait l'objet de 4 communications dans des conférences internationales [76, 77, 78, 79]. Un article a été publié dans *Journal of Spacecraft and Rockets* [13] et un autre a été soumis.

Bibliography

[1] Charles, E., Cockrell, Jr., "Aerosciences, Aero-Propulsion and Flight Mechanics Technology Development for NASA's Next Generation Launch Technology program," AIAA paper 2003-6948

[2] Drummond, Ph., Bouchez, M. and McClinton, Ch.R.,"Overview of NATO background on SCRAMJET technology," RTO-TR-AVT-007-V2, Chap.1, 2007

[3] Falempin, F., Bouchez, M., Serre, L., Bruno, C. and Hendrick, P., "Air-Breathing Propulsion for Future Space Launchers Proposal for a Minimum R & T Program on For Europe," AIAA paper 2005-3362

[4] Hirschel, E.H., "Historical Perspective on Programs, Vehicles and Technology Issues," Critical Technologies for Hypersonic Vehicles Development, RTO-AVT-VKI Lecture Series, May, 2004, von Karman Institue for Fluid Dynamics

[5] Schneider, S.P., "Hypersonic laminar-transition on circular cones and scramjet forebodies," *Progress in Aerospace Science* Vol. 40, 2004, pp. 1-50

[6] Defense Science Board, "Report of the Defense Science Board Task Force on National Aero-Space Plane Program," November, 1992, DTIC citation AD-A274530

[7] Berry, S.A., DiFulvio, M., and Kowalkowski, M.K., "Forced Boundary-Layer Transition on X-43 (Hyper-X) in NASA LaRC 20-inch Mach 6 Air Tunnel," NASA/TM-2000-210316, Aug. 2000

[8] Borg, M.P., Schneider, S.P., and Juliano, T.J., "Effect of Freestream Noise on Roughness-Induced Transition for the X-51A Forebody," AIAA paper 2008-592, Jan. 2008

[9] Lau, K.Y., "Hypersonic Boundary Layer Transition - Application to High Speed Vehicle Design," AIAA paper 2007-310, Jan. 2007

[10] Schneider, S.P., "Flight Data for Boundary Layer Transition at Hypersonic and Supersonic Speeds," *Journal of Spacecraft and Rockets*, Vol.36, No. 1, 1999, pp. 8-20

[11] Reshotko, E., "Is Re_θ/M^e a meaningful transition criterion?," AIAA paper 2007-943, Jan. 2007

[12] Ferrier, M, "Analyse de la stabilité et prévision de la transition laminaire / turbulent de l'écoulement proche paroi sur l'avant-corps d'un véhicule hypersonique" *Thesis*, May 2006

[13] Ferrier, M., Fedioun, I., Orlik, E., and Davidenko, D., "Modal Linear Stability of the Near-Wall Flow on a Hypersonic Forebody," *Journal of Spacecraft and Rockets* Vol. 46, No. 1, 2009, pp. 51-66

[14] Burcat, A., and Ruscic, B., "Ideal Gas Thermodynamic Data in Polynomial form for Combustion and Air Pollution Use," *Third Millennium Ideal Gas and Condensed Phase Thermochemical Database for Combustion* [on line database], http://garfield.chem.elte.hu/Burcat/burcat.html, Dec. 2006

[15] Lemmon, E.W., Jacobsen R.T., Penoncello, S.G., and Friend, D.G., "Thermodynamic Properties of Air and Mixtures of Nitrogen, Argon, and Oxygen From 60 to 2000K at Pressures to 2000 MPa," *Journal of Physical and Chemical Reference Data*, Vol. 29, No. 3, 2000, pp. 331-385

[16] Wilke, C.R., "A viscosity equation for gas mixtures," *Chemical Physics*, Vol. 18, 1950, pp. 517-519

[17] Kee, R.J. *et al.*, *CHEMKIN collection*, release 3.5, Reaction Design Inc., Sandia National Laboratories, San Diego, CA, 1999

[18] Ferrier, M., Fedioun, I., and Davidenko, D., "Boundary-Layer Transition Prediction on a Hypersonic Vehicle Forebody," AIAA paper 2006-8092, Nov. 2006

[19] Malik, M.R., and Anderson, E.C., "Real gas effects on hypersonic boundary-layer stability," *Physics of Fluids* A Vol. 3, No. 5, 1991, pp. 803-821

[20] Quirk, J.J., "A contribution to the great Riemann solver debate," *Intl J. Numer. Meth. Fluids* 18, 555-574, 1994

[21] Robinet, J.-Ch., Gressier, J., Casalis, G., Moschetta, J.-M., "Shock wave instability and the carbuncle phenomenon: same intrinsic origin?" *J. Fluid Mech.*, vol. 417, 2000, pp. 237-263

[22] Kimmel, R.L., Klein, M.A., Schwoerke, S.N., "Three-dimensional hypersonic laminar boundary-layer computations for transition experiment designs," *Journal of Spacecraft and Rockets* Vol. 34, No.4, July-August 1997

[23] Kimmel, R.L., Poggie, J., Schwoerke, S.N., "Laminar-turbulent transition in a Mach 8 elliptic cone flow," *AIAA Journal* Vol. 37, No. 9, Sept. 1999

[24] Liechty, D.S., Berry, S.A., Hollis, B.R., and Horvath, T.J., "Comparison of Methods for Determining Boundary Layer Edge Conditions for Transition Correlations," AIAA paper 2003-3590, June 2003

[25] Lees, L., and Lin, C.C., "Investigation of the stability of the laminar boundary layer in a compressible fluid," NACA technical note No. 1115, Sept. 1946

[26] Mack, L. M., "Linear Stability Theory and the Problem of Supersonic Boundary-Layer Transition," *AIAA Journal* Vol. 13, No.3, 1975, pp. 278-289

[27] Mack, L.M., "Boundary-layer linear stability theory," AGARD report Vol.709, VKI, Brussels, 1984, pp. 3-1 – 3-81

[28] Malik, M.R., "Prediction and Control of Transition in Supersonic and Hypersonic Boundary Layers," *AIAA Journal* Vol. 27, No.11, 1989, pp. 1487-1493

[29] Poll, D.I.A., "Laminar-Turbulent Transition," AGARD report 319 vol.1, 1996, pp. 3-1 – 3-20

[30] Saric, W.S., Reshotko, E., and Arnal, D., "Hypersonic Laminar-Turbulent Transition," AGARD report 319 vol.2, 1998, pp. 2-1 – 2-27

[31] Arnal, D., "Transition Prediction in Industrial Applications," *Transition, Turbulence and Combustion Modeling*, ERCOFTAC series, Hanifi A., Alfredsson P.H., Johansson A.V. and Henningson D.S. ed., Kluwer Academic Publishers, 1998

[32] Vandomme, L., Chanetz B., Benay R., and Perraud J., "Transitional shock wave boundary layer interactions in hypersonic flow at Mach 5," AIAA paper 2003-6966, Dec. 2003

[33] Morkovin, M.V. and Reshotko, E. and Herbert, T., "Transition in Open Flow Systems - a Reassessment," *Bull. Am. Phys. Soc.*,1994, 39, 1882

[34] Malik, M.R., and Balakumar, P., "Acoustic receptivity of Mach 4.5 boundary layer with leading edge bluntness," *Theoretical and Computational Fluid Dynamics* Vol. 21, No. 5, 2007, pp. 323-342

[35] Fedorov, A., Khokhlov, A.P., "Prehistory of Instability in a Hypersonic Boundary Layer," *Theoretical and Computational Fluid Dynamics* Vol. 14, 2001, pp. 359-375

[36] Fedorov, A., Tumin, A., "Initial-Value Problem for Hypersonic Boundary-Layer Flows," *AIAA Journal* Vol. 41, No.3, 2003, pp. 379-389

[37] Forgoston, E., Tumin, A., "Initial-value problem for three-dimensional disturbances in a compressible boundary layer," *Physics of fluids* Vol. 17, 084106, 2005

[38] Mee, D.J., "Boundary Layer Transition Measurements in Hypervelocity Flows in a Shock Tunnel," AIAA paper 2001-0208

[39] Hiroki Sugiura, Naoko Tokugawa Yoshine Ueda, "Compressible Boundary-Layer Transition on an Axisymmetric Body at Incidence," AIAA 2004-0251

[40] Ito T., Randall L.A., Schneider, S.P., "Effect of Freestream Noise on Roughness-induced Boundary-Layer Transition for a Scramjet inlet," AIAA 2000-0284

[41] Holden M.S., Wadhams T.P., MacLean, M, Walker, B.J., "Experimental Studies in Hypersonic Flows for Facility and Code Validation," AIAA 2007-1304

[42] "Pegasus® Wing-Glove Experiment to Document Hypersonic Crossflow Transition-Measurement System and Selected Flight Results," NASA/TM-2000-209016

[43] Dhawan, S., "Direct Measurements of Skin Friction," NACA Rept. 1121, 1953

[44] Ehud Gartenberg, Robert E. Wright, "Boundary-Layer Transition Detection with Infrared Imaging Emphasizing Cryogenic Applications," AIAA Journal Vol. 32, No. 9, Sept. 1994

[45] Borovoy, V.Y., "Gas flow and heat transfer in the areas of interaction of shock waves with boundary," Mashinostroenie, 1983, (in Russian)

[46] V.Å. Mosharov, V.N. Radchenko, "Measuring the heat fluxes fields in impulse wind tunnel with TSP," TsAGI, Uchenye Zapiski, vol. 38, No 1-2, p.94 - 101, 2007, (in Russian)

[47] Merski, N.R., "Reduction and Analysis of Phosphor Thermography Data With the IHEAT Software Package," AIAA Paper 98-0712, 1998

[48] Buck, G.M., "Simultaneous Global Pressure and Temperature Measurement Technique for Hypersonic Wind Tunnels," AIAA Paper 2000 - 2649

[49] Kornilov, V., "Investigation Transition of Boundary Layer on Flat Plate at Super- and Hypersonic Velocities," to appear Journal Thermophysics and Aeromechanics, vol. 16, No 3, 2009

[50] Lebiga, V., "Boundary Layer Transition and Reversal Phenomenon at High Flow Velocities," 4th Pacific International Conference on Aerospace Science and Technology, Taiwan, May 21-23, 2001

[51] Menter, F.R., "Two-Equation Eddy-Viscosity Turbulence Models for Engineering Applications," *AIAA Journal* Vol. 32, No.8, 1994, pp. 1598-1605

[52] Schneider, S.P., "Summary of Hypersonic Boundary-Layer Transition Experiments on Blunt Bodies with Roughness," *Journal of Spacecraft and Rockets*, Vol. 45, No. 6, 2008, pp. 1090-1105. doi: 10.2514/1.37431

[53] Schneider, S.P., "Effects of Roughness on Hypersonic Boundary-Layer Transition," AIAA paper 2007-0305, Jan. 2007

[54] Potter, J.L., and Whitfield, J.D., "Effects of slight nose bluntness and roughness on boundary-layer transition in supersonic flow," *Journal of Fluid Mechanics*, Vol. 12, No. 4, 1962, pp. 501-535

[55] Tirtey, S.C., Bolnot, H., Bottini, H., Paris, S., Fletcher, D.G., and Chazot, O., "In-Flight Hypersonic Roughness Induced Transition Experiment ," AIAA paper 2008-0250, Jan. 2008

[56] Tirtey, S.C., and Chazot, O., "Experimental Investigations on hypersonic roughness induced transition for EXPERT program ," AIAA paper 2008-2597, May 2008

[57] Whitfield, J.D. and Iannuzzi, F.A.,"Experiments on Roughness Effects on Cone Boundary-Layer Transition Up to Mach 16," *AIAA Journal* Vol. 17, No.3, 1969, pp. 465-470

[58] Van Driest, E.R., and Blumer, C.B., "Boundary layer transition at supersonic speeds: roughness effects with heat transfer," *AIAA Journal*, Vol. 6, No. 4, 1968, pp. 603-607

[59] Reshotko, E., and Tumin, A., "Role of Transient Growth in Roughness-Induced Transition," *AIAA Journal* Vol. 42, No.4, 2004, pp. 766-771

[60] Reda, D.C., "Review and Synthesis of Roughness-Dominated Transition Correlations for Reentry Applications," *Journal of Spacecraft and Rockets*, Vol. 39, No. 2, March-April 2002, pp. 161-167. doi: 10.2514/2.3803

[61] Berry, S.A., Bouslog, S.A., Brauckmann, G.J., and Caram, J.M., "Shuttle Orbiter Experimental Boundary-Layer Transition Results with Isolated Inducer," *Journal of Spacecraft and Rockets*, Vol. 35, No. 3, 1998, pp. 241-248

[62] Berry, S.A., Auslender, A.H., Dilley, A.D., and Calleja, J.F., "Hypersonic Boundary-Layer Trip Development for Hyper-X," *Journal of Spacecraft and Rockets*, Vol. 38, No. 6, 2001, pp. 853-864. doi: 10.2514/2.3775

[63] Micol, J.R., "Langley Aerothermodynamic Facilities Complex: Enhancements and Testing Capabilities," AIAA Paper 98-0147, January, 1998

[64] Horvath, T.J., Berry, S.A., Hollis, B.R., Chang C.L., and Singer, B.A.,"Boundary Layer Transition on Slender Cones in Conventional and Low Disturbance Mach 6 Wind Tunnels," AIAA Paper 2002-2743, June 2002

[65] Horvath, T.J., Berry, S.A., and Hollis, B.R., "Boundary layer transition on slender cones in conventional and low disturbance Mach 6 wind tunnels," AIAA paper 2002-2743, June 2002

[66] Schneider, S. P., "Effect of High-Speed Tunnel Noise on Laminar-Turbulent Transition," *Journal of Spacecraft and Rockets*, Vol. 38, No. 3, 2001, pp. 323-333

[67] Schneider, S. P., "Development of Hypersonic Quiet Tunnels," *Journal of Spacecraft and Rockets*, Vol. 45, No. 4, 2008, pp. 641-664

[68] Borg, M.P., and Schneider, S.P., "Effect of Freestream Noise on Roughness-Induced Transition for the X-51A Forebody," *Journal of Spacecraft and Rockets*, Vol. 45, No. 6, 2008, pp. 1106 -1116. doi: 10.2514/1.38005

[69] Berry, S.A., Nowak, R.J., and Horvath, T.J., "Boundary Layer Control for Hypersonic Airbreathing Vehicles," AIAA paper 2004-2246, June 2004

[70] Whadams, T. P., Mundy, E., MacLean, M. G., and Holden, M. S., "Ground Test Studies of the HIFiRE-1 Transition Experiment Part 1: Experimental Results," *Journal of Spacecraft and Rockets*, Vol. 45, No. 6, 2008, pp. 1134-1148. doi 10.2514/1.38338

[71] Alba, C.R., Johnson, H.B., Bartkowicz, M.D., and Candler, G.V.,"Boundary-Layer Stability Calculations for the Hifire-1 Transition Experiment," *Journal of Spacecraft and Rockets*, Vol. 45, No. 6, 2008, pp. 1125-1133. doi 10.2514/1.37445

[72] Kulesh, V.P., Morozov, A.N., Mosharov, V.E., Radchenko, V.N., "The application of prism image splitter for pressure distribution measurement using the method of two-color luminescent sensor," Instruments and Experimental Techniques, v.1, 2001

[73] Bottini H., Jivraj, F., Strub, A., Paris, S., Asma, C.O., and Fletcher, D.G., "Inducer-Induced Transition in Hypersonic Boundary Layers," AIAA paper 2007-537, Jan. 2007

[74] Perraud, J., Arnal, D., Dussillols , L., Thivet F.,"Studies of Laminar-Turbulent Transition in Hypersonic Boundary Layers at ONERA," 3^{rd} European Symposium on Aerothermodynamics for Space Vehicles Noordwijk, The Netherlands 24-26, November 1998

[75] Tim Roediger, Helmut Knauss, Boris Smorodsky, Malte Estorf, Steven Schneider, "Hypersonic Instability Waves Measured Using Fast-Response Heat-Flux Gauges," *Journal of Spacecraft and Rockets*, Vol. 46, No. 2, 2009 pp. 266-273, doi 10.2514/1.37026

[76] Ferrier, M., Orlik, E., Fedioun, I., and Davidenko, D., "Three Dimensional Linear Stability Analysis of the Boundary and Entropy Layers on Hypersonic Vehicle Forebody," 2^{nd} European Conference for Aerospace Sciences, Brussels, Belgium, July, 2007

[77] Orlik, E., Kornilov, V., Ferrier, M., Fedioun, I., and Davidenko, D., "Hypersonic Laminar/Turbulent Transition: Computations and Experiments," 3^{rd} European Conference for Aerospace Sciences, France, Versailles, July, 2009

[78] Ferrier, M., Fedioun, I., Orlik, E., and Davidenko, D., "Transition Prediction of the 3D Boundary Layer Under an Hypersonic Vehicle Forebody," 15^{th} AIAA International Space Planes and Hypersonic Systems and Technologies Conference, Dayton, Ohio, Apr. 28-May 1, 2008

[79] Orlik, E., Fedioun, I., and Davidenko, D., "Boundary-Layer Transition on a Hypersonic Forebody: Experiments and Calculations," 16^{th} AIAA/DLR/DGLR International Space Planes and Hypersonic Systems and Technologies Conference, Germany, Bremen, October, 2009

Appendix

```
/************************************************************************
   UDF to calculate temperature field function and store in
   user-defined memory. Also print min, max, avg temperatures.
************************************************************************/
#include "udf.h"

DEFINE_ON_DEMAND(zone_domain_threads)
{
   int nThread, nCells;
   real xc[ND_ND];
   real density;
   real pressure;
   real velocity_U;
   real velocity_V;
   real velocity_W;
   real temperature;

   FILE *FileOut;

   Domain *d; /* declare domain pointer since it is not passed as an
                 argument to the DEFINE macro  */
   Thread *t;
   cell_t c;
   face_t f;
   d = Get_Domain(1);     /* Get the domain using Fluent utility */

   FileOut = fopen("MeshCells.dat", "w");

   /* Loop over all cell threads in the domain */
   nThread = 0;
   thread_loop_c(t,d)
     {

     nThread++;

     /* Loop over all cells  */
     nCells = 0;
     begin_c_loop(c,t)
       {
         nCells++;
 if( nThread == 2 )
 {
C_CENTROID(xc,c,t);
   density = C_R(c,t);
           pressure = C_P(c,t);
           velocity_U = C_U(c,t);
           velocity_V = C_V(c,t);
           velocity_W = C_W(c,t);
```

```
           temperature = C_T(c,t);
fprintf(FileOut, "%24.16e %24.16e %24.16e   %24.16e  %24.16e  %24.16e
%24.16e  %24.16e  %24.16e\n", xc[0], xc[1], xc[2],pressure,density,velocity_U,
velocity_V,velocity_W,temperature);
 }
       }
     end_c_loop(c,t)

     printf("\n nThread = %i   nCells = %i\n", nThread, nCells);
/*     printf("%g  %g  %g\n", xc[0], xc[1], xc[2]);
*/
     }


   /* Loop over all cell threads in the domain */
   nThread = 0;
   thread_loop_f(t,d)
     {

     nThread++;

     /* Loop over all cells  */
     nCells = 0;
     begin_f_loop(f,t)
       {
         nCells++;
 if( nThread == 13 )
 {
F_CENTROID(xc,f,t);
           density = 0.0;
           pressure = 0.0;
           velocity_U = 0.0;
           velocity_V = 0.0;
           velocity_W = 0.0;
           temperature = 0.0;
 fprintf(FileOut, "%24.16e %24.16e %24.16e   %24.16e  %24.16e  %24.16e
 %24.16e  %24.16e  %24.16e\n", xc[0], xc[1], xc[2],density,pressure,velocity_U,
 velocity_V,velocity_W,temperature);
 }
       }
     end_f_loop(f,t)
 printf("\n nThread = %i   nCells = %i\n", nThread, nCells);
     //printf("%g  %g  %g\n", xc[0], xc[1], xc[2]);

   }
fclose(FileOut);
}
```

Evgeniy ORLIK

ETUDE DU CHAMP AERODYNAMIQUE ET DE LA TRANSITION LAMINAIRE-TURBULENT SUR L'AVANT-CORPS D'UN VEHICULE HYPERSONIQUE

Résumé:

Prévoir la transition laminaire-turbulent de la couche limite sur l'avant-corps d'un véhicule hypersonique est important pour optimiser l'entrée d'air du superstatoréacteur qui lui est associé, mais reste très difficile après un demi-siècle de recherches intensives sur le sujet. Dans ce travail, les approches numériques et expérimentales sont mises en œuvre et comparées. Expérimentalement, la transition naturelle est détectée à Mach 4 et Mach 6 dans la soufflerie continue T-313 de l'ITAM à Novossibirsk à l'aide de mesures de pression Pitot. Dans une autre soufflerie de l'ITAM, la AT-303 à rafale, on a détecté la transition naturelle à Mach 6 et la transition déclenchée par rugosités à Mach 8 à l'aide d'un procédé optique basé sur l'emploi de peintures thermosensibles. Ces essais ont été réalisés sur maquette à échelle 1/3. Toutes les rugosités testées se sont montrées efficaces. La prévision théorique de la transition naturelle a été réalisée au moyen de la théorie de la stabilité linéaire locale modale couplée à la méthode du e^N. En vol, sur avant-corps à échelle 1, les facteurs *N* atteignent difficilement 8 à 9, ce qui est insuffisant pour assurer la transition avec certitude. Pour appliquer la méthode aux essais au sol, on a besoin de connaître les facteurs *N* de transition des souffleries, ce qui est réalisé à partir d'essais de calibration sur plaque plane dans T-313. Un excellent accord théorie/expérience est obtenu à Mach 4. A Mach 6, on doit prendre en compte la présence d'instabilité ''crossflow'' inflexionnelle au nez de l'engin, moyennant quoi l'accord est aussi très bon. Les calculs de stabilité ont été réalisés sur des solutions de base obtenues par simulation numérique (CFD) des conditions de vol ou des essais au sol. Ces simulations ont également permis de bien comprendre la structure de l'écoulement autour de l'avant-corps et de concevoir en grande partie les moyens d'essai.

Mots clés: transition laminaire-turbulent, écoulement hypersonique, couche limite, stabilité, soufflerie continue, soufflerie à rafale, transition déclenchée par rugosités

INVESTIGATION OF FLOW FIELD AND LAMINAR-TURBULENT TRANSITION ON A FOREBODY OF HYPERSONIC VEHICLE.

Abstract:

The prediction of the laminar-turbulent transition in the boundary layer on a hypersonic vehicle forebody is important to optimize the air inlet of the associated scramjet engine, but is still very difficult after half a century of intensive research on the subject. In this work, numerical and experimental approaches are applied and compared. Experimentally, the natural transition is detected at Mach 4 and Mach 6 in the blow down wind tunnel T-313 in ITAM Novosibirsk using Pitot pressure measurements. In the impulse AT-303 wind tunnel in ITAM, the natural transition at Mach 6 and the roughness induced transition at Mach 8 are detected using an optical method based on thermosensitive paints. These tests have been performed on a 1/3 scale model. All the trips tested have shown their effectiveness. The theoretical prediction of the natural transition has been performed using the local modal linear stability theory coupled with the e^N method. In flight, on the full scale forebody, *N* factors hardly reach 8 to 9, which is insufficient for the transition. To apply the method to ground tests, the wind tunnels transition *N* factors are needed. They are obtained from calibration tests on a flat plate in T-313. A very good agreement with experiments is found at Mach 4. At Mach 6, the presence of inflexional crossflow instability near the nose of the body must be taken into account, which gives also a good agreement. Stability calculations have been done for mean flow solutions obtained by numerical simulations (CFD) of flight or ground tests conditions. These simulations have also helped to understand the structure of the flow around the forebody and to design efficiently the experimental setup.

Keywords: laminar-turbulent transition, hypersonic flow, boundary layer, stability, blow down wind tunnel, impulse wind tunnel, roughness-induced transition

Laboratoire ICARE-CNRS

1C Av. de la Recherche Scientifique,
45071 Orléans cedex 2